POLITECNICO DI TORINO

Corso di Laurea Magistrale

in Ingegneria Civile

Tesi di Laurea Magistrale

Freezing process in porous media

Relatori

Prof.ssa Marina Pirulli

Prof. Claudio Scavia

Candidato

Giorgia Amato

Anno Accademico 2018/2019

Contents

List of Tables

List of Figures

Abstract

Frozen soil is a multi-phases system composed of mineral particles, ice, unfrozen water and gas. Due to the existence of ice, several factors affect frozen soil properties (*e.g.*, pressure, temperature, salinity, etc..). Mechanical and deformation behaviour of frozen soil is not completely clear. A better understanding of physical frozen soil properties and of its freezing process are needed to improve the prediction of frozen soil deformation characteristics. This has application in aged cold region engineering problems such as the Frost heave but also in new issues of the modern era related to the Artificial Ground technique and to Global warming, since the recorded increasing creep settlements. This thesis describes different freezing procedures to make a elementary representative frozen specimen. Its mechanical response corresponds to the mechanical behaviour of soil only if the frozen specimen is homogeneous and isotropic and does not contain ice segregation inside the soil matrix. If not, the mechanical response would be the sum of that from ice and from frozen soil. Two kind of frost susceptible soil were investigated: Halden silt and Onsoy clay. The Onsoy clay showed ice lensing phenomena, while Halden silt frozen without the development of ice lenses. The analysis were computed on 3D images taken by the x-ray tomography scanner. Further investigation were carrier out on the 1D freezing process. Its evolution was scanned over the time by x-ray tomography. Moreover, this last allowed to explore and analyze phenomena involved by freezing, such us frost heave and section shrinkage for the clay. The frost heave and the maximum frozen height were measured for the 1D frozen clay specimen at different thermal gradients. A reliable quantification of section shrinkage was obtained by digital image processing of 3D images, taken during a one freeze-thaw-freeze cycle.

Acknowledgments

Firstly I would like to thank Professor Gudmund R. Eiksund for teaching me all I needed to work with frozen soil and carefully following me in every step. Many thanks to Dr. Edward Andò for be present (physically and virtually) in every moments and for encouraging me to do more and more. You taught me a lot about tomography and image processing and you showed me how much passionate the research world is. A particular thank for Professor Cino Viggiani, who believed in me and supported me in the worst moments. Thanks for your classes and life lessons. Thank to Professor Alice Di Donna, for all the valuable advises she gave me during these months. I would like to thank Professor Marina Pirulli and Professor Claudio Scavia for being my supervisors at Politecnico of Turin. *Un grazie speciale va alla mia famiglia. Grazie mamma per non avermi mai fatto sentire sola ed essermi sempre stata vicina anche a kilometri di distanza. Grazie per aver esultato insieme a me dopo le mie vittorie e avermi sostenuto quando sono stata sconfitta. Conosci sempre la parola giusta da dire. Grazie papà per aver sempre creduto in me e per avermi aiutato a valutare tutte le decisioni prese durante la mia carriera universitaria e non. Tu mi hai insegnato ad osare e a non arrendersi mai di fronte agli ostacoli che la vita pone davanti. Grazie a mio fratello Dario per essermi stato vicino e avermi sempre fatta ridere. La tua voglia di fare è da sempre un esempio per me. Ringrazio Anna e Mariachiara, le mie amiche di sempre. Grazie Stefania per il sostegno e l'affetto. Vorrei poi ringraziare tutti i colleghi con cui ho avuto il piacere di collaborare durante il mio percorso di studi. Ciascuno di voi mi trasmesso un insegnamento. In particolare grazie a Serena e Roberta, fedeli alleate che l'università mi ha regalato. Grazie alla mia Crazy Family, che durante quast'ultimo anno mi è stata vicino. Ringrazio infine tutti gli zii, i cugini e gli amici che sono stati fonte continua di energia durante questo percorso.*

Chapter 1

Introduction

Since the Cold-war era, engineering properties of frozen soils have been investigated. The first research groups born to study permafrost and frozen materials, initially with military installation purposes and then to develop the north Russia [Cole and Abdullahi (2001)].

Nowadays, many other issues bring civil engineers to further study frozen soils physical, thermal and mechanical properties. On one hand, in frost susceptible soil frost heave causes the raise of the ground, damaging pavements and structures' foundations. On the other hand, over the last years global warming is generating new foundation challenges. Due to the increasing large-scale ground temperature, permafrost and seasonally frozen soil are getting more and more warm, evidencing creep settlements of the ground and slope instabilities.

Furthermore, over last few decades, properties of frozen soil have been further explored to improve new techniques, recently arisen in the scenario of the ground stabilization. First and foremost, the Artificial Ground Freezing (AGF) provides the improvement of the soil strength and get it impervious by extracting heat from soil.

Current researches aim to develop constitutive models able to describe the stress-strain behavior of frozen soil. This is an hard challenge, since several factors need to be taken into account (*e.g.*, pressure, temperature, salinity, unfrozen water, etc..). Furthermore, many kind of cryogenic structures exists in nature [Kanevskiy et al. (2013)].

When upon freezing, ice segregates inside the soil matrix, assuming different shapes and making frozen soil inhomogeneous. In this conditions, mechanical tests' responses would be the sum of the response of two different phases, the frozen soil and the ice.

To obtain the actual behavior of frozen material, avoid the segregation of ice lenses in frozen soil is needed. The main objective of this research is to study different freezing procedures in order to find the parameters affecting the ice crystal size and identify the freezing procedure which allows to get an elementary representative frozen samples. In this last, ice crystals are expected to be uniformly distributed, in the way they cannot be identify as a separated phases from frozen soil.

Further analysis were also carried out as an attempt to extend the understanding of the short-term deformations. Indeed, despite of frozen soil has been studied for a long time, short and long-term permanent changes in soil structures as a result of freezing are not well understood. Furthermore, the demand of short-term volumetric changes prediction is increasing by the AGF techniques. They require an accurate estimation of stresses involved on the surrounding soil by the ground freezing to avoid damages on the near buildings and infrastructures.

Two frost susceptible soil were analyzed during this master research: the Halden silt and the Onsoy clay. After a first examination of the clay sampling procedures, several specimens were made.

Different three-dimensional freezing procedures were tested and then the understanding of the freezing phenomenon was extended by the analysis of the one-dimensional freezing. Indeed, if one looks at the phenomena at a smaller scale, even the three-dimensional freezing process occurs due to a one dimensional thermal gradient.

Clay specimens were 1D frozen imposing three different thermal gradients. The deformation behaviour of clay was observed also upon one freeze-thaw-freeze cycle.

Finally, the experimental data were compared with the results from two frost front penetration models: the Stefan formula and the Modified Barggren equation, adopted by cold region civil engineering for the frost front penetration prediction.

The analysis carried out in this master project were possible by using the *digital image processing* of 3D images, scanned by the x-ray tomograph. This latter consists of a x-rays source, which shots x-ray to the soil mass, and a detector, which measures the x-ray attenuation field due to the material crossing. The peculiarity of x-ray tomography is that scans are taken from many different angular positions. The reconstruction of these scans returns a 3D image. These latter are composed of voxels (3D pixels). Each voxel returns a measurement of the x-ray attenuation in terms of grey value, which is closely related to the mass density [Viggiani et al. (2014)].

Chapter 2

Literature review

This chapter presents an overview about frozen soil, natural freezing processes and the deformation mechanisms observed in literature. It wants to introduce sufficient background knowledge for understanding the basic behavior of soil upon freezing.

2.1 Frozen soil

Natural frozen soil exits in large parts of northern Europe, north central Asia, Alaska, Canada, southern part of south America and large parts of the United States, which are Cold regions, since their isotherm is 0 °C in the coldest month of the year[Bates and Bilello (1966)]. Frozen soil is defined as the soil with a temperature below 0 °C [Andersland and Ladanyi (2004)]. If the soil keeps this last temperature during at least two consecutive winters and the intervening summer, frozen ground is called *Permafrost* or *Perennially frozen ground*, while it is defined *Seasonally frozen soil* or *Active layer* if its temperature fluctuates above and below 0 °C [Andersland and Ladanyi (2004)].

In nature, frozen soil exists in the form of cyostructure, defined as a pattern formed by inclusions and lenses of pore and segregated ice [Kanevskiy et al. (2013)]. Figure 2.1 shows the main cryostructure types of mineral soils found in nature. In the upper permafrost of the Beaufort Sea Coast of Alaska, Kanevskiy et al. (2013) found that the most common cryostructure of silt and clay was the Ataxitic in which soil aggregates are suspended in an ice matrix.

Frozen soil mainly differs from the unfrozen soil since it contains ice in addition to the mineral

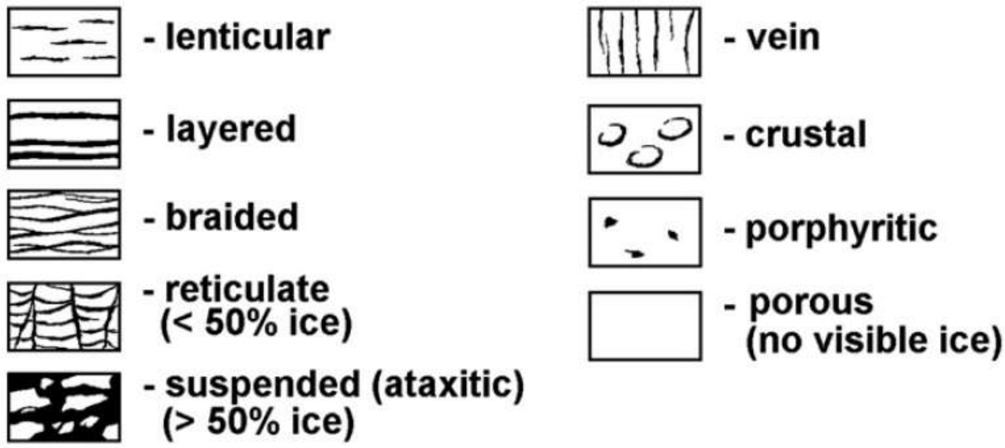

Figure 2.1: Main types of cryostructures of mineral soils (ice is black) from Kanevskiy et al. (2013)

particles, water and air or gas. Its constituents coexist and interact with each other and may switch their phases, depending on the environmental changes [Jia (2018)]. The size and shape of soil particles affects the molecular interaction forces of the mineral particles with each other and with water. Inter molecular forces are able to suppress freezing although temperature drops below 0 °C.

Water exists in three states depending on its distance from the mineral particles. *Firmly bond* water is called the first layer surrounding the mineral particle on which interactive forces are higher. Such water does not freeze even if temperatures drops to −186 °C. The attractive forces decreases on the next layer, which is called *loosly water*. Finally, *Free water* exists farther from mineral particles and when temperature drops below the freezing point it is frozen first. Such forces becomes bigger for large specific surfaces of the mineral particles. It is the case for clay and silt. By cooling down sand and clay below the freezing point, the unfrozen water content was measured from 0.2 to 2% and from 5 to 40%, respectively. Therefore, especially for the clay, taking into account the existence of unfrozen water is needed, since it is massively present when it is frozen [Tsytovich (1960)].

Ice is the main constituent which gets frozen soil of particular interest. Depending on the micro structure of soil, pressures and salinity, ice does not form necessary at 0 °C [Fofonoff and Millard Jr (1983)]. For cohesionless soils with small specific surface area, the *initial freezing* *temperature* T_f can be close to 0 °C, while for cohesive soils soils T_f can be −5 °C. Comparing to the unfrozen soil, the existence of ice soil significantly increases the strength of frozen soil [Andersland and Ladanyi (2004)] and decreases its permeability and deformability. On the other hand, it makes the frozen soil's behavior not easy to understand and predict, since it get influenced by many factors, *e.g.*, loading rate, temperature, pressure, salinity, etc.. [Jia (2018)].

2.2 Freezing process in natural frozen soil

The natural freezing process is a one-dimensional phenomenon leaded by a vertical thermal gradient. In cold regions, due to the air temperature, ground surface reaches below 0 °C temperature. This last increases moving down toward the Earth's core, due to the geothermal heat. Furthermore, geothermal heat makes the air temperature can't affect the soil temperature below 10 or 20 m [Andersland and Ladanyi (2004)]. Temperature profiles in Seasonally and Perennially frozen soil are shown in Figure 2.2.

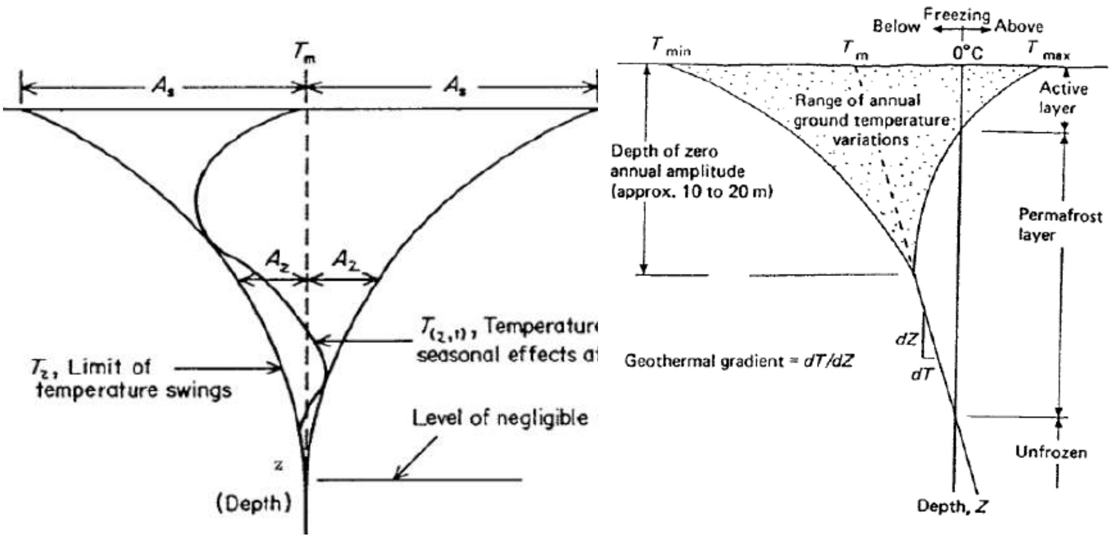

Figure 2.2: Temperature profiles in Seasonally (left) and Perennially (right) frozen soil from Andersland and Ladanyi (2004)

To model the cryogenic processes in permafrost and seasonally frozen soils, Thomas et al. (2009) considered two seasonal freezing scenarios. The *One-sided freezing*, for soils without permafrost, where frost front penetrates from the surface downward and the *two-sided freezing*, for soils underlain by permafrost, where large thermal gradient above the permafrost layer can make active layer freezing in two directions, from the permafrost table upwards and from the ground surface downwards.

In his *Discrete ice lens theory*, Nixon (1991) modeled the one-side monodimensional freezing process on a homogeneous fine-grained soil column (Figure 2.3). He identified a zone of frozen soil, an active ice lens, a freezing fringe zone and an underlying zone of unfrozen soil. The active ice lens grows by freezing unfrozen water existent at its boundary, which has gone through frozen fringe. Since the freezing fringe are region of impeded flow caused by partial filling of soil pores by ice, ice lens stops growing when the water supply of the current frozen fringe is cut off [Nixon (1991)].

In the frozen fringe region, soil skeleton is assumed incomprehensible and it only expands when the pressure in the ice exceeds the overburden pressure plus an additional pressure component required to initiate the parcicle expantion [Nixon (1991)]. Pressure in the ice is due to the volumetric expansion of water within the unfrozen pore of the frozen fringe, caused by the phase change from liquid to ice (Miller (1972)).

During the freezing process, soil contains water in two phases: ice and liquid. Unfrozen water is assumed always be located between the surface of the porous matrix and the ice. Under the hypothesis of phase thermodynamic equilibrium, the equilibrium for the chemical potential of the two phases results in the Clapeyron equation (Black (1995)):

$$V_w dp_w - V_i dp_i = \frac{\Delta H_{wi}}{T_0} dT \tag{2.1}$$

in which V is the molar volum, p and T are absolute pressure and temperature for the phases water w and ice i. ΔH is the molar heat of fusion at T_0 (273.15 K).

In response to the thermal gradient, a pressure gradient is developed at the two phases interface, defined as *cryogenic suction*. This last drives the pore water in the unfrozen soil towards the freezing front.

On the bases of the Clapeyron equation and under the assumption of isotropic, homogeneous and saturated soil, Thomas et al. (2009) expressed cryogenic suction (S_T), as:

$$S_T = \rho_l L \frac{T - T_0}{T_0} \tag{2.2}$$

in which ρ_l is the pore water density, L the latent heat of fusion, T is temperature and T_0 is the freezing point of pore water (both in Kelvin). Due to the water relocation, the soil below the

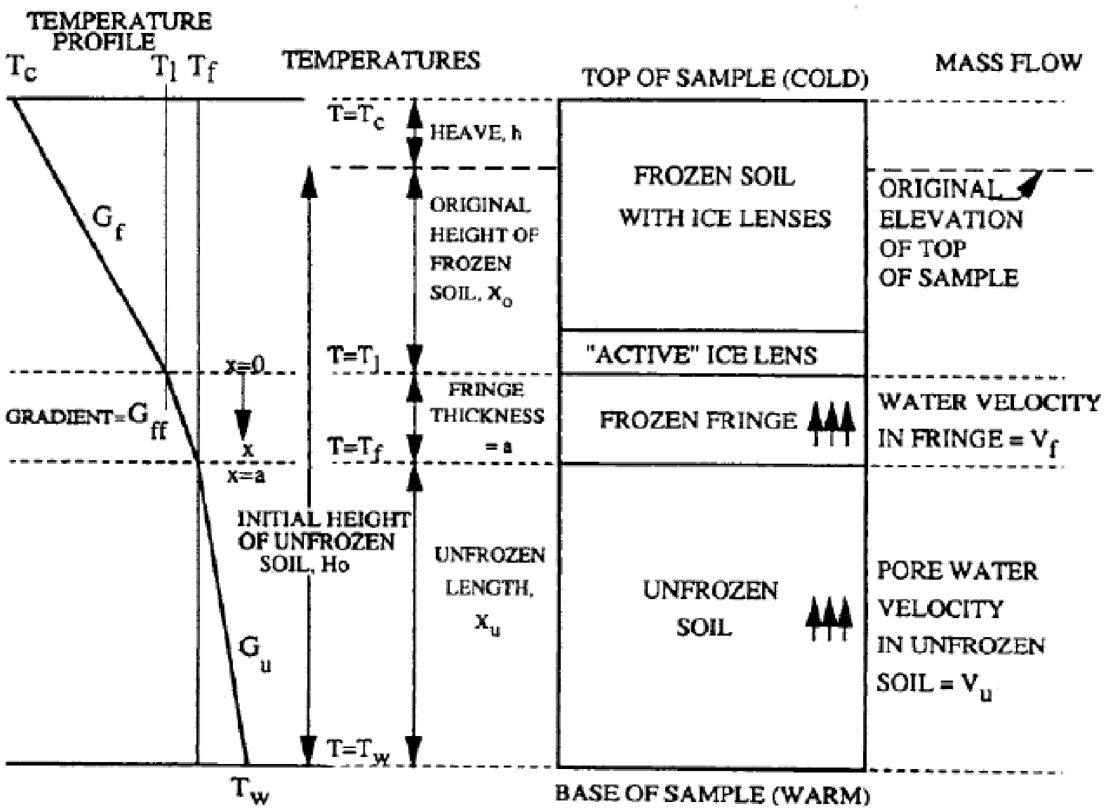

Figure 2.3: Freezing process in one dimensional soil column from Nixon (1991)

frozen fringe zone undergoes consolidation, while positive vertical displacements are measured near the surfaces [Jia (2018)].

2.3 Soil properties changes due to the freezing

Deformation mechanisms in soil upon frost have been analyzed over the years. A considerable amount of researches have been carried out to understand the *Frost heave mechanism*. It is defined as the upwards swelling of soil during freezing condition caused by an increasing presence of ice as it grows towards the surface.

Frost heave results not just from the expansion of the water volume contained in the pores but a supply in water has been observed, when a source of water is available. Furthermore, the amount of surface heaving is found not proportional to the depth of freezing [Taber (1929)].

New techniques were developed in order to study frozen soil deformations. Akagawa (1988) combined conventional frost heave test to X-ray radiography. In such occasion, the techniques matching had a good response. X-ray radiography allowed to see differential expansion of soil layers and ice crystals. A typical X-ray radiograph and temperature profile is visible in Figure 2.4. The width of expansion layer and the expansion rate decreased with time. Finally, between the 0 °C isotherm and the expanding layer, a shrinking layer was observed, putting forward the idea that the water content may not be at saturation in this zone.

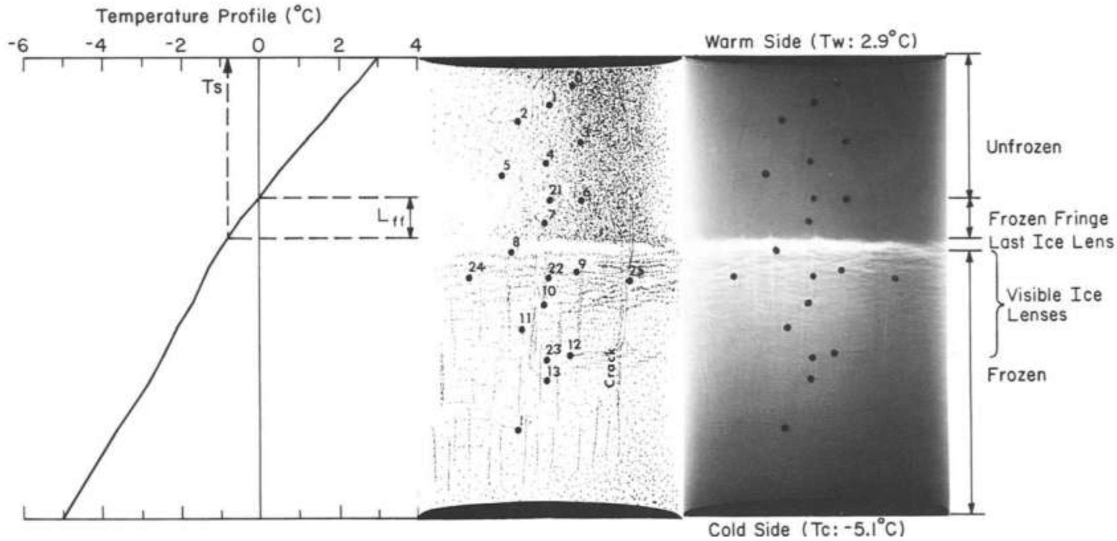

Figure 2.4: Typical X-ray radiograph and temperature profile from Akagawa (1988)

After the soil is frozen, its structure experiences changes; *e.g.*, Chamberlain and Gow (1979) observed vertical shrinkage cracks (much like desiccation cracks), developed because of the large negative pore water pressure that evolves during freezing.

Qualitative observation has been realized about the shrinkage of soil upon freezing. For instance, Chamberlain (1989) observed that in normally consolidated or weakly overconsolidated soils when the soil starts to freeze its volume does not increase but shrink. While, not shrinkage was seen by Ji-Lin and Wei (2006) for the overconsolidated soil, although an expansion was noted once the cold source gets removed.

Structural change and volumetric shrinkage due to freeze-thaw were investigated by Wang et al. (2017), by scanning a saturated clay sample before and after freeze-thaw. The freezing was applied in one-dimensional way. X-ray tomography scans were taken at a spacial resolution of 0.0012 mm^3. Figure 2.5 shows the sample's section obtained after the reconstruction of the scans. During such study, a radial shrinkage of the sample was observed in the top zone of the sample after thawing. A portion at the warm end did not freeze during the experiment. On the basis of the existing knowledge about the cryogenic suction at the freeze fringe, the observation about the pore pressure decrease in the soil beneath the freezing fringe during freezing and the evidence of fissure shape change due to the ice lens formation, the authors state that the cause of the shrinkage is the moisture migration from the warm end to the freezing fringe. The water content was measured after the freeze- thaw process at different elevations of the sample (100 mm in height), for four freezing temperature (2.6) and they indicate a moisture migration from the warm end to the cold end. A densification of the top zone was obtained. During the study the temperature gradient was identified as the main factors controlling the amount of moisture in the same type of soil. Finally, moisture migration was identified causing the radial shrinkage, but not the volumetric one, since the clay was saturated and the system was closed.

As recently observed on unsaturated silty clay sample upon −10 °C three-dimensional freezing by Liu et al. (2019), deformation mechanisms depends on the initial degree of saturation S_r of the soil. In particular, above 75 % S_r soil swells, while if it is less soil shrinks (Figure 2.7).

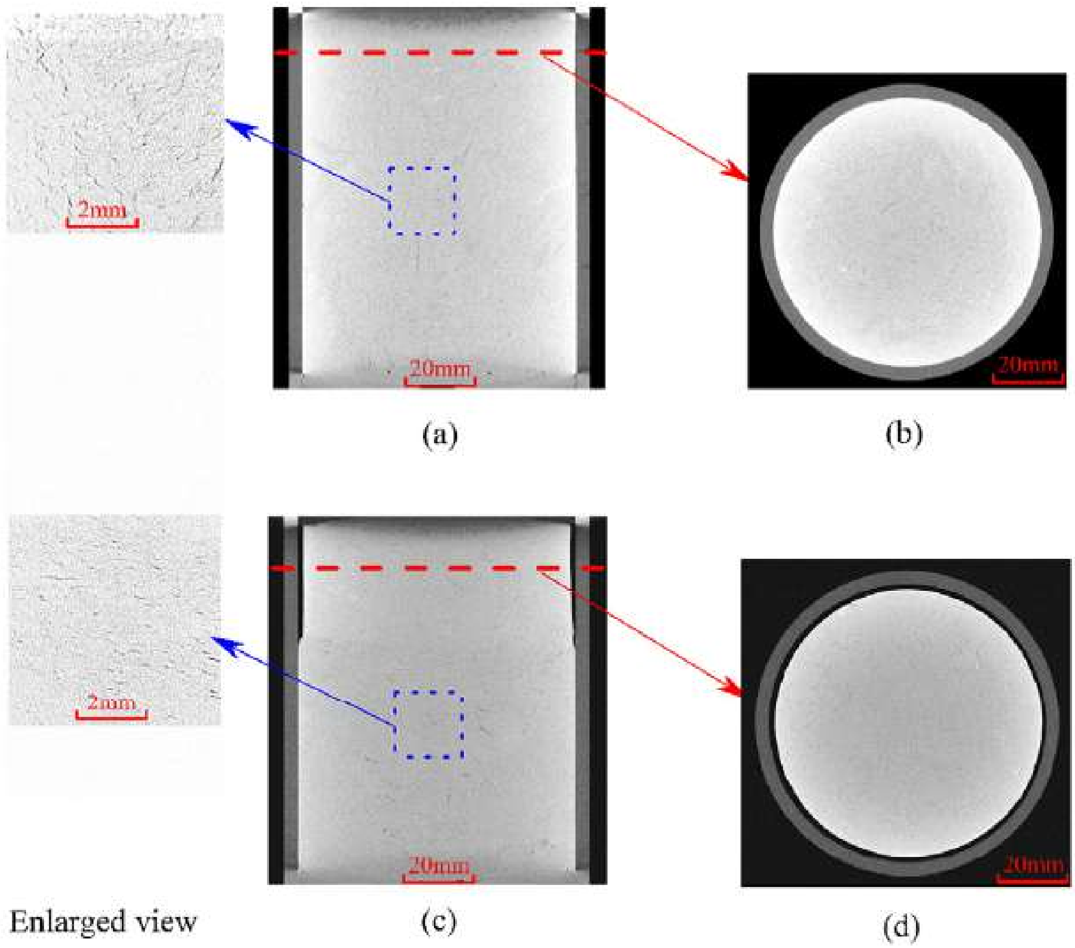

Figure 2.5: 3D image section views before and after freeze-thaw: a) longitudinal before, b) horizontal before, c) longitudinal after and d) horizontal after from Wang et al. (2017)

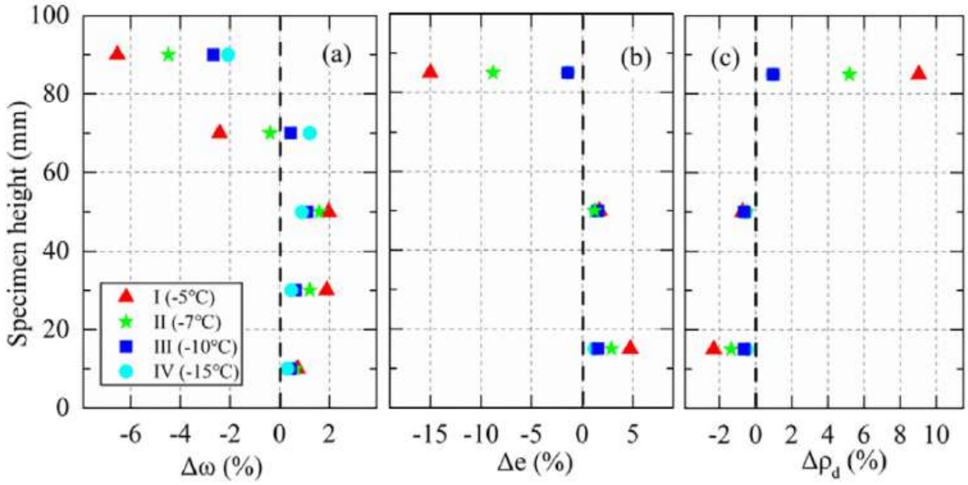

Figure 2.6: Moisture content, void ratio and dry density variation along specimen height after freeze-thaw experiments under four freezing temperatures from Wang et al. (2017)

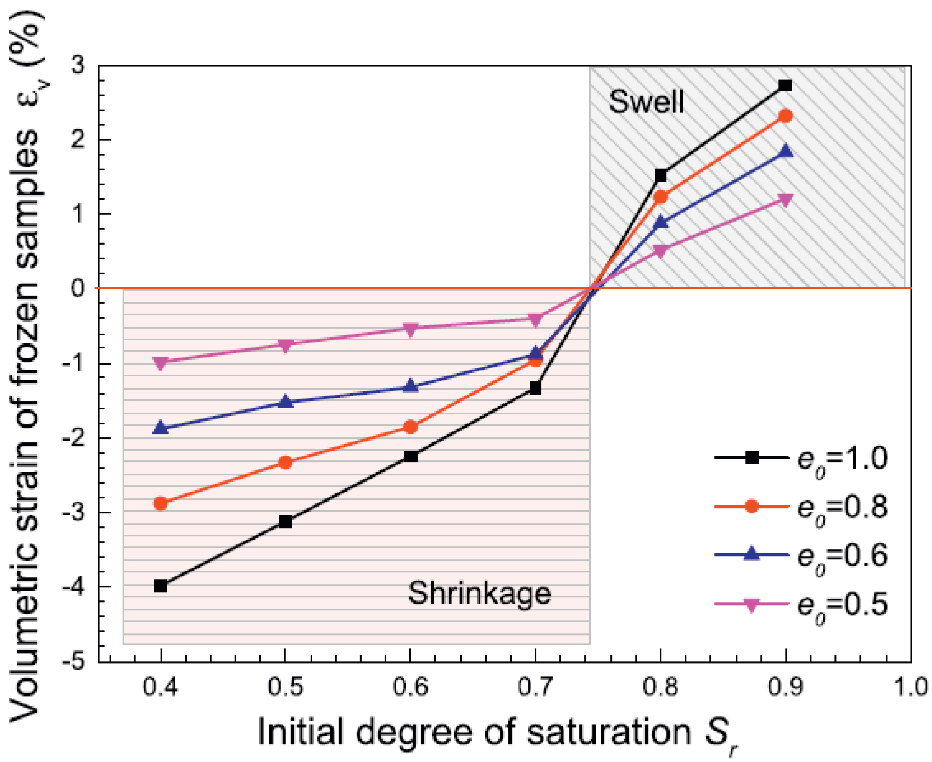

Figure 2.7: Volumetric deformation vs. initial degree of saturation from Liu et al. (2019)

Chapter 3

X-ray tomography for experimental geomechanic

During the last two decades, x-ray tomography has been more and more required in experimental geomechanics for the study of geomaterials. X-rays allowed to understand the failure mechanism of soil and rocks and to understand how natural processes take place in soils. For instance, tomography scans were taken to see the bean seed growth in sand and ice lenses in frozen soil [Viggiani et al. (2014)]. Current study are investigating the roots development in soil using x-rays. Furthermore, several information about the mechanical behavior of granular materials have been obtained by combining x-rays and mechanical test for geomaterials.

3.1 X-rays

X-ray were discovered by the German physics professor Wilhelm Röntgen on November 8, 1895 [Stanton (1896)]. They are electromagnetic radiations that exist in a certain range of wavelength and frequency values in the electromagnetic spectrum (λ = 0.01 ÷ 10 nm; f = 1016 ÷ 1020 Hz). As every type of radiation, they consist of photons, which are individual packets of energy. X-ray distinguish in soft and hard X-Rays depending on their energy level. Soft X-Rays have lower energy and they can be easily absorbed (frequency range ≈ 1016 ÷ 1018 Hz; higher λ values), whereas hard X-Rays have higher energy and penetrate matter much more easily (frequency range ≈ 1018 ÷ 1020 Hz; lower λ values).

X-rays are generated by an x-ray tube. It is a vacuum tube and it contains a cathode and a anode. The cathode correspond to a low atomic number metal (*e.g.*, brass) and it is connected to the high tension circuit. The anode is placed in the opposite side of the tube and it corresponds to a high atomic number metal (*e.g.*, tungsten). The cathode is heated and then it releases electrons for thermoionic effect. The cloud of electrons are accelerated and as they hit the anode. The collision transforms the kinematic energy into heat and x-rays [Wikipedia (2019)]. The scheme of the x-ray tube is shown in Figure 3.2.

Two physical ways exist for producing x-rays [Viggiani (2018)]:

1. by change of orbit of electrons coming from electronic shell: the transition of the electrons between shells produces x-rays photons;

2. by changing the speed of electrons (*i.e.*, braking and change of trajectory). It happens when electrons pass close to a nucleus or through a magnetic field. In these occasion electrons are attracted so they lose a part of their energy, emitting x-ray photons (figure 3.1).

The main characteristics of an x-ray beam are:

1. Energy (eV): capacity to penetrate matter;

2. Intensity (photon/sec): photon flux;

3. Convergence (rad) : ray geometry;

4. Size (m)

Intensity, Convergence and Size of the beam affect the Brilliance, which is expressed in $photon/sec$, per mm^2 of the beam size, per $mrad^2$ of the open angle and for band width of 0.1% of the energy considered. The higher the brilliance, the more powerful the system [Viggiani (2018)].

3.2 X-ray tomograph

Since long time, the tomograph has been used as an non-invasive medical device used to visualize anatomy of the human body and to investigate about the health of organs, bones and tissues. The

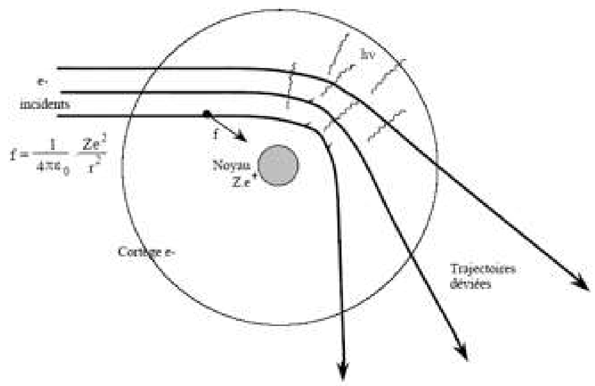

Figure 3.1: Change of trajectory of electrons due to the presence of a nucleus from Viggiani (2018)

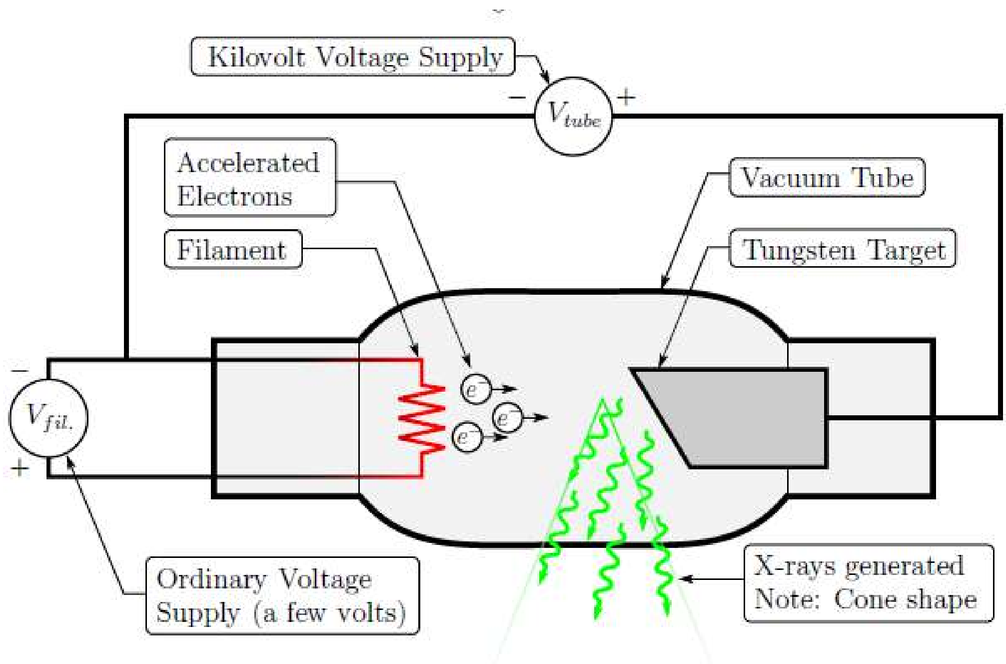

Figure 3.2: X-ray tube scheme from Andò (2006)

patient needs to be lying on the bed while the scanner is turning around body, shooting x-rays at the body zone to investigate (Figures 3.3 and 3.4).

The tomograph in 3SR laboratory (Figure 3.5) is used for experimental geomechanics and it consist of a source and a detector which are fixed, while the body turns thanks to a turntable (Figure 3.6).

The source contains the X-ray tube, which produces an x-rays cone-beam (see 3.1). The

Figure 3.3: Medical device for x-ray tomograph scans

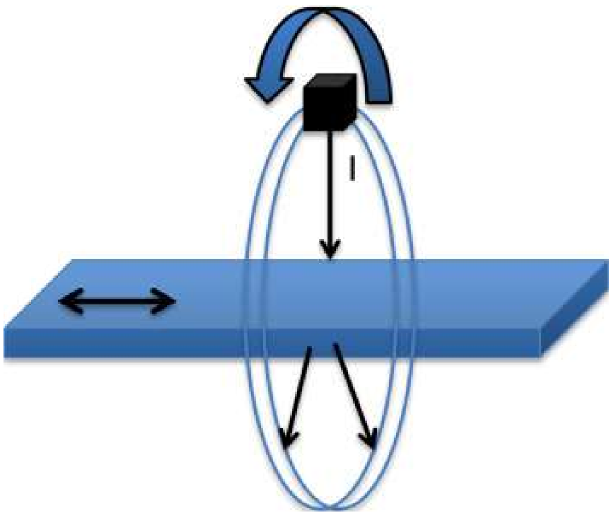

Figure 3.4: Medical tomograph's scanning scheme form Love (2017)

beam is shoot against the specimen and the detector measures the x-ray attenuation due to the specimen crossing. The detector of 3SR laboratory's tomograph is a flat-pannel devise, *indirect* in type, marketed for medical use. It works using a similar technology of image sensors in digital photography and video. *Indirect* detectors contain a layer of scintillator material, typically either gadolinium oxysulfide or cesium iodide, which are able to convert the incoming photons (x-ray) into light (Figure). An amorphous silicon detector array is directly behind the scintillator. It is manufactured using a process very similar to that used to make LCD televisions and computer

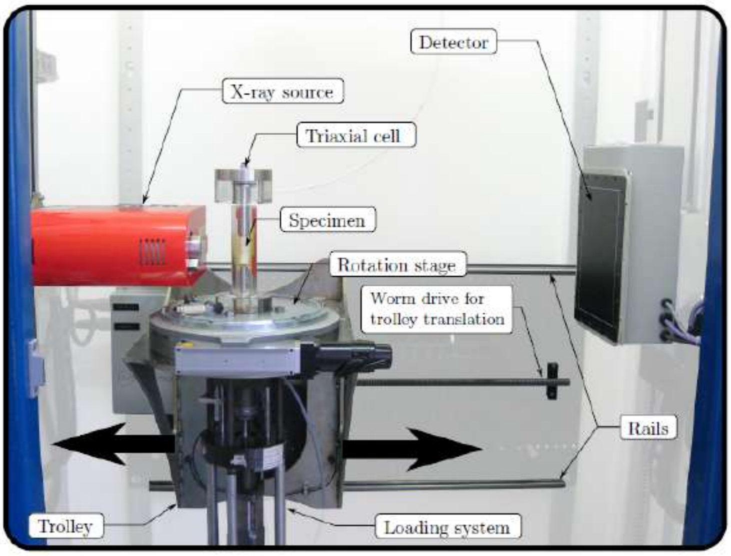

Figure 3.5: 3SR laboratory's Tomograph from Andò (2006)

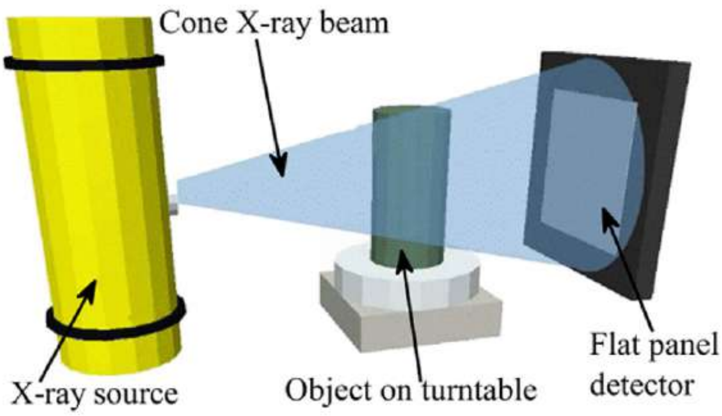

Figure 3.6: 3SR tomograph's scanning scheme from Wang et al. (2017)

monitors [Kump et al. (1998)]. The scheme of an *indirect* detector is shown in Figure 3.7.

Detector contains millions pixels and, similar to a digital camera's image sensor chip, each pixel also contains a photodiode which generates an electrical signal in proportion to the light produced by the portion of scintillator layer in front of the pixel. The signals from the photodiodes are amplified and encoded by additional electronics positioned at the edges or behind the sensor array in order to produce an accurate and sensitive digital representation of the x-ray image [Kotter and Langer (2002)].

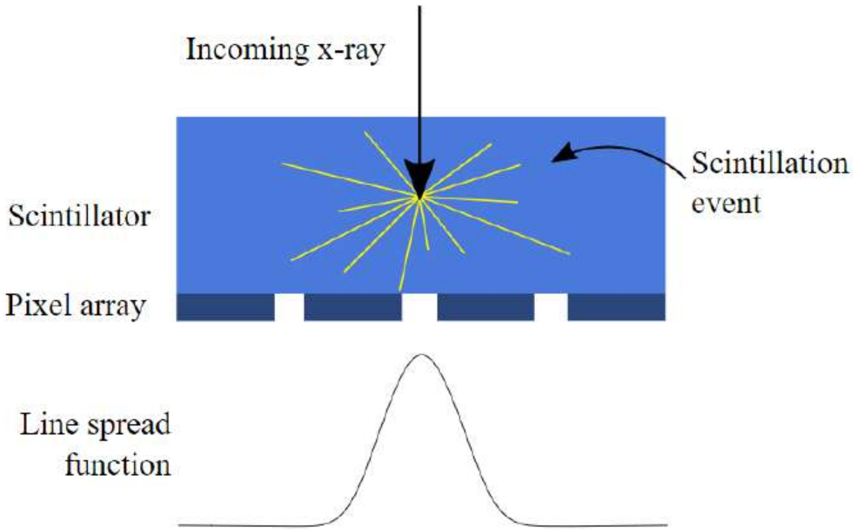

Figure 3.7: Indirect detector scheme from Commons (2017)

3.3 Images acquisition

Tomography allows to have a three-dimensional image of an object, called *Tomogram*. Once this image is obtained, the object scanned can be sectioned in whatever direction to look inside it. The *Tomogram* is obtained by taking several radiographs of the object at different angular positions. Indeed, during the scanning the specimens turns since the support, on which it is placed, rotates. Knowing the specimen's center of rotation, the horizontal sections (slices) of the specimen are first reconstructed and then the whole volume is obtained by a slice by slice reconstruction (Figure 3.8).

Detector measures an x-ray attenuation field due to the crossing of the object placed between the source and the detector. X-ray photons may interact with the object's matter through different mechanisms (*e.g.*, Compton Scattering, Refraction and Reflection, Pair Production, Raleigh Scattering). For soils and the energy of x-ray radiation used, the overarching mechanism of interaction of x-rays with the material is photoelectric absorption. In a photoelectric absorption event, an x-ray photon is absorbed by an atom, which causes an electron to be ejected.

The absorbed photon's quantity depends on the beam energy and on the material density and it follows the the Beer-Lambert law:

$$I = I_0 e^{-\mu\rho x} \tag{3.1}$$

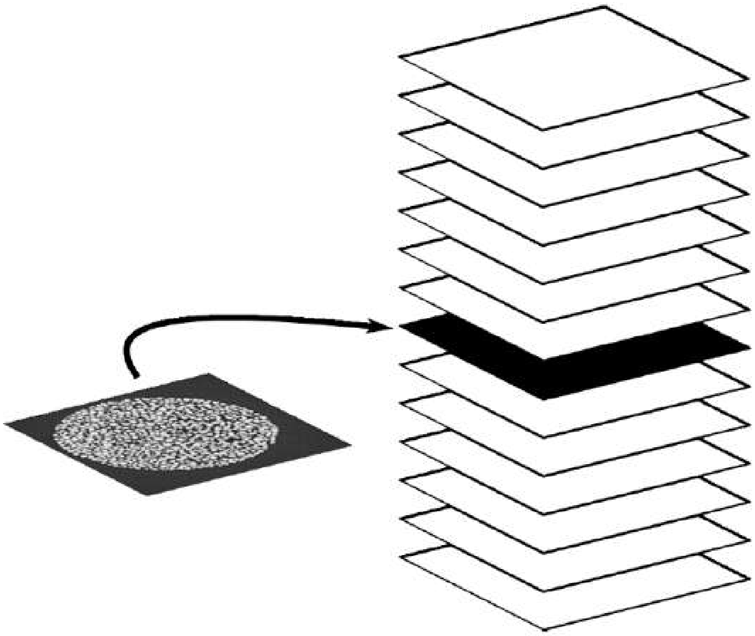

Figure 3.8: Reconstruction of horizontal slices

where I_0 is the Intensity of the beam measure when nothing is in between the source and the detector, μ is *attenuation coefficient* related to a given energy, ρ is the material density; x is the length of the crossed object.

Before starting the test, the detector needs to be calibrated by measuring the term I_0.

In terms of digital images, *spatial resolution* refers to the number of pixels utilized in construction of the image. Images having higher spatial resolution are composed with a greater number of pixels than those of lower spatial resolution [Kenneth et al. (2019)]. The spacial resolution is expressed in μm/pixel and it is chosen depending the specimen size. On the basis of the X-ray Collimator aperture D, the distance between Collimator-Object L and the distance of Object-Detector l (Figure 3.9), the spacial resolution could be changed following the formulation:

$$d = \frac{l}{L/D} \tag{3.2}$$

The detector has a fixed number of pixel of a certain size in μm, but its effective size can be changed by translating the support, on which the specimen is placed, between the source and the detector (Figure 3.5).

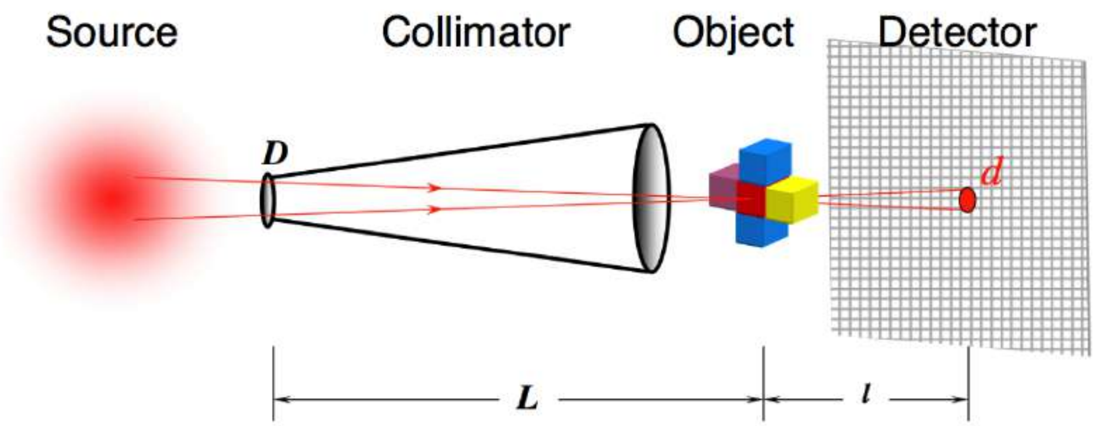

Figure 3.9: Significant quantities for the spacial resolution

The spot size depends on the power of the x-ray source. Smaller spot size is achieved by reducing the power of the x-ray source. To have good images, once the beam's intensity is reduced, the exposure time for acquisition of radiographs needs to be increased in order to use enough of the detector's dynamic range [Andò (2006)].

Chapter 4

Tested soils and specimens preparation

Materials used during this research project are Halden silt and Ønsoy clay. Since no enough amount of natural soil was available to test the freezing processes planned in the experimental campaigns, reconstituted specimens were made. The analysis of freezing processes needs specimens to be homogeneous and isotropic,then several reconstituting sample procedures were tested, in order to find the one which returns the most uniform material.

4.1 Halden silt and Onsoy clay: Frost susceptible soils

Susceptible soil are defined by Atakol (1969) such us soil ”in which significant ice segregation will occur when the requisite moisture and freezing conditions are present”. Several methods were proposed to test and classify frost heave susceptibility of soils based on particle size, pore size characteristics, mineralogy, hydraulic conductivity, moisture content and availability, density and freezing conditions [Chamberlain (1981)]. The ISSMGE Commitee in 1989 proposed a classification of frost-susceptible soil based on the grain size distribution curve (Figure 4.1). Following this classification, soil can be defined as frost susceptible (FS) if its grain size distribution completely falls in the region 1 of the graph in Figure4.1, while they are not when it is in regions 2, 3 and 4. Soils in region 1L have low susceptibility and particular attention should be paid for the borderline cases ([Slunga and Saarelainen (2005)].

Halden silt and Onsoy clay are two Norwegian kind of soils, whose grain size distribution curves are shown in Figure 4.2. The main part of such curves stands in region 1, hence they are frost susceptible soils.

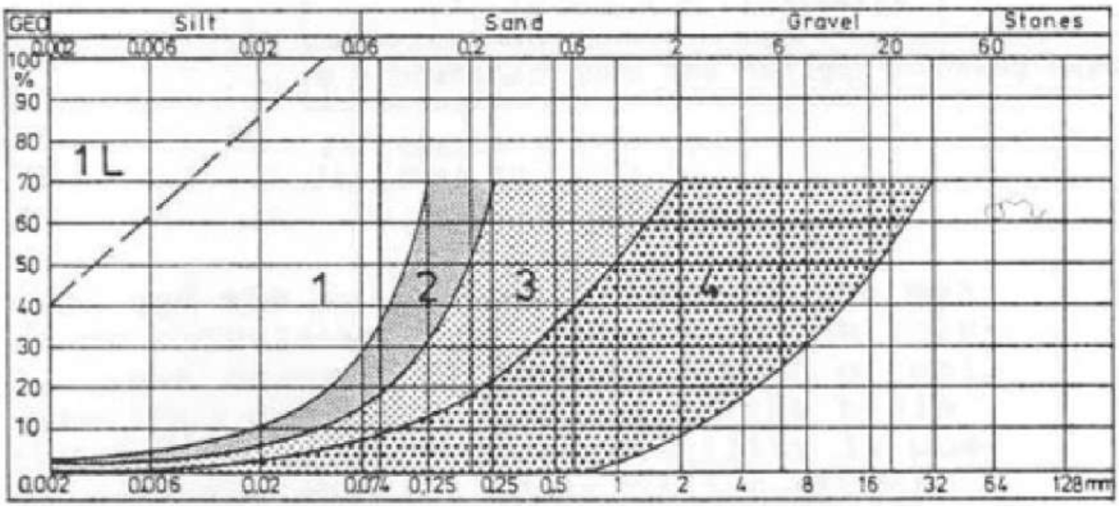

Figure 4.1: Frost-susceptibility of soil based on the grain size distribution curve from Slunga and Saarelainen (2005)

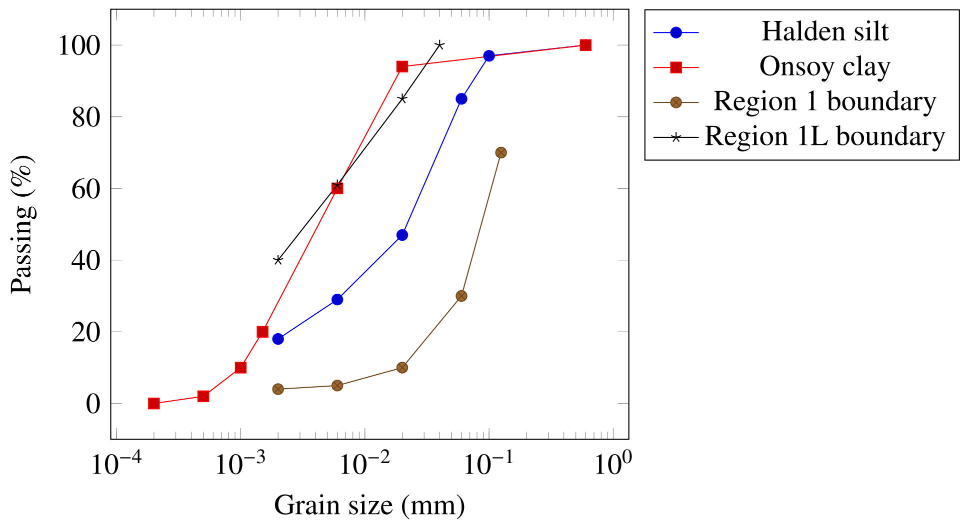

Figure 4.2: Grain size distribution of Halden Silt from Blaker et al. (2016) and Onsoy clay from Müthing et al. (2017)

4.2 Natural soil sampling and remolding procedures

Halden silt specimens were made by coring the material from a cylindrical block of silt extracted in Norway. To compensate the slight drying due to the travel from Norway to France, the sample was saturated back. Once cored, the specimen was place on a porous stone in contact with water and left in this condition for 24 hours. In this way it retook water thanks to the capillarity raise. In the case of Ønsoy clay, the material arrived in the shape of cylindrical disturbed samples and cubic block. Due to the lack of enough natural clay specimen to realize the planned tests for the experimental campaigns, artificial clay samples were made afterwards by remolding the natural ones.

No Standard explains which is the best way to remould and make representative clay specimens. In literature many procedures have been adopted and identified as good solution for the clay in hand. Burland (1990) defined reconstituted clay as “one that has been thoroughly mixed at a water content equal to or greater than the liquid limit w_L”. De Sheeran and Rj (1971) suggest to make homogeneous clay sample by use 2.5 times the liquid limit. Penumadu and Dean (2000) prepared reconstituted sample by remoulding first intact material at a moisture content of 1.8 times the liquid limit with the addition of deionized water, then, once it has been de-aired, the slurry is one-dimensional consolidated.

The main problem found following such procedures was the presence of air bubbles left in the final sample after consolidation. Air bubbles are incorporated at the slurry during the mixing and the pouring process. Air bubbles affects the freezing process since they corresponds a preferential location for the initiation of ice segregation. Furthermore, recent study have revealed that water can infiltrate into deeper soil through preferential pathways where air-filled macropores exist at the time of freezing [Niu and Yang (2006)] The discovery of such inhomogeneities in the specimen was made thanks to the use of the x-ray tomography scanner. Several trials were done and a good procedure was found to obtain homogeneous clay specimens.

However, before freezing, in any cases reconstituted cylindrical specimens are placed between metal end caps and put in latex membrane and this two last are keep fixed by o-rings. Membrane is used to get soil impervious while caps are of metal to allow the thermal flux and to no affect the freezing. Specimen is introduced in membrane using triaxial cell mould. Once the membrane is placed inside the mould and gets adherent to the metal by vacuum, the specimens is carefully make slide into the membrane. Afterwards, specimen's equipment is completed by metal cups and o-rings.

In what follows, the different specimen reconstitution methods are explained.

1. A first trial was conducted on Kaolin clay powder. Demineralized water was added to the powder in the ratio 1,5:1, the manually mixed slurry (Figure 4.3 a.) was then reversed into the consolidometer (42mm in diameter) by a spoon and subjected to 42 hours vacuum (Figure 4.3 b.). Afterwards, the slurry was one-dimentionally consolidated at 60 kPa (Figure 4.3 c.). The water in the slurry could drain both from the top and the bottom of the consolidometer. The consolidation pressure was gradually increases in step during a period of 27 h until 60 kPa, following the step 5 kPa, 10 kPa, 15 kPa, 30 kPa and 60 kPa. For each step the vertical pressure was increased when the pore over-pressure was totally dissipated, *i.e.*, after the vertical settlement at that step was over. As Figure 4.3 d. shows, after took the sample out from the consolidometer the surface of the specimen appeared extremely rough because of left cavities between soil and consolidometer's wall.

2. In order to avoid a nonuniform surface and obtain smaller air babbles, some adjustments were made for the second trial. The water content was increased from 1,5 to 1,8 the liquid limit to get a less viscous slurry and this latter was squeezed into the consolidometer (42mm in diameter) by *sac à poche*, so that air is not trapped between one scoop and the following one. The vacuum step was skipped because considered not working due to the high viscosity of the mixture. The vertical consolidation pressure was increased to 200 kPa, following the step 20, 70, 100, 150, 200 kPa . After consolidation, the specimen surface appeared less rough, but inside small air bubbles were still evident, as visible from the sample's vertical section shown in Figure 4.4, captured by x-ray tomography scanner.

3. Unlike Kaolin clay, Onsoy clay samples were not reconstituted from powder but starting from natural clay. In this case water was added until an homogeneous paste was obtained. The final water content of the mixture was w=57%, while its liquid limit was found w_L=65%. The consolidometer (70 mm in diameter) was filled by soil using palette knife, taking care to create no voids in the specimen. This latter was then subjected to 96 hours consolidation at 57 kPa (similar to the pressure at the sampling depth to the *in-situ* pressure).

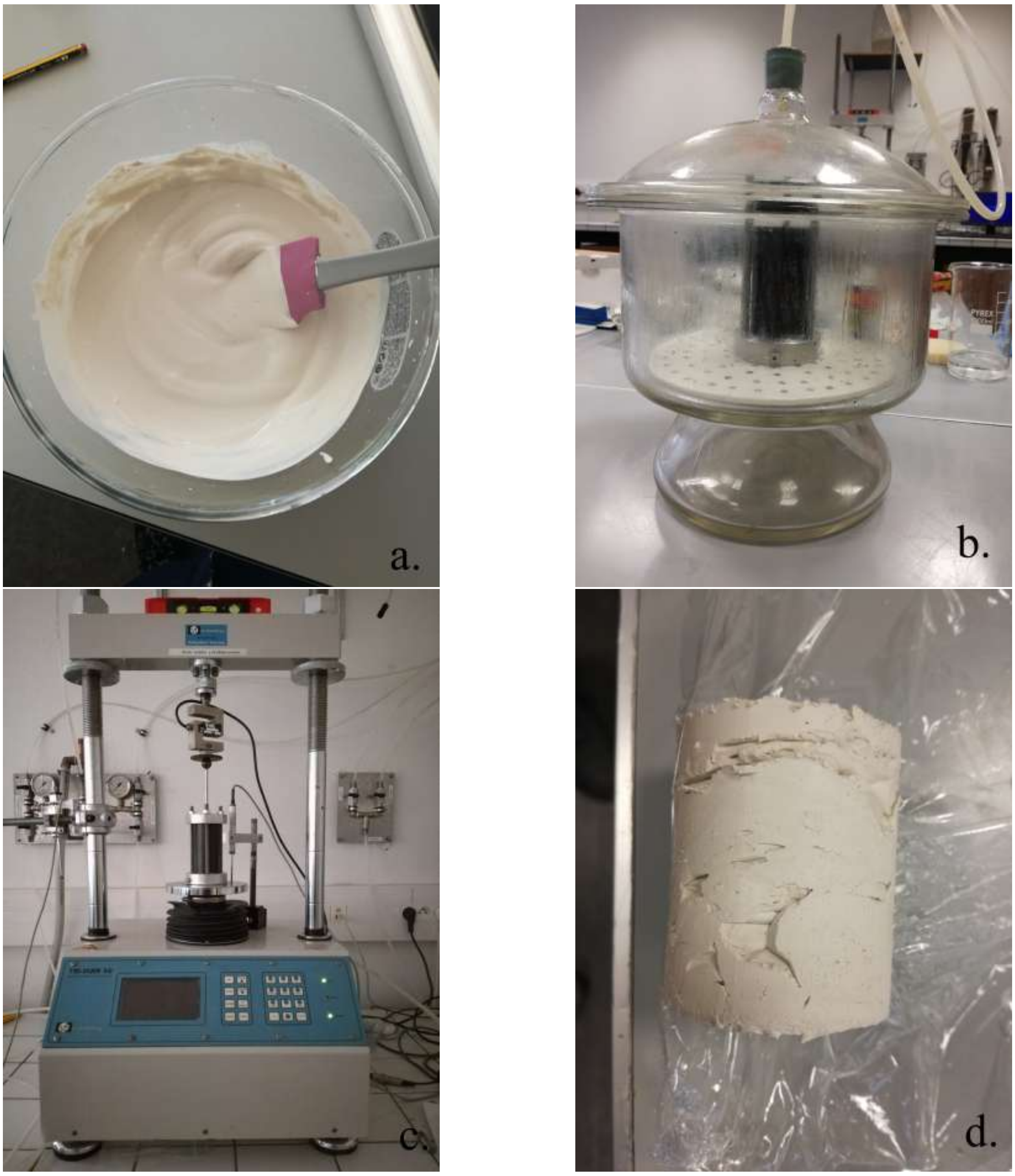

Figure 4.3: Procedure 1: a. Slurry, b. Vacuum chamber, c. One-dimensional consolidation, d. Kaolin clay reconstituted specimen

The final sample was 70 mm in diameter and 61 mm in high. In figure 4.5 is shown the vertical section of the specimen, captured by x-ray tomography scanner. Several voids with different sizes still exist inside the sample.

4. Finally, the best procedure to make clay samples, found and suggested in this research

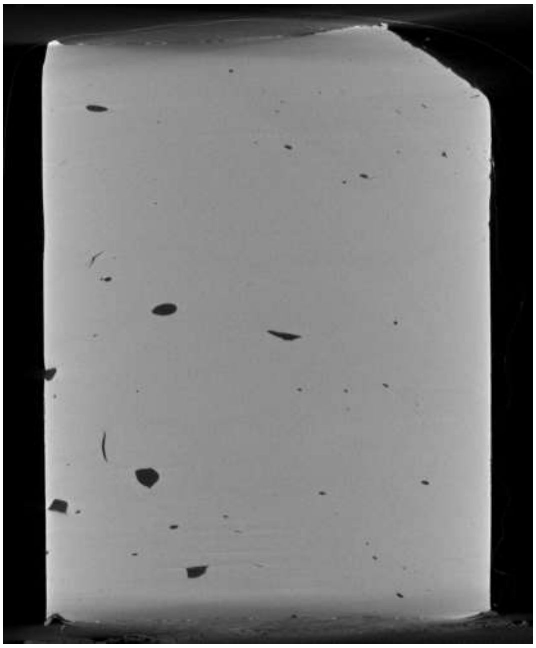

Figure 4.4: Vertical section of reconstituted clay by Method 2

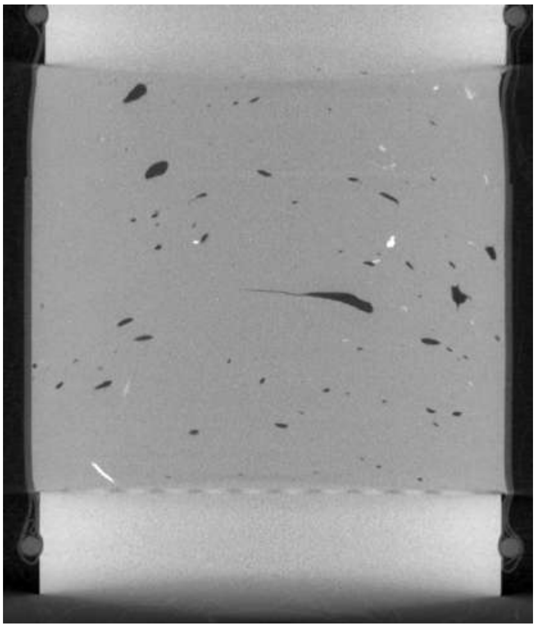

Figure 4.5: Vertical section of reconstituted clay by Method 3

project, is the following one. An homogeneous mixture of a high viscous liquid (Figure 4.7 a.) is obtained by adding water until the water content is slightly above the liquid limit, *i.e.*, when at the Casagrande apparatus (Figure 4.7 b.) the number of blows are a little less than

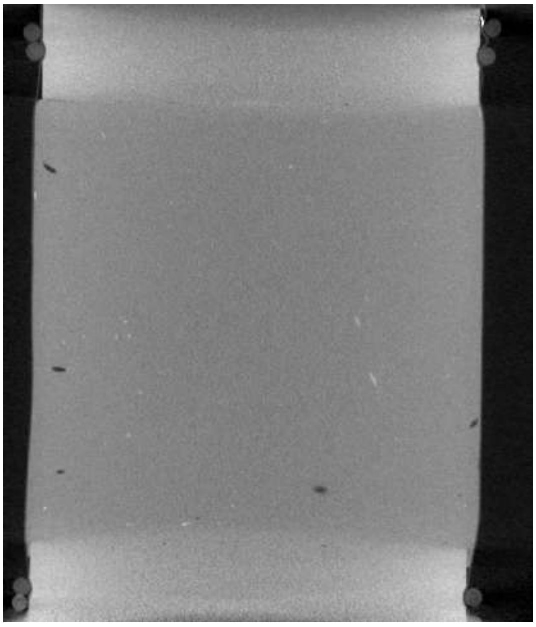

Figure 4.6: Vertical section of reconstituted clay by Method 4

25 [Lambe (2006)]. By this time, the mixture can be put into the consolidometer using spoon. Filter papers are placed at the bottom and at the top, once the mixture is ready for being consolidated. The removing of air bubbles is achieved by the use of a concrete vibrator (Figure 4.7 c.) moved around in the clay for a couple of minutes. Vibration make the soil around the vibrator liquid, allowing then air bubbles to rise and escape from the mixture. A good quality clay sample is so obtained after a one-dimensional consolidation in oedometer, as shown in Figure 4.7 d. The water contents achieved by samples before consolidation was between 67% and 72%. After 72 hours of one-dimentional consolidation the water contents varied between 51% and 55%. The variation in achieved water content was due to variable piston friction in the consolidometers used. An example of vertical section of an Onsoy clay specimen obtained following such procedure is in Figure 4.6.

However, before freezing, the reconstituted cylindrical specimens are placed between metal end caps and put in latex membrane and this two last are kept fixed by o-rings. The membrane is used to separate the samples from the cooling liquid in the freezer, while the purpose for the metal end caps is to provide a firm support for rings and to allow the thermal flux, without affecting the freezing. The membrane is placed using a triaxial membrane stretcher. Once the membrane is placed inside the mould and gets adherent to the mould by vacuum, the specimens is carefully slid into the membrane. Afterwards, specimen's equipment is completed by metal cups and double o-rings.

Figure 4.7: Procedure 4: a. Mixing, b. Casagrande apparatus, c. Concrete vibrator, d. Oedometer consolidation

4.3 Air bubbles detection

Computation of number and size of air bubbles inside specimens using the usual laboratory tools is not simple, so the comparison among the different sampling procedures was realized by the use of The Software for the Practical Analysis of Materials (SPAM). SPAM is a software made to handle x-ray tomography data, having strongly application in the field of science material. With its package of Python functions SPAM allows to compute full-field displacements and strain, changes in volume, porosity fields and it offers many other functions which can be used for mechanical applications [Int (2019)].

Detection of air bubbles was realized by implementing a code, already written in SPAM to detect the particle size of granular materials. Once the 3D image are taken by x-ray tomograph and upload in the code, it is prepared for the pores detection. First a threshold is applied in order to isolate air bubble from the soil. The extreme values of the threshold were identifies on the basis of gray value frequency of the image. Then, a cylindrical mask is applied on the image to delete what is outside the specimen. The soil texture is identified, dilated and its gray value is imposed equal to zero. In the resulting image pores are isolated. Then, the function *watershed* identify each single pore and label it, returning the numbers of pores. Volume of pores is finally computed by the function *volumes*, which count the number of voxels, whose each label is made of. The background is labeled as well and its volume was identified and subtracted and the analysis. Such technique is able to detect an object at minimum 2x2x2 voxels in size. On the assumption of spherical air bubbles, as they commonly appear, it is possible to obtain the diameter of each pore. Furthermore, knowing the total air volume (V_V) and the sample's volume (V_{TOT}), it is possible to calculate the air bubble porosity as:

$$\phi = \frac{V_V}{V_{TOT}} \tag{4.1}$$

In Figure4.8 histograms show diameters and numbers of air bubbles inside the reconstituted specimen obtained by Method 2, 3 and 4. For the different methods, table 4.1 shows the air bubbles porosity, the amount of air bubbles and their greater size (expressed in term of diameter). Method 2 involves in specimens full of tiny air bubbles dispersed in the solid matrix. Despite of for the Method 3 and 4 the specimen's size is twice the previous one, the amount of pores decreases respectively of 2 and 4 times. Method 3 involves in higher porosity and it globally contains bigger air air bubbles than the other case. The best reconstituting procedure is so identified in the Method 4 since it leads to lower porosity and less amount of pores than the other cases. All the tested in this project were carried out on specimens prepared by Method 4.

Table 4.1: Reconstituted specimen's pores properties for Method 2, 3 and 4

Method	Air bubbles porosity (%)	Number of air bubbles	Maximum diameter (mm)
2	2,2	1100	4.1
3	7,7	559	25,2
4	1,1	273	7,4

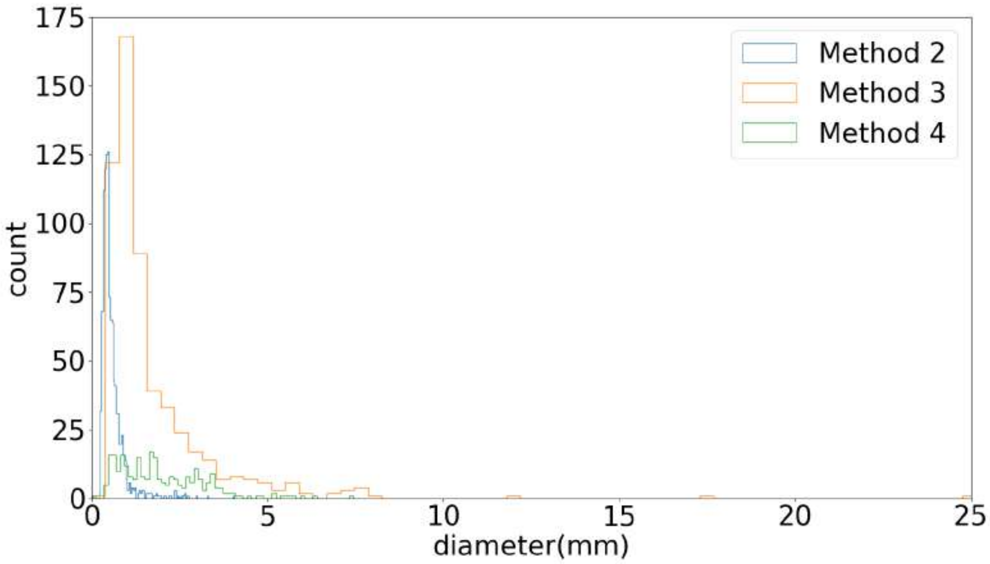

Figure 4.8: Number of air bubbles vs. diameter fo Methods 2,3 and 4

Chapter 5

Three-dimensional freezing processes

Mechanical tests on frozen soils are usually carried out on artificial frozen specimens. As we have see in the literature review, frozen clay and silt soil naturally tend to segregate and get dispersed into a matrix of ice. In this conditions, mechanical tests responses would be the sum of the response of two different phases, the frozen soil and the ice. To obtain the actual behavior of frozen material, avoid the existence of ice lenses is needed.

Literature presents many different ways in which the frost is applied on the unfrozen soil before the test is run. Wang and Nishimura (2017) froze the specimen (reconstituted Kasaoka Clay) at $-15\,°\mathrm{C}$ for 12 hours and then changed the temperature to -2, -5 or $-10\,°\mathrm{C}$ before the triaxial compression tests. Before the creep test on loess, Xu et al. (2017) cooled the specimen for 48 hours down to the testing temperature (-2, -4 , -5 and $-7\,°\mathrm{C}$). To investigate the strength and deformation characteristics of frozen sandy soil, again Xu et al. (2011) decided to mono-dimensional freeze the specimen quick from the top to the bottom under $-30\,°\mathrm{C}$, to avoid frost heave and the specimens were considered completely frozen after 48 hours.

In the following sections three-dimensional freezing procedures are applied to Halden silt and Onsoy clay natural and reconstituted specimens. Comparisons between the frozen and the unfrozen state are done after taking x-ray tomography scans.

5.1 Topology of ice formation

The topology of ice formation during freezing was explored by Viggiani et al. (2014). They applied air 24 h of air freezing at −18 °C on remolded samples of fine Fontainebleau sand, kaolinite clay and bentonite clay. Kaolinite and bentonite specimens were prepared at initial water contents equal to their liquid limits. Samples were prepared just putting the material into a Plexiglas cylinder, resulting in sample 80 mm in diameter and 110 mm in height. The samples were frozen and then scanned at a spacial resolution of 50 μm/voxel. Figures 5.1 show the horizontal section of the frozen samples. The sand specimen shows no evidence of ice segregation. Lenses grew inward from the specimen boundary in the kaolinite specimen. The bentonite specimen was massively crisscrossed by ice lenses. The density profile was computed across one of the ice lens of the kaolinite clay specimen (Figure 5.1). It shows a relatively constant density in the soil mass next to lenses. The absence of a density gradient in the soil close to lenses suggests that cryogenic suction-driven consolidation has been completed and the scans were taken when the samples were in steady-state equilibrium. Furthermore, it was found that the ice lens formation is a three-dimensional phenomenon.

5.2 Halden silt testing procedures

Large thermal gradient in 3D freezing is considered leading to an in-homogeneous tensional state. Temperature at the specimen surfaces decreases while the core keeps the initial one, then voids could open between these two phases. In this section, to avoid the just described situation, two gentle freezing procedures were applied on cored Halden silt specimens (Section **??**).

A plastic container, full of refrigerant liquid with a freezing point of −30 °C, was used as freezing chamber and the specimens (in cling foil wrapped) were cooled down in the following ways:

1. The refrigerant liquid was preventively cooled down to −12 °C, specimen was then placed into the container and the temperature of the whole system was kept at −12 °C by freezer for 24 hours.

2. The specimen was placed into the container, where refrigerant liquid was at 12 °C, then the whole system was cooled down to −12 °C by freezer for 24 hours.

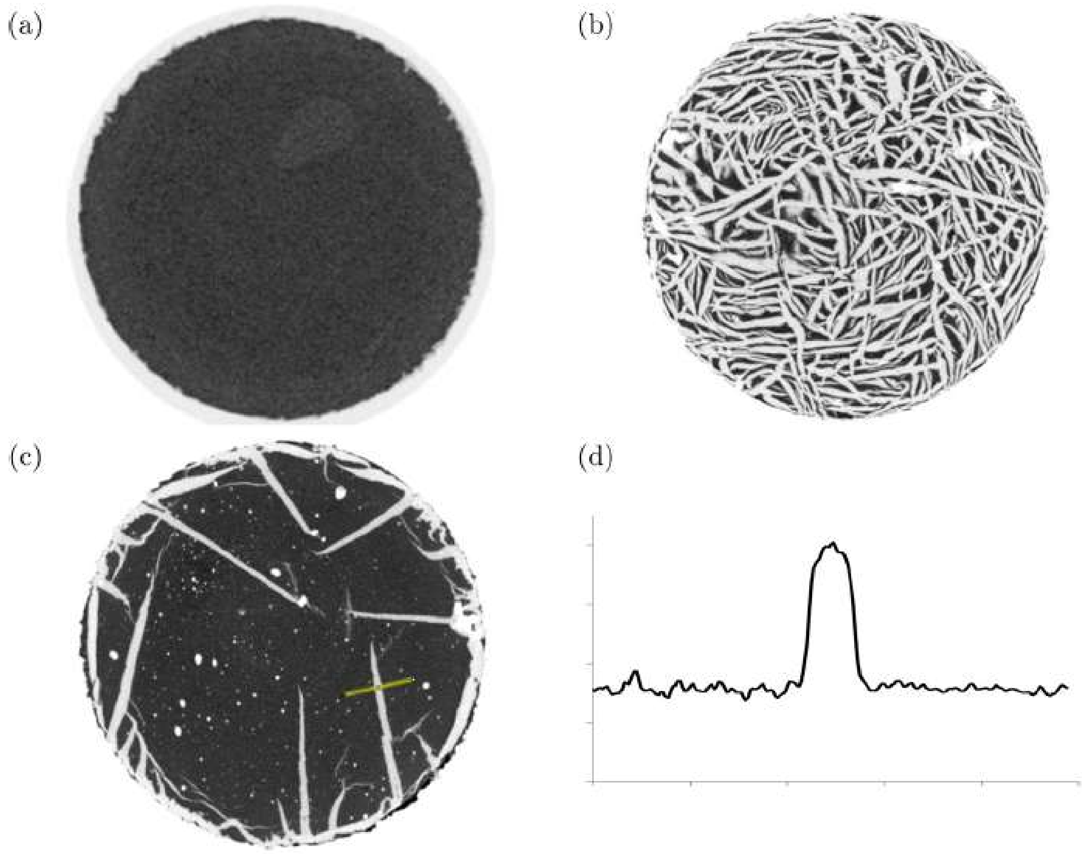

Figure 5.1: Horizontal section frozen specimen: a. fine Fontainebleau sand, b.bentonite clay and c. kaolinite clay, d. density profiles shown across an ice lens in the kaolinite specimen

The tomography scans show no clearly visible ice crystals for the first case (Figures 5.2 and 5.3) , while thin ice lenses at the boundary appear in the second one (Figures 5.4 and 5.5). If the first procedure seems to be preferable for experiments, the second one could be also adopted if the core of the sample is used.

5.3 Onsoy clay testing procedures

Freezing processes applied to natural and remoulded Onsoy clay specimens can be divided in *fast* and *slow freezing*.

Fast freezing was achieved by air freezing and it was imposed on natural disturbed samples with 55% in water content. Two experiments were carried out:

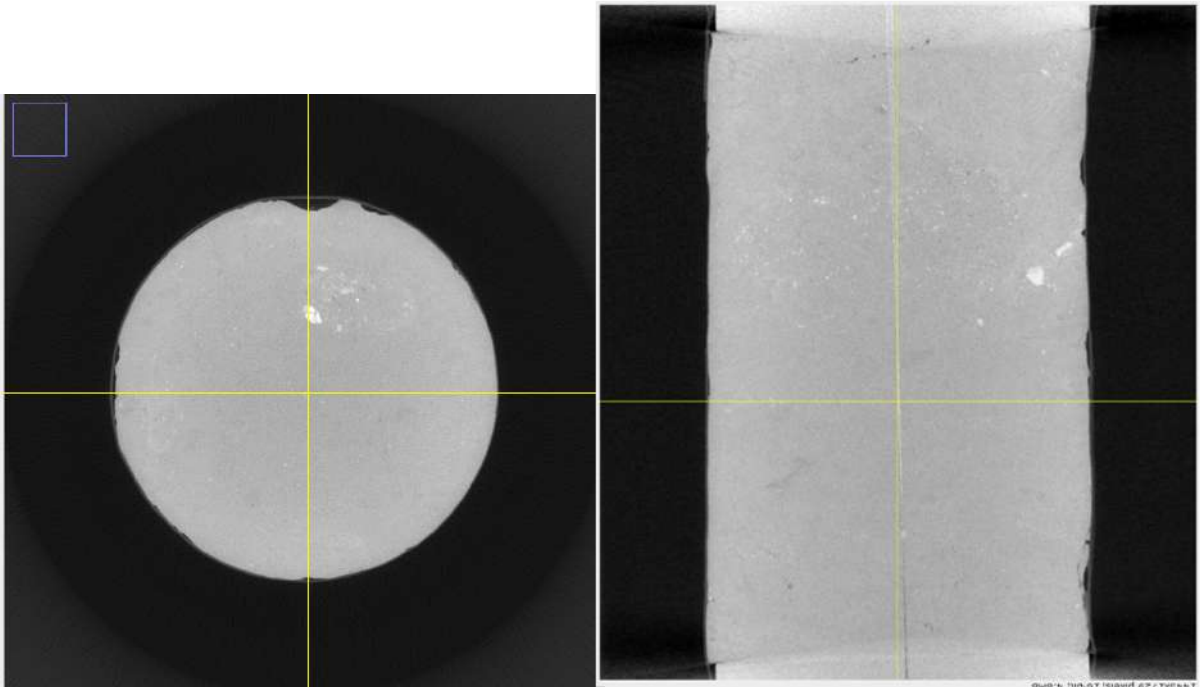

Figure 5.2: Halden silt specimen's horizontal and vertical section in unfrozen state for Freezing 1

1. 24 hours air freezing at $-12\,°C$;

2. 24 hours air freezing at $-20\,°C$;

Before and after freezing, each specimen was scanned at a spacial resolution of 60 and 65 μm/voxel, respectively. Since scanning took almost 40 minutes, frozen specimens were placed in isolation chamber(16 cm in diameter and 32 cm in height cylindrical container full of EPS granulate) and then positioned between x-ray source and detector. Figures from 5.8 to 5.10 show the vertical and horizontal sections of the 3D images.

Slow freezing to -5 and $-7\,°C$ was applied by using a container full of 30 liters of antifreeze fluid as freezing chamber. In this latter case remoulded specimens by Method 4 were used. To apply slow freezing, the specimen is previously chilled from ambient temperature to 5 °C to avoid development of tensions at surface due to the large thermal gradient. Then, it is placed in the center of the chamber and the refrigerant fluid temperature is decreased by freezer (T=$-14\,°C$). To keep homogeneous the fluid temperature during the experiment, heat flow was produced in the following way. Five 1 liter bottles were introduced into the refrigerant liquid. Since they were

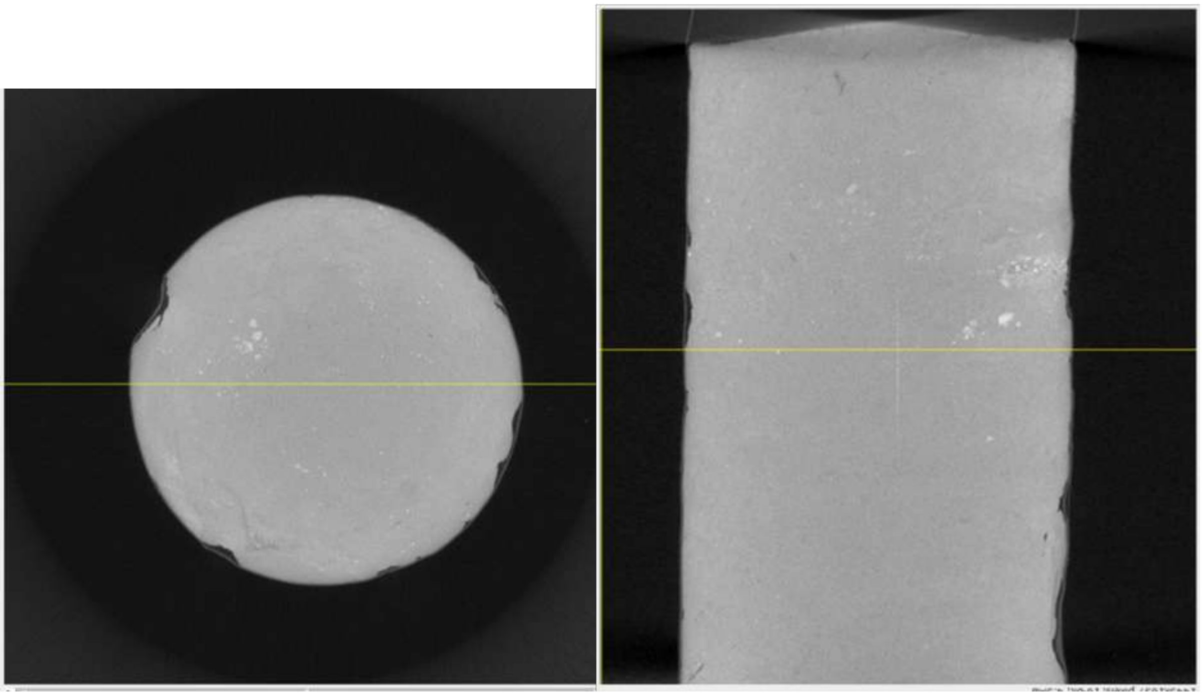

Figure 5.3: Halden silt specimen's horizontal and vertical section in frozen state for Freezing 1

filled of brine with different freezing point (-0.5, -1, -1.5, -2, −2.5 °C), once temperature reached the freezing point they start releasing energy to create its crystal lattice . Hence, heat convection involves in homogenize the refrigerant fluid temperature and help to make three dimensional the freezing process. Finally, sand was mixed to the brine, to avoid supercooling ("cool (a liquid) below its freezing point without producing solidification or crystallization [House (1993)]) and make the battles sink.

X-ray tomography scans were taken before and after freezing and at some intermediate freezing temperatures, in same cases. As for the severe freezing, the sample is placed in the isolation chamber, during the almost 40 minutes scanning.

Two experiments of slow freezing were carried out:

1. Two specimens were kept at 5 °C by refrigerator for 2 hours, then they were placed into the freezing chamber at 0 °C initial temperature and cooled finally down from 5 °C to −5 °C in 21 hours and 35 minutes. X-ray tomography scans were taken at a spacial resolution of 60 μm/voxel, before and after freezing. One of these two was also 20 min scanned when the liquid temperature was −2 °C and −3 °C after 3 hours and 45 minutes and 6 hours of

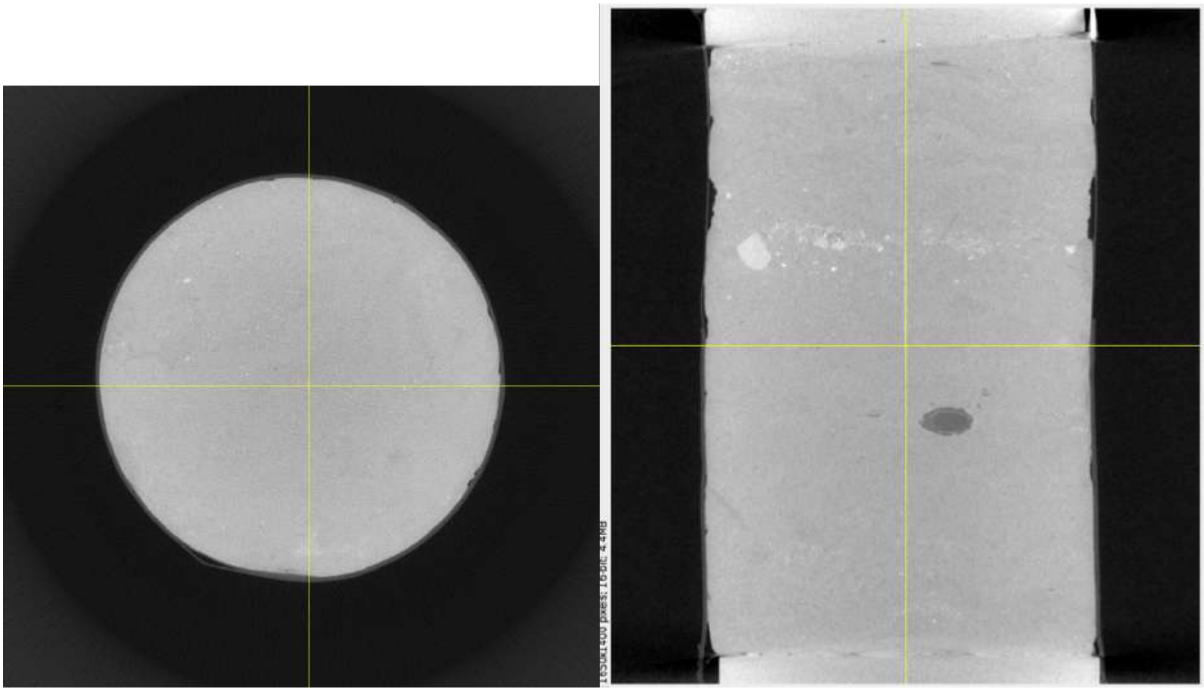

Figure 5.4: Halden silt specimen's horizontal and vertical section in unfrozen state for Freezing 2

cooling, respectively. During the scanning, the specimen was kept in the isolation chamber.

2. The specimen was first placed in 2 liters container filled with 5 °C antifreeze liquid for 1 hour and 10 minutes. Then, the whole system (sample plus container) was introduced into the freezing chamber at initial temperature of −4 °C. X-ray tomography scans were taken after 4 hours and 20 minutes, during which temperature was fluctuating between -4.0 and −4.8 °C. A further tomography was applied after 22 hours and 45 minutes, when antifreeze fluid was at −7 °C at the depth of the specimen, inside the freezing chamber.

5.4 Analysis

For Onsoy clay, the tomography scans (Figures 5.7-5.11) show freezing leads to soil segregation and ice crystals growth. In order to compare the different freezing procedures, an approximated measurement of the average of ice lenses thickness was realized by using the Software Fiji, built for the scientific image processing and analysis. By applying a threshold to the frozen clay 3D images, ice gets isolated from soil, and in this way simple is detect the amount of pixels

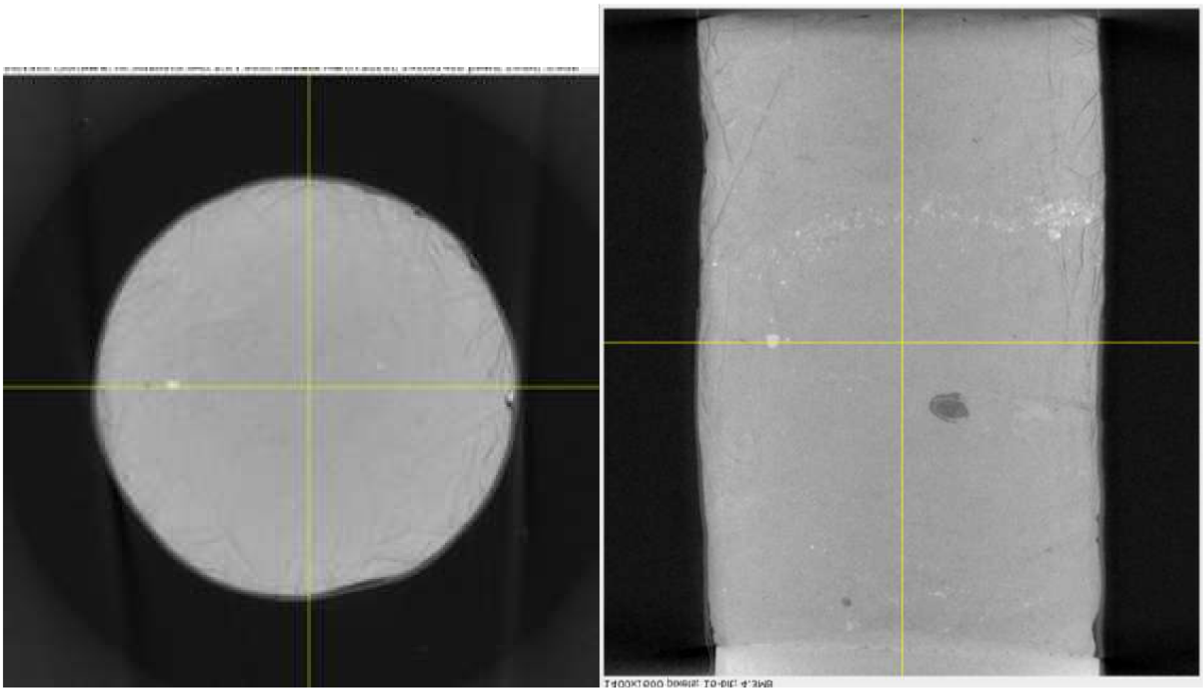

Figure 5.5: Halden silt specimen's horizontal and vertical section in frozen state for Freezing 2

contained in ice lenses by the stack histogram. By imposing the *skeletonization* of the stack, just the skeleton (1 pixel in thickness line) of the ice lens is left. The histogram of the skeletonized image gives us the numbers of black pixels contained in the new 3D image. The ratio between the amount of pixels involved before and after the skeletonization corresponds to the average of ice crystal thickness in pixel unit. The corespondent thickness in millimeters is obtained by multiplying the ratio to pixel size in millimeters.

Ice crystals develops with different inclinations and towards different directions during the freezing process. For this reason ice lensesare hard to isolate, identify and characterize. In the 3D images obtained for $-20\,°C$ fast freezing, ice lenses were more distinguishable since they were thicker, as we will see later. In such occasion, it was possible to observe that ice grows in the shape of planes, more or less extended, and its thickness could change depending of their position within the specimen.

For such reasons, by using the skeletonization method, one does not pretend to compute the ice planes thickness but just quantify an average of them. That is just to do the comparison among the methods analysed within this master project.

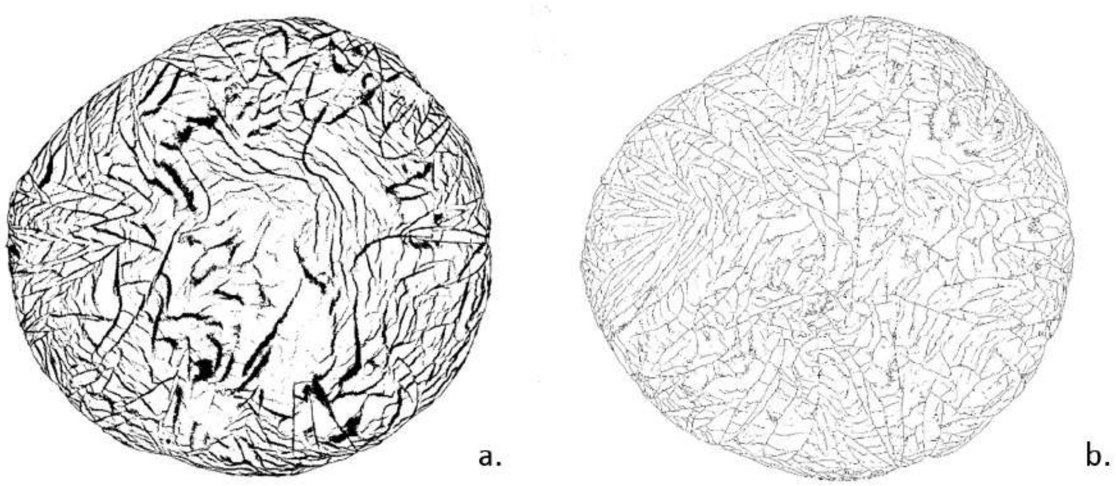

Figure 5.6: Binarized horizontal section of frozen clay: a. before skeletonization and b. after skeletonization

The results of the analysis are summarized in Tables 5.1, 5.2 and 5.3, together with the freezing temperature and and the water content. In Table 5.1, water content is the one measured before freezing, while in Tables 5.2 and 5.3, it was measured after thawing.

Table 5.1: Average ice lenses thickness for the fast freezing

T (°C)	w (%)	Thickness (mm)
-12	55	0.14
-20	55	0.26

5.5 Results

Despite of in some permafrost zones, frozen silt and clay present soil segregation and visible ice crystals, for the case in exam Halden silt did not reveal a strong tendency to segregate. Hence, it can be concluded that a reliable mechanical response of an Halden silt frozen specimen could be obtained by using almost any freezing procedure.

Ice crystals develop through Onsoy clay when the temperature drops below $-4\,°C$ and that makes the specimen non-homogeneous and an-isotropic. In particular, from the image processing of the 3D tomography scans, different parameters affecting the ice lenses average thickness were identified. Table 5.1 show that low freezing temperature leads to thicker ice planes. The reason

Table 5.2: Average ice lenses thickness for the slow freezing, Experiment 1

T (°C)	**w (%)**	**Thickness (mm)**
-5	61	0.22
-5	49.6	0.08

Table 5.3: Average ice lenses thickness for the slow freezing, Experiment 2

T (°C)	**w (%)**	**Thickness (mm)**
-4	48.4	0.16
-7	48.4	0.19

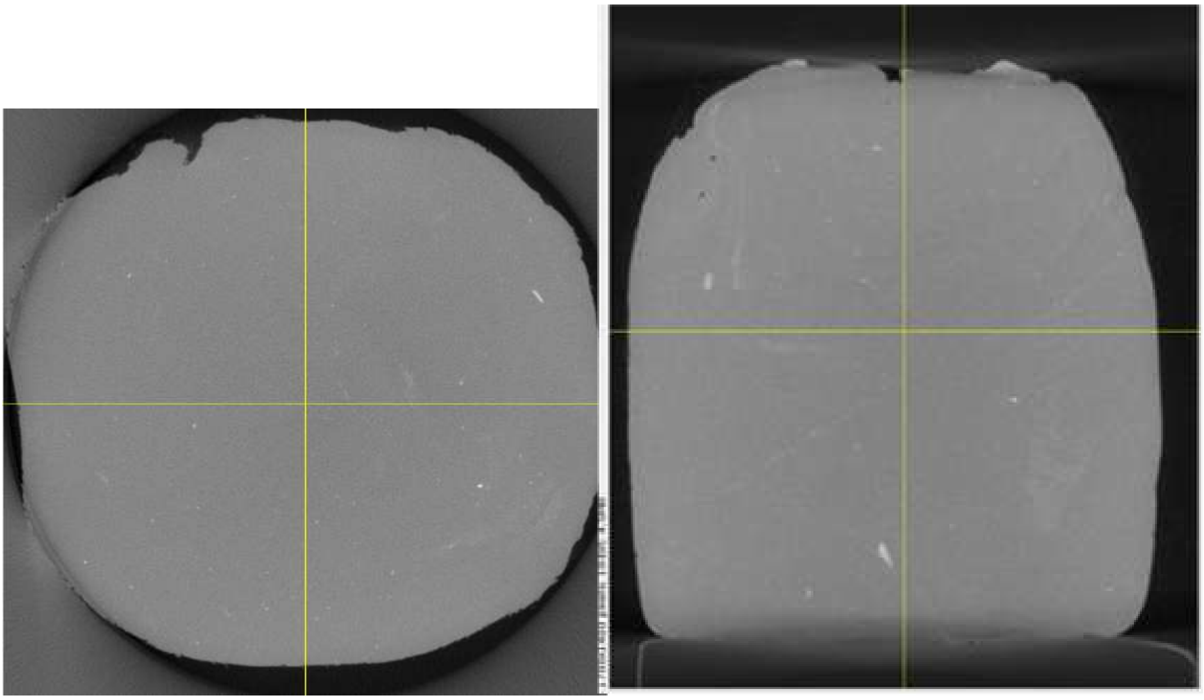

Figure 5.7: Onsoy clay specimen's horizontal and vertical section in unfrozen (left) and frozen (right) state, $-12\,°C$ fast freezing

could be that due to a larger thermal gradient, a greater suction pressure develops towards the core of the sample. That makes clay segregate and consolidate while water supply ice lenses, making them longer and thicker. Some authors use Clapeyron equation to model this pressure (*e.g.*, O'Neill and Miller (1985), Thomas et al. (2009)). Table 5.2 allows to notice that in the case of less water content the ice lenses are thicker than in the other case. Again in Table 5.3 an increase in thickness can be seen when the temperature descreases.

As regards the slow freezing procedures, the two experiments were realized at a different

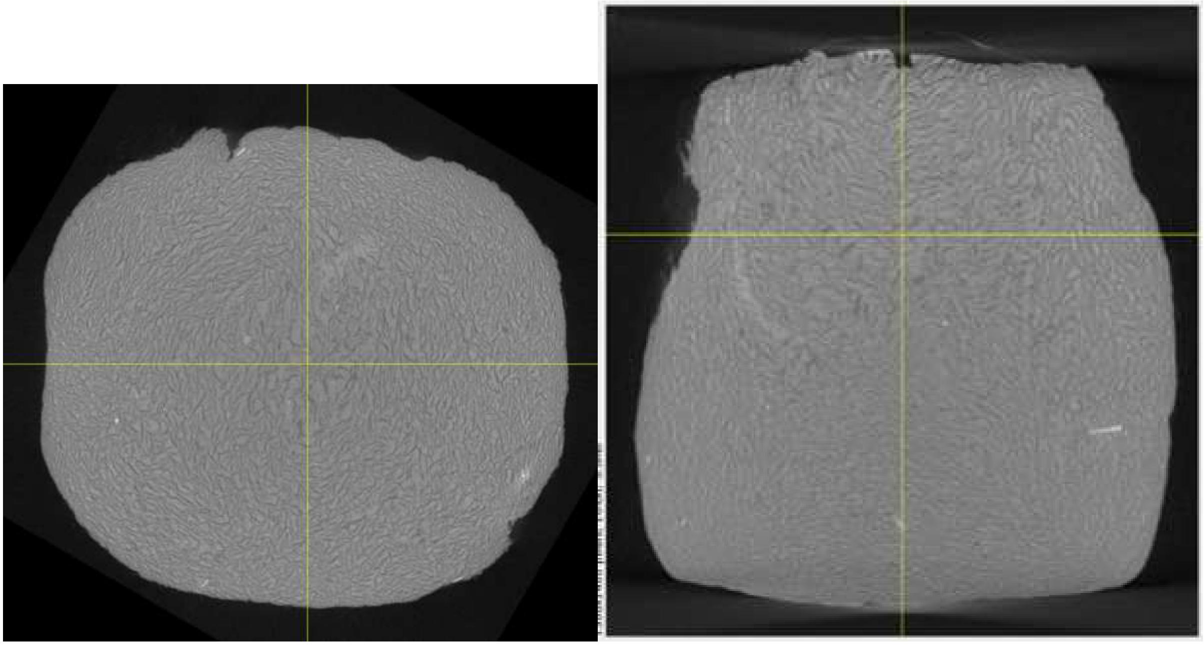

Figure 5.8: Onsoy clay specimen's horizontal and vertical section in unfrozen (left) and frozen (right) state, −12 °C fast freezing

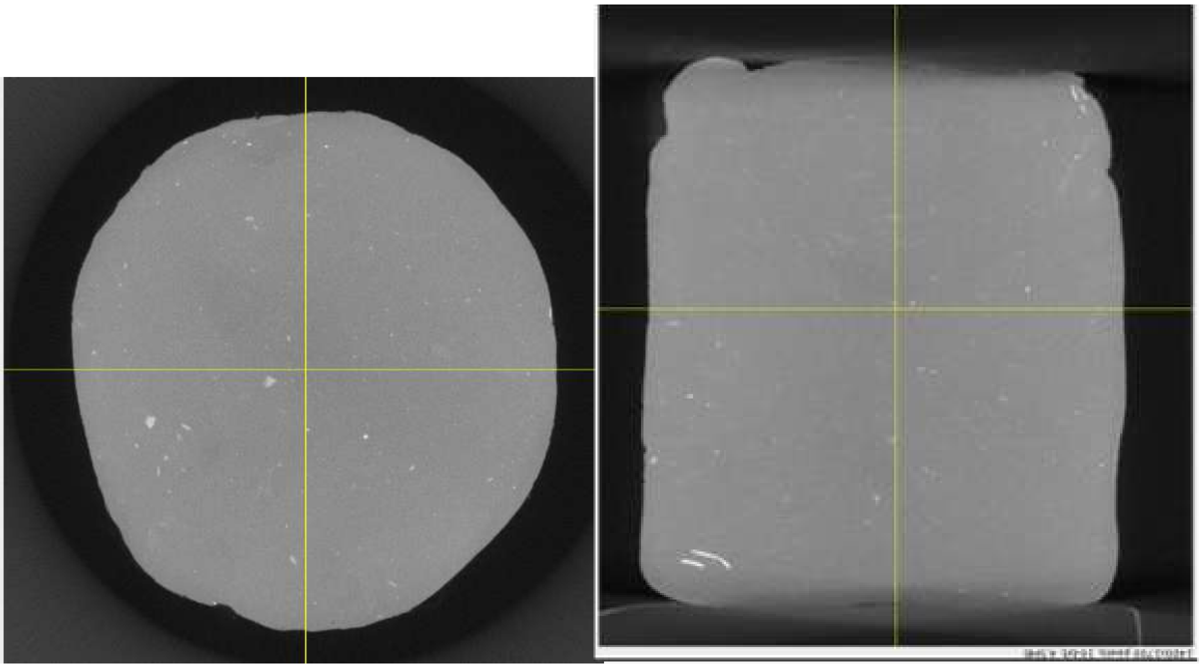

Figure 5.9: Onsoy clay specimen's horizontal and vertical section in unfrozen state, −20 °C fast freezing

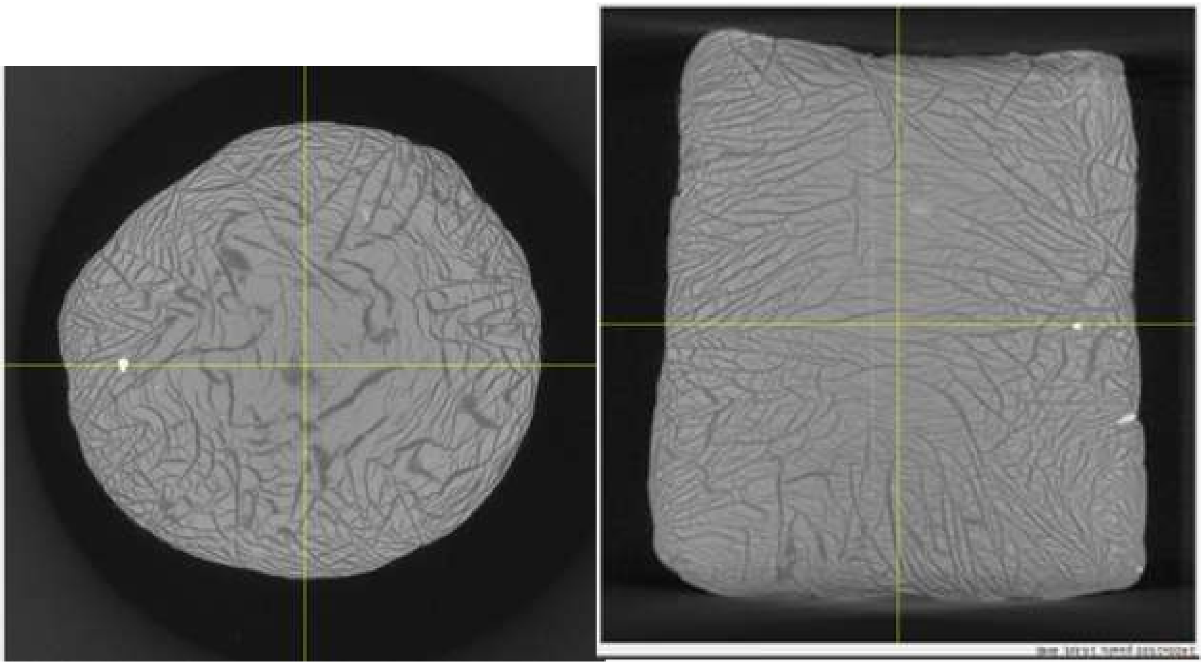

Figure 5.10: Onsoy clay specimen's horizontal and vertical section in frozen state, $-20\,°C$ fast freezing

freezing rate. It appears evident that, for specimens almost equal in water content, despite of the higher temperature, the second experiment at a freezing temperature of $-4\,°C$ make ice lenses thicker than in the first experiment carried out at a freezing temperature of $-5\,°C$. Hence, the rate of freezing needs to be take into account to make the frozen specimen homogeneous, as well as thermal gradient and water content.

Among the freezing methods tested during this master thesis, the slow freezing from 0 to $-5\,°C$ was identified as the best procedure to freeze, since it involves the most homogeneous soil material, despite the existence of small ice crystals.

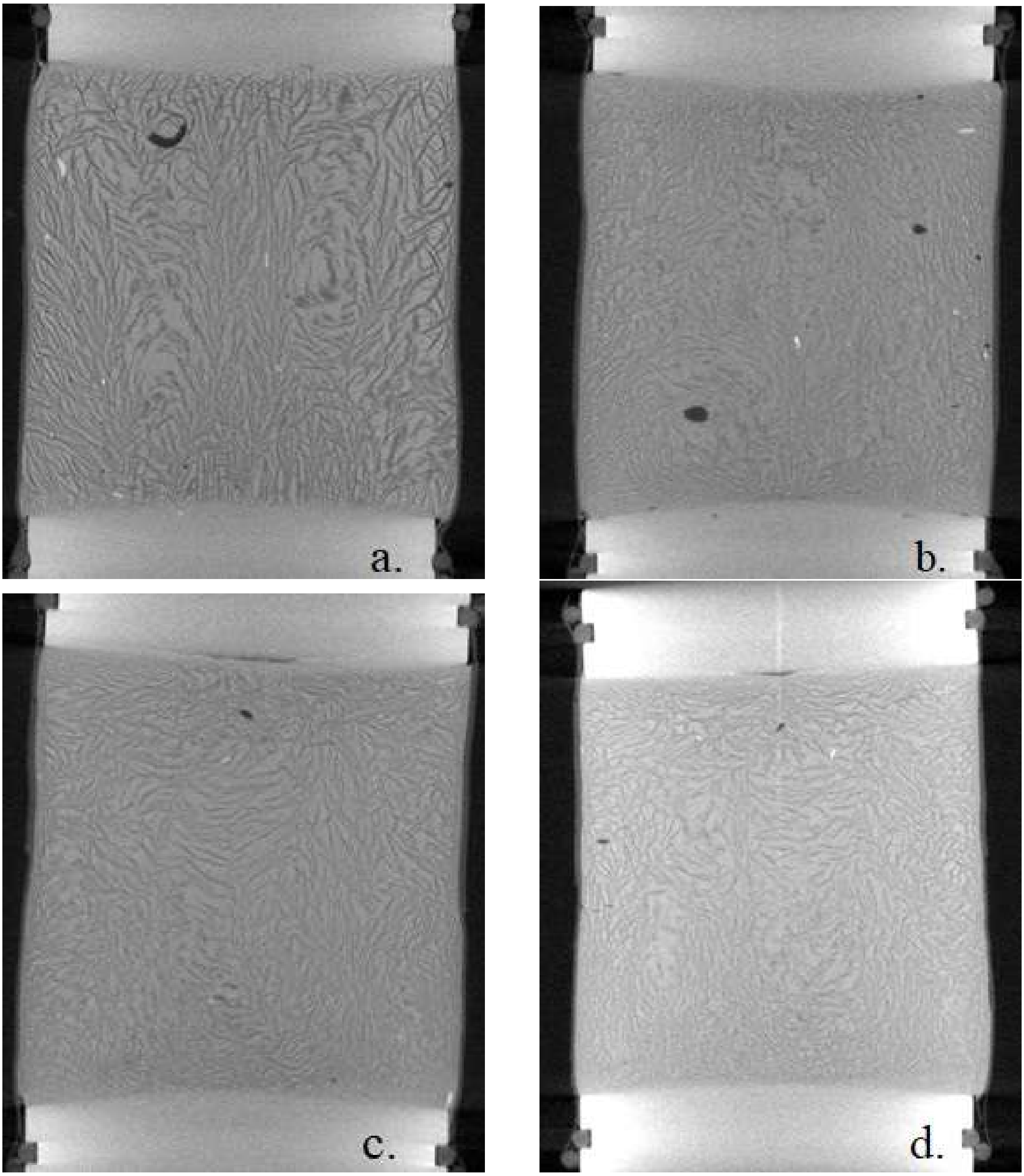

Figure 5.11: Onsoy clay specimen's vertical section for slow freezing (a: experiment 1 (w=61%), b: experiment 1 (w=49.6%), c: experiment 2 (−5 °C), d: experiment 2 (T=−7 °C)

Chapter 6

One-dimentional freezing

Soils may contain dissolved salt in their pore water, due to the mineral composition of rocks from which they were originated or to their position relative to salt water source. Indeed, soils are in may cases sedimented in seawater. For instance, that is the case of marine clays in Scandinavia and Canada currently above sea level due to the land heave after the last ice-age Salt affects the soil physical, mechanical and thermal properties. It increases the freezing-point depression, increases the unfrozen water content and results in a reduced frost susceptibility [Andersland and Ladanyi (2004)]. For these reasons, freezing usually occurs in soils when temperature drops some degrees below 0 °C. In such occasion, heat is extracted from soils and a thermal flux develops from the higher to the lower temperature. Despite of a three-dimensional freezing is applied on the specimen, if the phenomena is seen at a smaller scale, the freezing process occurs due to a one dimensional thermal gradient. Furthermore, the natural freezing process is one-dimensional in natural seasonally and perennially soils and sometimes also in artificial frozen ground. Then, in order to understand how the freezing process involves in porous media, one-dimensional freezing was applied in Onsoy clay and Halden silt specimen.

6.1 Freezing chambers

The studying of one-dimensional freezing needed two experimental campaigns. In order to scan the freezing process in soils, a small freezing chamber was designed to fit inside the tomograph.

The freezing chamber planned for the first campaign was successively improved during the second set of experiments. Such chambers were designed to freeze the specimen by the contact with frozen brine, *i.e.*, a mixture of salt and water. The contact with a mass at a temperature less than that of the specimen develops a heat flow towards the frost source. When the specimen temperature drops some degrees below zero, it starts to freeze. Once the temperature reaches the brine's melting point, the mixture start to melt. The phase changing occurs at a constant temperature, as Figure 6.1 shows. During the plateau, the brine's crystal lattice is disrupt by breaking the hydrogen bonds and just when the brine is completely, the temperature begin to raise [Zumdahl and Zumdahl (2011)]. The plan was to unidimensionally freeze the specimen from the bottom to the top, during the brine's melting period.

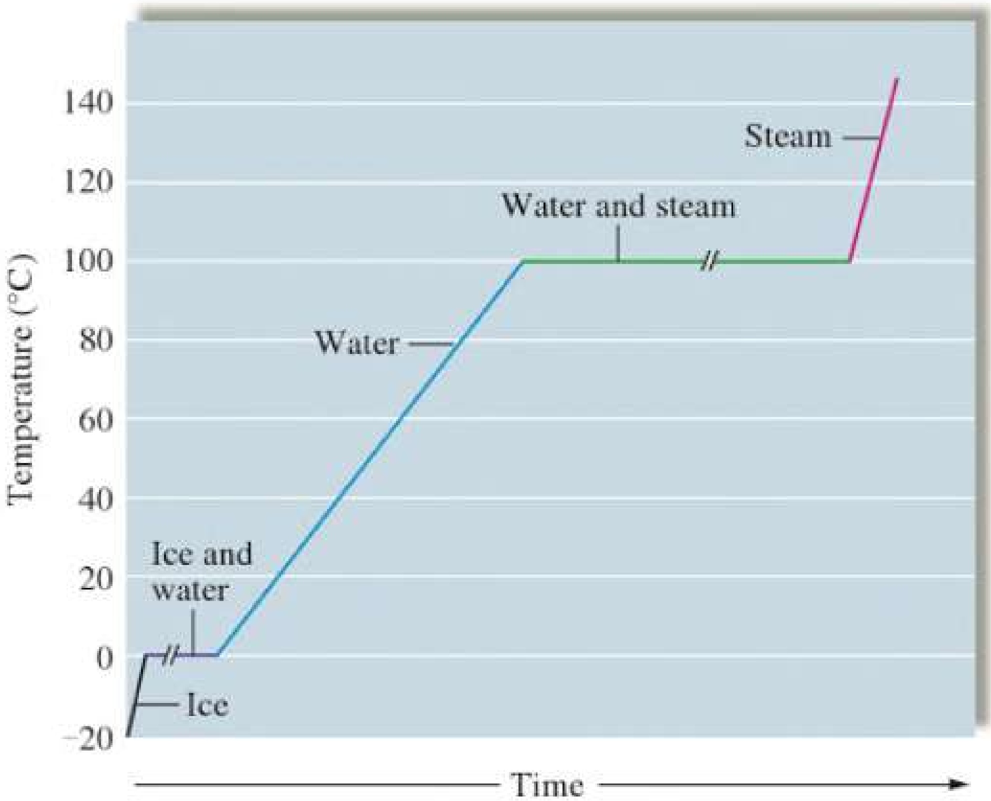

Figure 6.1: Water heating curve from Zumdahl and Zumdahl (2011)

The designed freezing chambers are described in what follow.

1. For the first campaign the freezing chamber (Figure 6.3) was constituted by one cylindrical

container (125 mm in diameter and 130 mm in height) filled by1 L frozen brine for the clay and 2 L frozen brine for the silt with $-12°$ as melting point. The container was isolated by almost 4.5 L of Expanded Polystyrene Granulate (EPS) granules, placed in a bigger cylindrical container (160 mm in diameter and 325 mm in height). The camber's vertical section is shown in Figure 6.3. The specimen was inside latex membrane and between metal caps. The bottom metal cap was placed straight on ice, to obtain a good contact to the freezing source. Due to the ice melting, the tomography scans show the specimen moved downwards during the freezing. Such problems was fixed in the second chamber.

2. During the second campaign, the amount of brine was increased to 3 L to record a longer freezing process. The container for brine was 180 mm in diameter and 200 mm in height. In such container, an hollow pedestal was introduces and a metal plate was placed on it. The plate was 10 mm in thickness. The specimen was placed on the metal plate, in order to avoid the movement of the specimen during the 3D scans. The brine container was inside a bigger bucket (310 mm in diameter and 330 mm in height) filled by EPS granules. The EPS layer on the top of the specimen was almost 50 mm, smaller than the one at the lateral surfaces to ensure a one-dimensional freezing. Thermocouples were placed to know the temperature in the system during the freezing. The freezing chamber's vertical sections are shown in Figures 6.2 and 6.3.

6.2 Comparison between Halden silt and Onsoy clay

During the first experimental campaign, Halden silt and Onsoy clay were one-dimensional frozen imposing at the specimen's bottom a temperature of $-12\,°C$. Onsoy clay was frozen and scanned for 210 min, while Halden silt for 162 min. Figures from 6.4 to 6.9 show the vertical section of the specimens scanned at a spacial resolution of $120\,\mu m$ for three subsequent instants. The gray value in the scans is an average of the x-ray attenuation occurred for 5 min.

In Halden silt, the scans show that the one-dimensional freezing involves in a frost front which moves upwards. It can be identified since above it the material keep the same gray tone, while below the frozen soil appears darker, because of its density is decreased. No ice lenses develop during the freezing process.

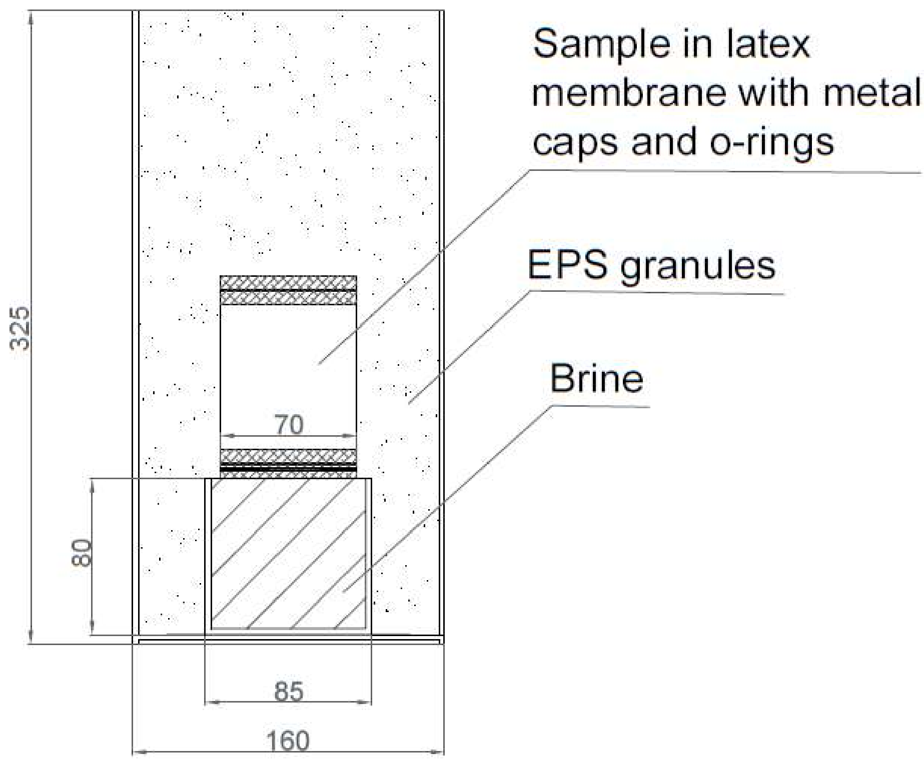

Figure 6.2: Freezing chamber adopted for the first experimental campaign

On the other hand, in the Onsoy clay specimen, a net frost front is not distinguishable but ice lenses appear growing upwards. In order to investigate what the freezing process involved in the Onsoy clay, two analysis were realized. First the change in density over the time along the vertical section of the specimen was computed. Then, some questions born in this analysis were answered by the computation of deformations occurred during the freezing.

6.3 Registration of images

As described in the previous sections, the Onsoy clay scans showed a moving sample. Such problem made very hard the image processing and then difficult the freezing process study. In order to get the bottom cap in the same position for each image, the *registration* of the 3D images was realized. Using the functions of SPAM, a code was implemented. First, the Transformation Gradient Tensor Φ was computed between one image and the one taken at the instant zero. The

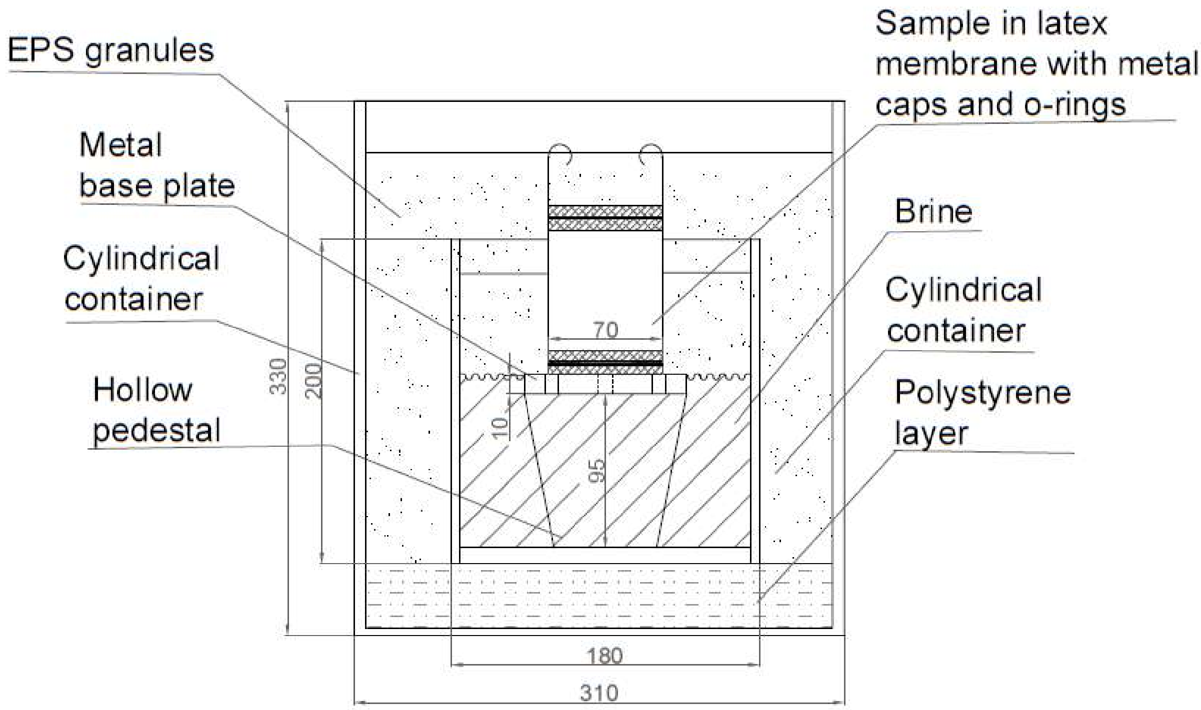

Figure 6.3: Freezing chamber adopted for the second experimental campaign

4x4 Φ is "deformation function" which contains the familiar 3x3 F in the top-left, known as "displacement gradient" $\frac{du}{dx}$. The Φ matrix provides the 3D transformation between the deformed image and the reference one. Its terms correspond to the average of elongations computed along three orthogonal axis and of distortions. Furthermore, it can be decomposed with a *polar decomposition* into translations, a rotation matrix and a stretch tensor. The first two are rigid motions.

$$\Phi = \begin{bmatrix} F_{zz} & F_{zy} & F_{zx} & t_z \\ F_{zy} & F_{yy} & F_{yx} & t_y \\ F_{xz} & F_{xy} & F_{xx} & t_x \\ 0 & 0 & 0 & 1 \end{bmatrix}$$

Φ matrix is computed by the function *lucasKanade*, it starts an iterative process in with the gray values of pixels within the reference and the deformed images are compared until the best matching is found, then the transformation parameters are returned. After the correlation, rigid translation and rotation vectors were extracted from the Φ matrix. Once they were inverted, a new Φ matrix, containing just these values, was computed and then applied to the image.

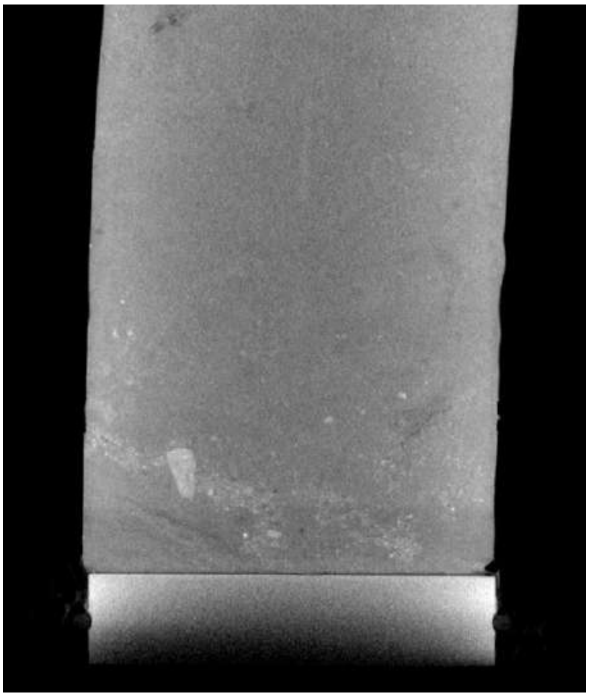

Figure 6.4: Halden silt vertical section after 0 min

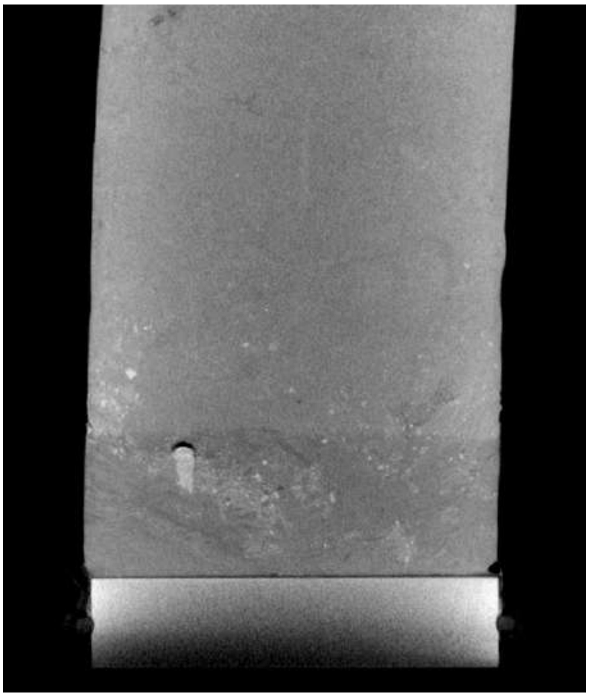

Figure 6.5: Halden silt vertical section after 84 min

6.4 Change in density over the time along the Onsoy clay specimen

The analysis of the change in density was realized by the use of the software Fiji. The soil's change in density during the freezing process was measured at six different heights as shown in Figure 6.10, where 800 pixels (96 mm) is the total height of the image. The change in density is expressed in terms of gray values. Higher gray values express a greater density, since they are generated by a major x-ray attenuation. Using the software ImageJ (Fiji), once registered, the images were *concatenated* and just a square (300x300 pix^2 in size, *i.e.*, 36x36 mm^2, centered in the image center) was extracted from the 4D image (Figure 6.11), in order to avoid boundary noise. Once the horizontal section is chosen, the trend of the mean of its grey values is plotted over time (Figures from 6.12 to 6.17).

Since 16 bit images were handled, grey values range is 0-65536.

Elevation h=150 pixels (18 mm) is in the darker zone, here density decreases until it becomes constant after 132 min. At elevation h= 250 pixels (30 mm), a peak is visible. It represents the

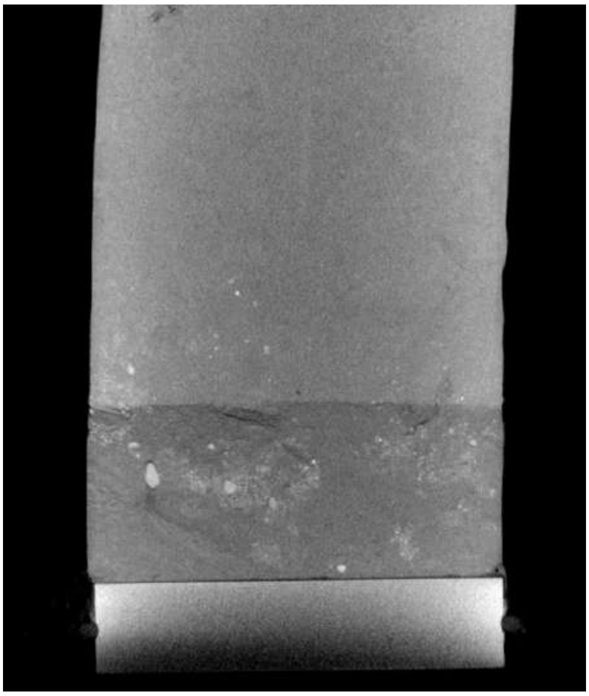

Figure 6.6: Halden silt vertical section after 162 min

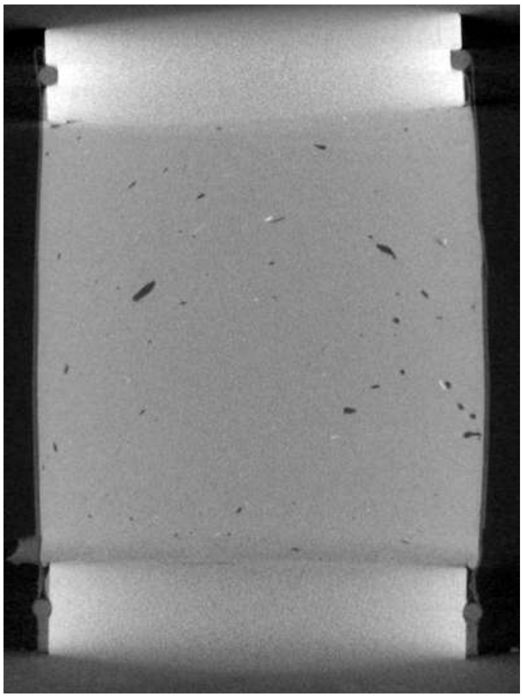

Figure 6.7: Onsoy clay vertical section after 0 min

higher density ahead the ice lenses, due to the suction pressure. A densification can be seen also at h= 350 pixels (42 mm) at the end of the scanned freezing process. In the upper zone, density keeps quite constant until depth h=650 pixels (78 mm), where a decreasing in density is recorded. Two first explanations may be:

1. it is an x-ray reconstruction artefact due to the density contrast between sample and cap;
2. such gray values belong to the metal cap at the first scans and at the soil at the end.

This latter hypothesis implies a vertical elongation of the specimen during the freezing process.

In this way four different zones were identified along the height of the specimen. From the bottom to the top, they are:

1. dark zone: this zone develops in a second time. Two hypothesis could be done to explain the reason of this darker gray value
   (a) due to the heat extraction, just in a second time the specimen's bottom zone soil reaches the temperature of −12 °C. In such condition, this darker gray value could

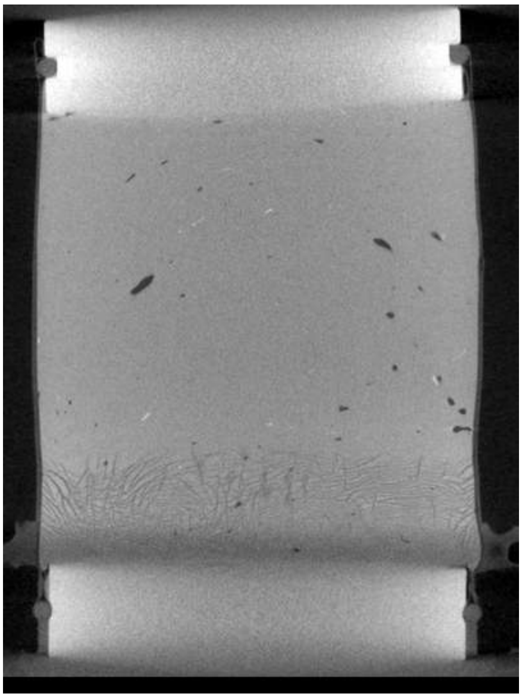

Figure 6.8: Onsoy vertical section after 120 min

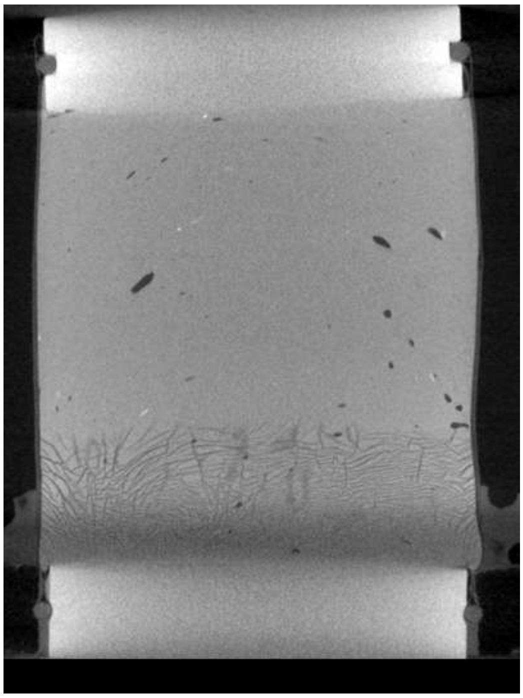

Figure 6.9: Onsoy vertical section after 204 min

be an average of further small ice crystals (not well visible at a spacial resolution of 60 μm);

(b) since the frozen brine is melting, the specimen drops into the water. The presence of this latter around the specimen could contribute to the x-ray attenuation;

2. ice lenses zone: within this zone ice lenses develop upwards, driven by the thermal gradient;

3. suction zone: the soil appears denser because, ahead the ice lenses, suction pressure develops due to the thermal gradient;

4. the soil appears undisturbed by the freezing.

A further analysis of the change in density was concluded by the computation of the gray values mean along the whole height of the sample over the time. In this case images were not concatenated. For each 3D image, a parallelepiped with square cross section (300x300 pix^2 in size, centered in the image center) was extracted. The gray values mean was automatically calculated for each square cross section by the software and plotted against the section position (slice) along the specimen height. Differently from the previous analysis, in which different sections were considered, now the entire specimen height was taken into account. Figures 7.10 and 6.19 show the mean of grey values computed in the horizontal slices of the sample, at the first and the last time step. In the horizontal axis, there are the number of slice from 0, the first section at the bottom to 800, the last at the top. The distance between each slice is 140 μm. The first and the last big peak represent the attenuation of the aluminum caps and, between these two, the gray value belongs to the sample. By doing the comparison between the graphs at these two different time steps, it is possible to notice that the gray value of the relative minimum, representative of the darker zone, decreases during the time, confirming what seen in the previous analysis (Figure 6.16). Ahead the relative minimum, a small peak is identifiable. Such peak can be considered representative of the suction zone. By the comparison between the two graphs, it is interesting to notice that the peak moves upwards but keeping the same value during the freezing process (Figure 6.20). That suggests that, in the graphs in Figure 6.14 for h = 350 pixels (42 mm) the density increases due to the suction zone is moved at that section, at the end of the freezing process.

At first glance, one may say that such results indicate that the suction pressure is constant during the process. Then, since the temperature below the specimen was constant, the thermal gradient and the suction pressure follow a linear law, as in the Clapeyron equation (2.1). Looking more accurately, the slopes of the curve ahead the peak changes (Figure 6.21, indicating that the zone interested by suction gets longer over the time, calling into question the linearity of temperature and suction. Furthermore, a plateau develops between the relative minimum and maximum. It represents the average of frozen soil and ice crystals gray value and it keeps constant during the freezing process .

6.5 Deformations during the freezing process

Deformations of the Onsoy clay specimen during the one-dimensional freezing process was computed running the function *lucasKanade* of SPAM. The function returns the 3D transformation from the reference image (usually the one at the instant zero) to the new image, expressed by the Φ matrix. The code was implemented on the registered images. Since during the 1D freezing

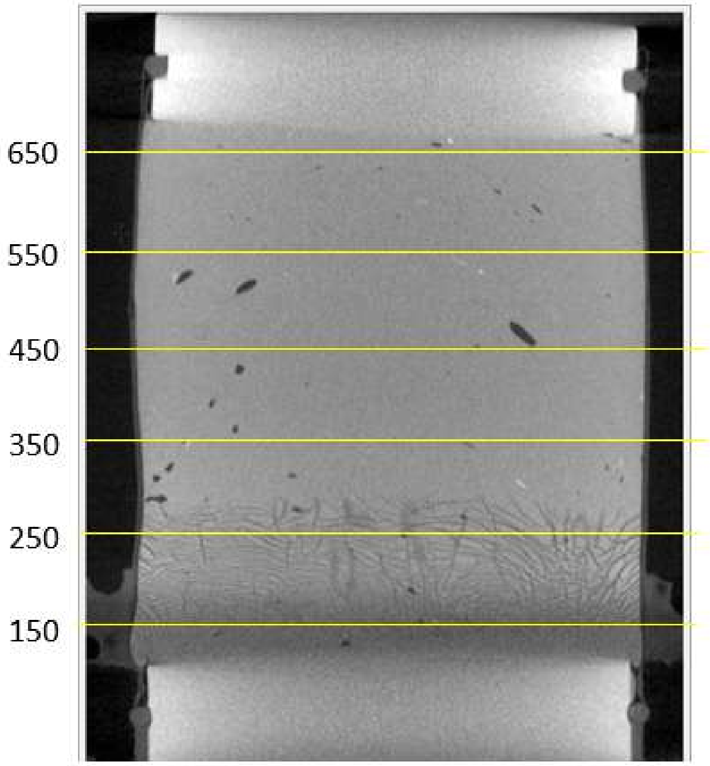

Figure 6.10: Slice elevation (in pixels) for which change in density was computed

four different zones were identified (see Section 6.4). The transformation was computed in such zones by isolating them during the matching operated by *lucasKanade*. The limits between zones 1 and 2 and between zones 2 and 3, as well as between soil and metal caps, where recognized with a precision of 5 slices (less than 1 mm), since the material changes its appearance. Between zone 3 and 4, no precise limit was identifiable. Furthermore, to make the iterations converge, the length of the zones was increased. In particular, metal caps where added to zone 1 and zone 3 (Figure 6.21), since their contraction due to the thermal gradient is negligible respect to the soil strain. Figure 6.22 shows the axial elongation, the change in volume ΔV and the rigid vertical displacement computed for each zone. The axial elongation was computed by subtracting 1 from F_{zz}. Under the hypothesis of large displacements, the change in volume ΔV was calculated as the determinant of the 3x3 matrix extracted from the Φ matrix by removing the last row and column. Such 3x3 matrix is known in literature as the Transformation Gradient Tensor F. The rigid vertical displacement was straightly returned by the Φ matrix. The explanation of graphs is

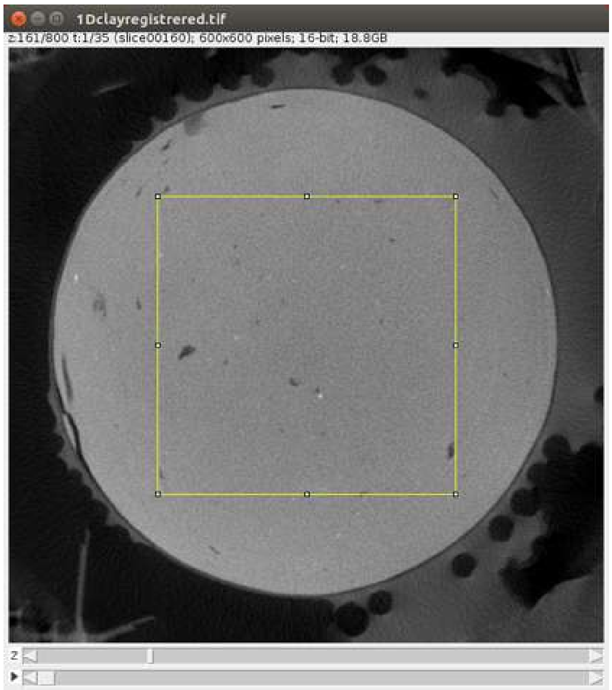

Figure 6.11: Square extracted portion from 4D registered image

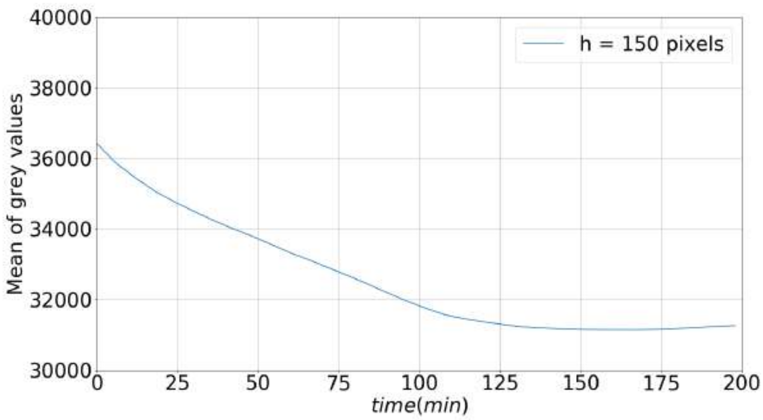

Figure 6.12: Mean of grey values over the time at elevation 150 pixel

realized for each zone in what follows.

1. In zone 1, a positive axial elongation is recorded until the minute 150, after which it unexpectedly becomes negative. The same trend and almost the same values are shown by the change in volume. Then, the change in cross section size is expected to be negligible, as

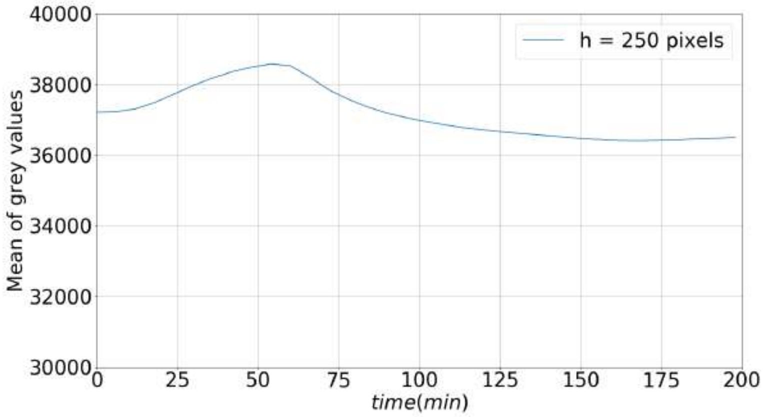

Figure 6.13: Mean of grey values over the time at elevation 250 pixel

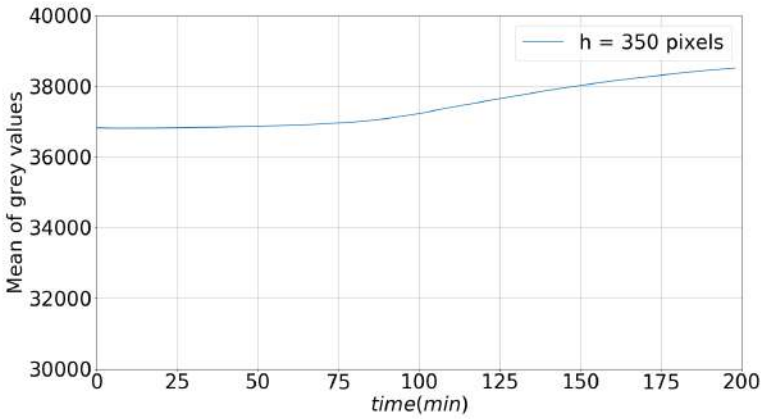

Figure 6.14: Mean of grey values over the time at elevation 350 pixel

graphs confirm in Figure 6.23. Small vertical displacements were recorded. In particular a maximum downwards displacement of 0.24 mm is recorded, confirming that the images were well registered. No reasonable physical explanation are given for the contraction at the end of the freezing.

2. Contrary to the zone below, in zone 2, a vertical contraction is recorded at the beginning of the freezing process followed by a vertical expansion. Here, contraction could be due to the effect of suction pressure while the zone starts to elongate when it is reached by ice lenses. The same behavior is shown by the change in volume but with larger percentage at the contraction time and lower percentage at the expansion time. Such observations

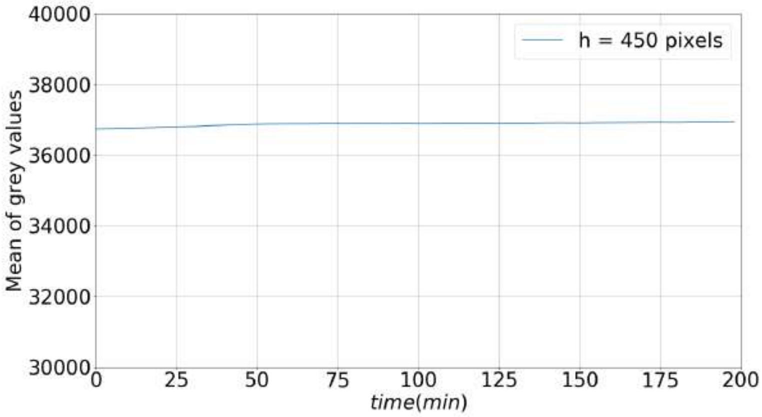

Figure 6.15: Mean of grey values over the time at elevation 450 pixel

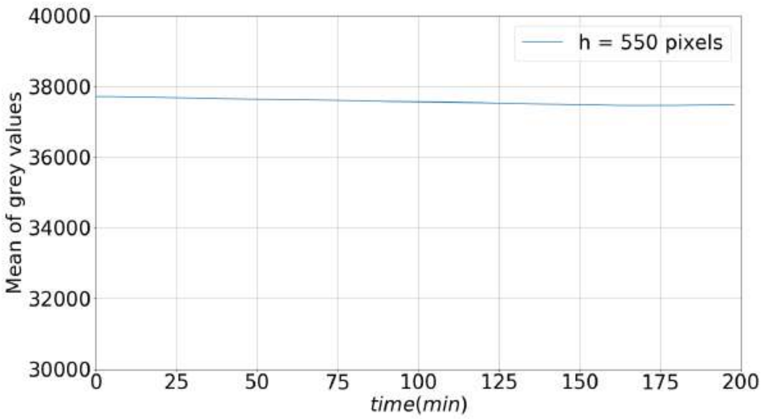

Figure 6.16: Mean of grey values over the time at elevation 550 pixel

tell that horizontal strain is negative over the time. The maximum recorded expansion in volume is almost 8%. At the end of the freezing, the entire zone is subjected to a vertical upwards displacement of 11 pixels. Since the images were preventive registered, movement at the basis of the sample was removed. Then, rigid displacement could only derive from the integration of the axial elongation measured in the zones below, but actually it is not. Furthermore, vertical displacement occur in the first 150 min of freezing, after that it keeps constant.

3. Within the Zone 3, strains along the three axes and change in volume are negligible, while the rigid vertical displacement is almost 10 pixels at the end of the freezing.

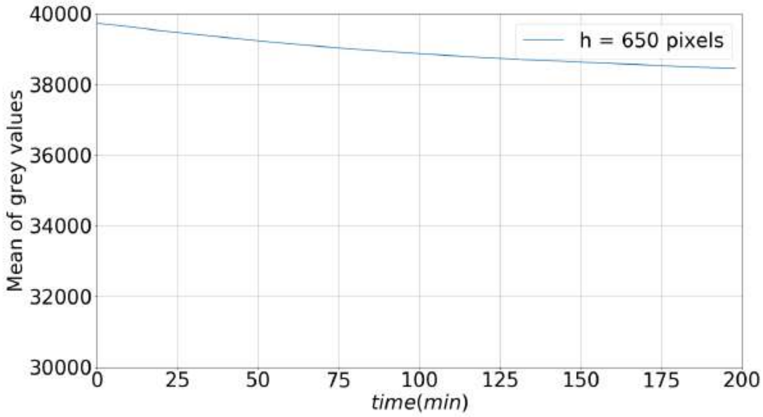

Figure 6.17: Mean of grey values over the time at elevation 650 pixels

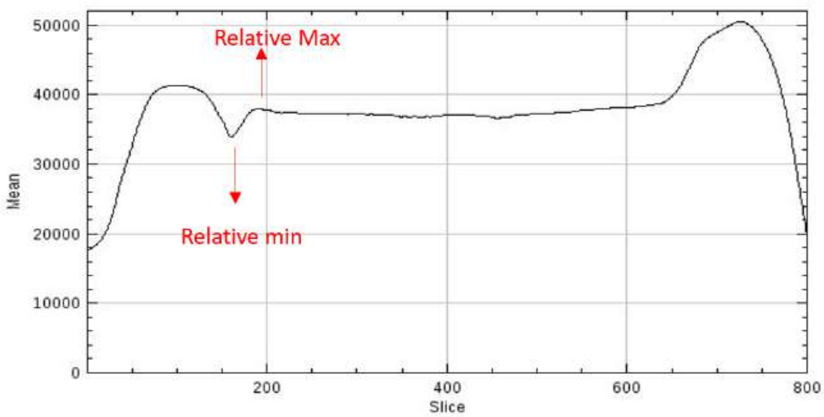

Figure 6.18: Mean of grey values along the specimen at the first x-ray scan

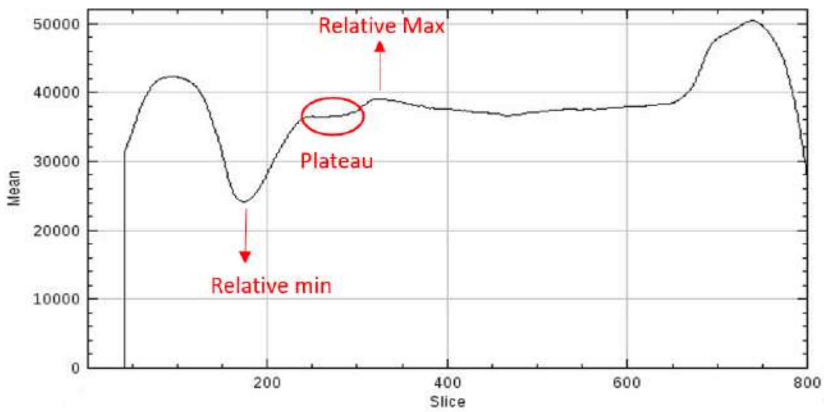

Figure 6.19: Mean of grey values along the specimen at the last x-ray scan

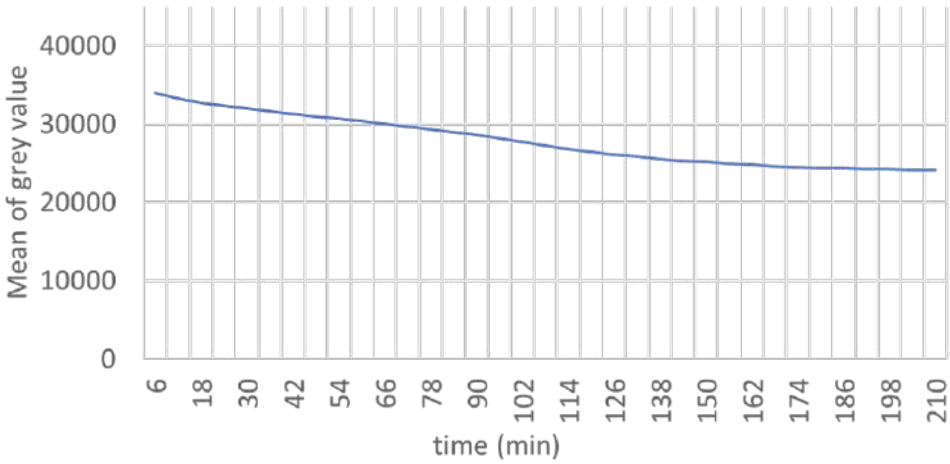

Figure 6.20: Gray value of the relative maximum over the time

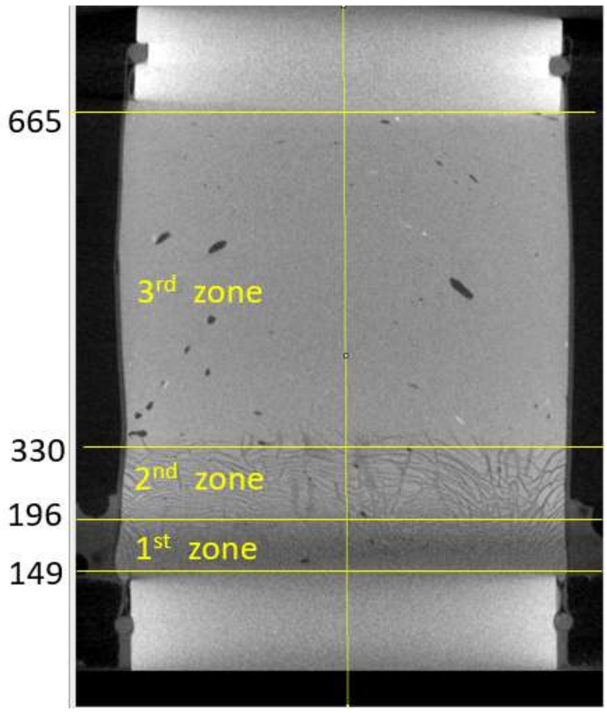

Figure 6.21: Different zones identified along the specimen

6.6 Validation of deformation analysis

As seen in the previous sections, the freezing process involves the change in density of the material and the growing of new elements into the soil, *i.e.*, the ice lenses. Such factors make

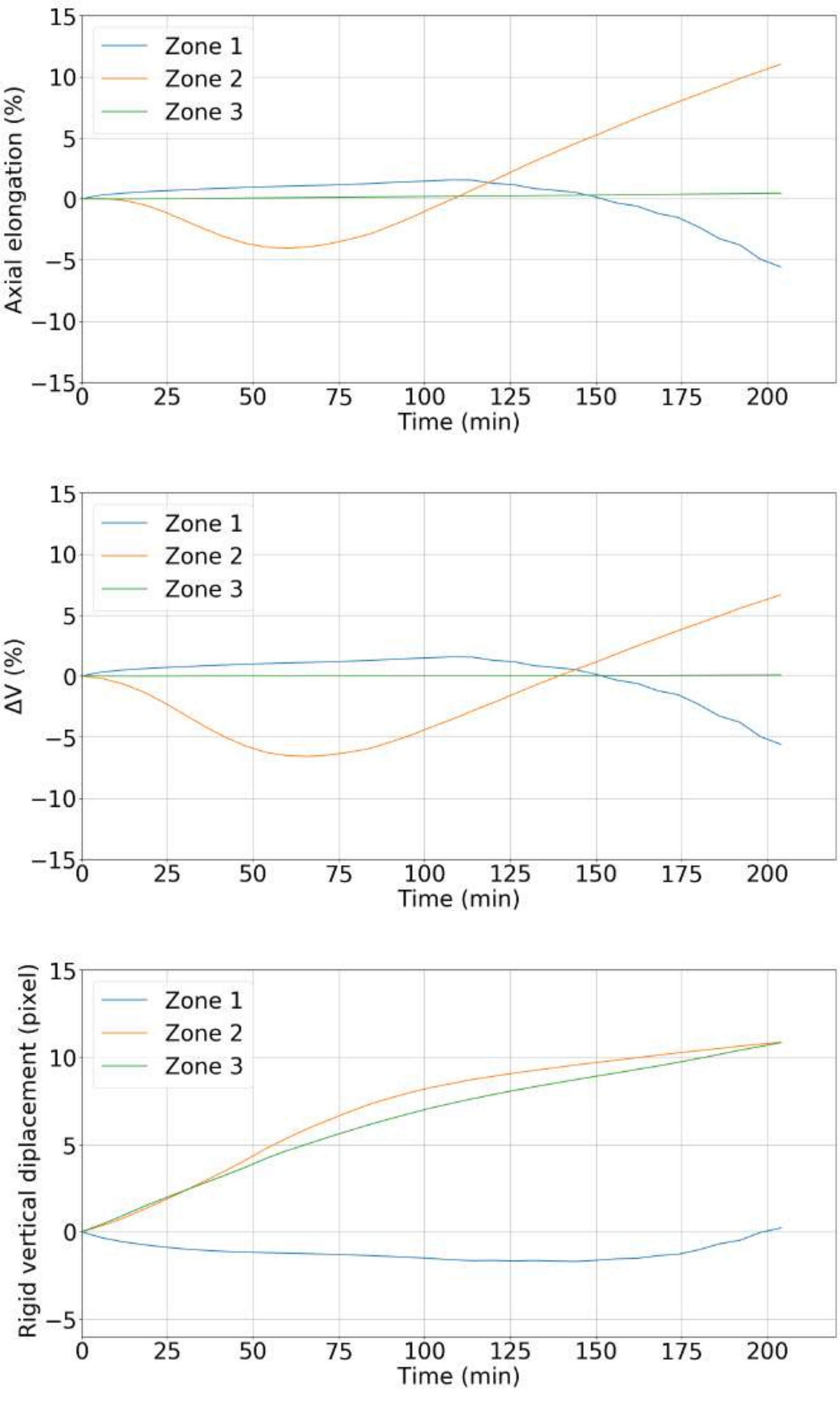

Figure 6.22: Axial elongation, change in volume and rigid vertical displacement over the time within Zone 1, 2 and 3

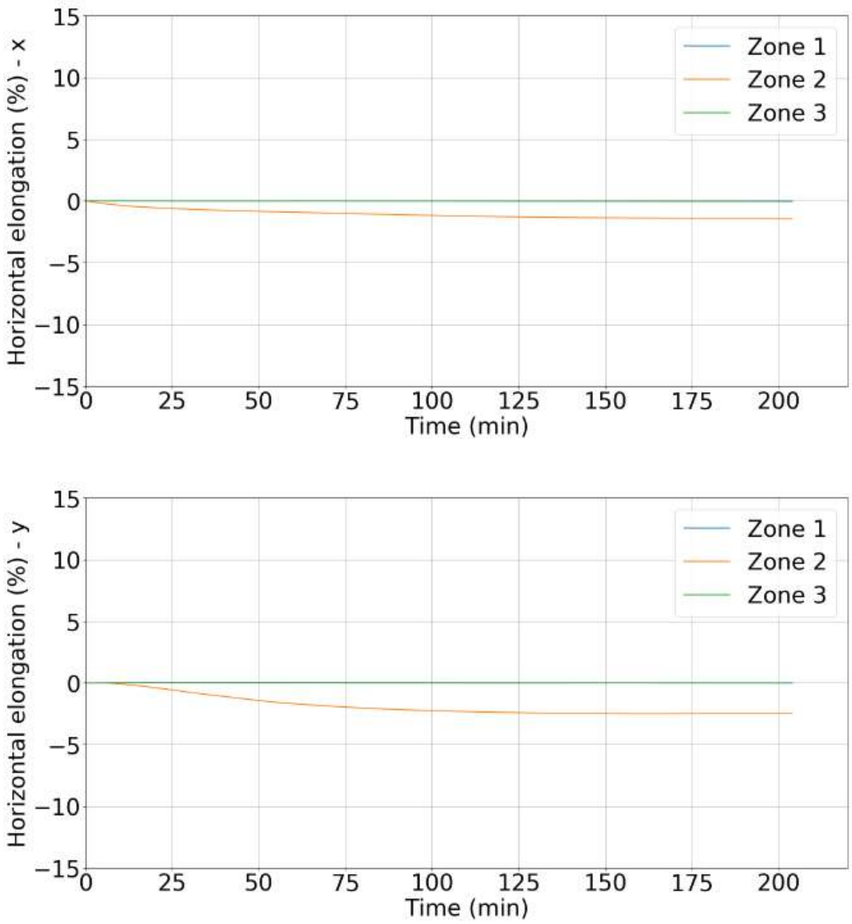

Figure 6.23: Horizontal strains over the time within Zone 1, 2 and 3

the correlation process difficult since the matching is searched between pixels whose gray value changes. A validation protocol was thought to prove the results were reliable. The objective was to test if the same vertical elongation is obtained, by calculating it in two different ways:

1. Manually: the 3D images taken at the beginning and the end of the freezing process were considered. The same cross sections were identified at the bottom and the top of the specimen in the two 3D images (Figures 6.24 and 6.25). The difference of the distance between the two cross sections at the beginning and at the end of the freezing process, gives the vertical elongation, once it is multiplied by the pixel size. Such elongation was found equal to 1.96 mm.

2. Axial strain: the component F_{zz} was extracted for each zone at the freezing end instant. By

multiplying such term by the initial height of the relative zone, its final height is computed. The subtraction between final and initial eight returns the vertical elongation.

(a) first zone: δ = (1- F_{zz}) · h = (1 - 0.94) · ((196-163) · 0.14) = -0.28 mm

(b) second zone: δ = (1- F_{zz}) · h = (1 - 1.12) · ((330-196) · 0.14) = 2.25 mm

(c) third zone: δ = (1- F_{zz}) · h = (1 - 0.00) · ((661-330) · 0.14) = 0.00 mm

The sum of the vertical elongation occurred in the three zones returns a total elongation of about 1.97 mm.

Elongations obtained in these two ways differ of 0.01 mm, which is enough small to say that correlation works well, despite of the freezing process.

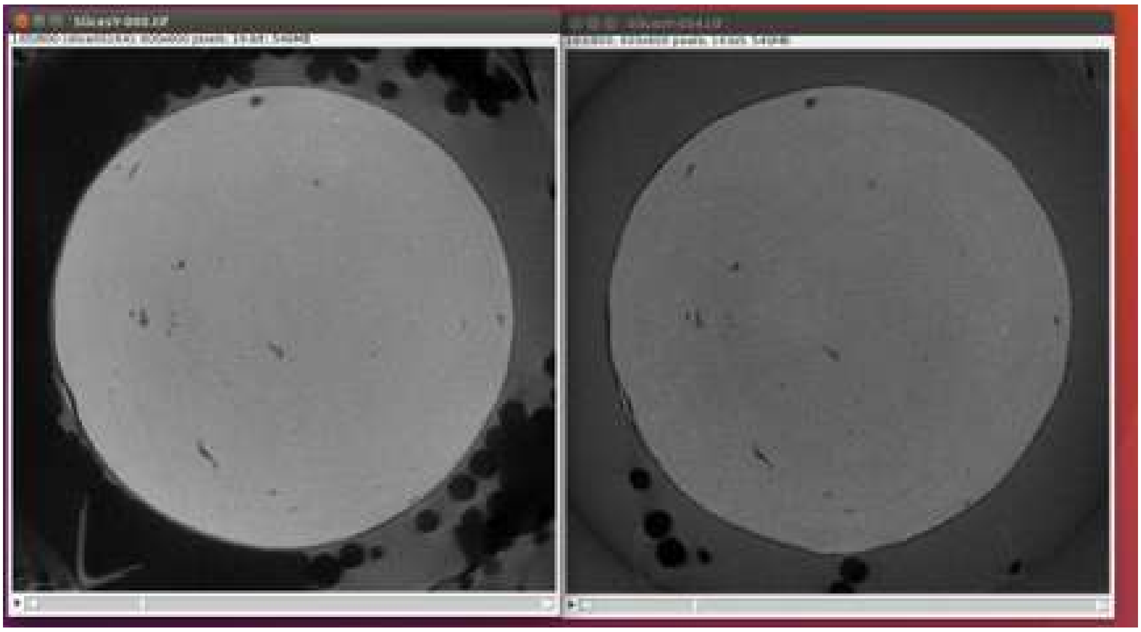

Figure 6.24: Cross section chosen at the bottom (left) and top (right) before freezing

6.7 Further analysis

The deformation analysis allows to confirm that specimen subjected to 1D freezing elongate. Then, hypothesis (1) may considered confirmed about the change in density at the slice 650 (see Section 6.4). Further analysis were realized about the dark zone, since it does not develop during

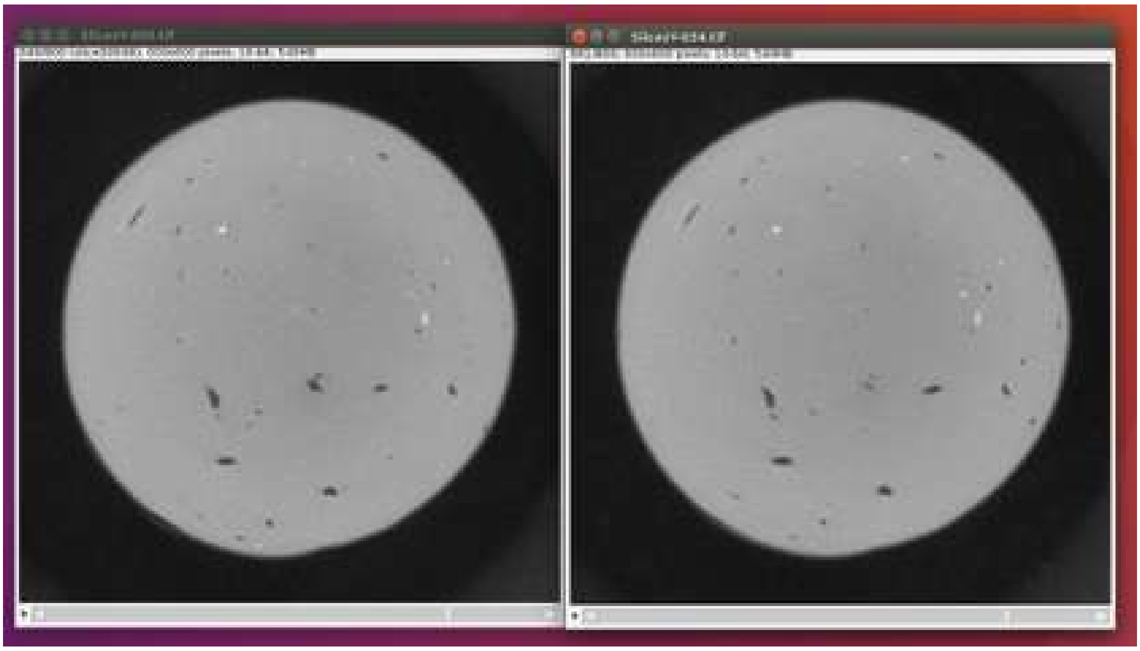

Figure 6.25: Cross section chosen at the bottom (left) and top (right) after freezing

the 1D freezing processes, proposed in the following chapter. First the minimum gray value within this zone was computed for each 3D image taken during the freezing. Such values were plotted against the time (Figure 6.26). The slope of the curve changes over the time. In particular, the gray value rate decreases in the first 15 time step, after which it increases from about α_1 = 320 gray values/step to α_2 = 420 gray values/step and then decreases again. Such result suggests that the gray value in the dark zone is influenced by the sinking of the specimen into the brine. Brine at −12 °C got in contact to the later surface of the sample. Furthermore, as it is visible from Figure 6.9, in the dark zone region, outside the specimen, the background becomes less dark. It suggests that the EPS granulates are wet.

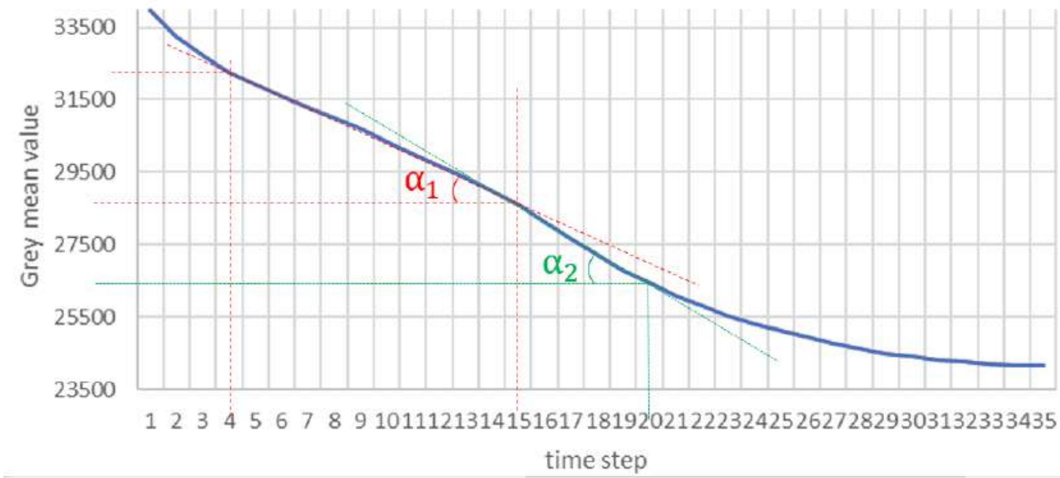

Figure 6.26: Rate of the mean of the grey value over the time (35 step of 6 min)

Chapter 7

Short-term deformations in 1D freezing

In permafrost or in seasonally frozen soil, temperatures usually does not drop below $-5\,^{\circ}\mathrm{C}$. Contrary, lower temperatures are imposed to stabilize soil or get it impervious by the Artificial Ground Freezing (AGF). In this case, if the Liquid Brine System is adopted, brine circulates in pipes with temperature between $-25\,^{\circ}\mathrm{C}$ and $-30\,^{\circ}\mathrm{C}$, while soil temperature drops below $-80\,^{\circ}\mathrm{C}$ when a Liquid Nitrogen System is installed [Chang and Lacy (2008)]. The design of Ground Freezing System needs to predict the short-term volumetric change of soil, in order to quantify the applied stresses on the surrounding soil and avoid damages on the near buildings and structures. Furthermore, available methods to accurate estimate the thaw settlement after the Ground Freezing are not been developed yet. As an attempt to increase the knowledge regarding these issues, analysis were carried out to extend the understanding of these phenomena and to increase data and information, which are critical for a good coupled thermal-hydro-mechanical analysis.

The experiments were performed on clay specimen whose deformation effects were pronounced during freezing, as seen in the previous chapter and by using the chamber 2 as freezing chamber, as described in Section 6.1. The frost penetration and heave is first analyzed for different bottom freezing temperature, then the clay's behavior is examined under one freeze-thaw-freeze cycle.

7.1 Brine melting point

In order to obtain a specific bottom temperature, a review about *colligative properties* was realized. Such properties depend just on the number of solute particles dissolved in the solution and not on their chemical nature [Pasquetto and Patrone (1994)]. Among these, *Freezing point depression* is a colligative property observed in solutions that results from the introduction of solute molecules to a solvent. The freezing points of solutions are all lower than that of the pure solvent and is directly proportional to the molality of the solution *m*. The molality corresponds to the number of moles of solute per kilogram solven [Atkins and De Paula (2009)]. The proportionality constant is called *cryoscopic constant* and it depends on the nature of the solvent, which for water corresponds to K_{cr}=1.853 Kkg/mol. The freezing point depression was computed using the formulation:

$$\Delta T_b = imK_{cr} \tag{7.1}$$

where i is the number of salt's ions dissociated in the solution.

Once the solute is chosen to mix with water and the freezing depression is fixed, the grams of salt can be calculated.

For the experimental campaign, NaCl salt was added to water. Since it was bought as commonly salt to cook, it was not pure. It contained some anti floucculant agents which made it difficult to obtain a perfect prediction of the solution melting point.

Calculation of the salt amount on the basis of molality is no more valid when a freezing depression to the *Eutectic point* is asked. The Eutectic temperature is the lowest possible melting temperature of a solution. Sodium chloride and water form a eutectoid when the mixture is 23.3% salt by mass with a eutectic point at −21.2 °C.

In the following table, the amount of salt to add to 2.6 kg of water, to obtain -5, -10 and −21 °C is shown. For the case of −10 °C and −21 °C the actual recorded melting temperature were −12 °C and −22 °C, respectively.

Table 7.1: Mass of salt calculated to obtain -5, -10 and −22 °C melting temperature for 2.6 kg of water

T (°C)	-5	-10	-22
Salt mass (g)	200	400	600

7.2 Image processing for 1D freezing analysis

Results about 1D freezing were obtained just after the 3D x-ray scans processing. In such section, they are explained the procedures adopted to quantify the freezing period, the frost front and the frost heave. The scanning of 1D freezing process was done for three different bottom temperature: -5, -12 and $-22\,°C$. For the $-5\,°C$ freezing the process was recorded until some hours after the sample started thawing. For the $-12\,°C$ freezing, the scanning was extended for a second freezing and stopped when sample started to thaw. Furthermore, for this case a second freezing was done after the sample got completely melted. Due to scheduling reasons, the third freezing process was scanned for just 6 h and 30 min.

For each bottom temperature case, series of scans with 6 min interval were conducted. The time of x-ray scan was 5 min, while between two scans 1 min was spent to store the data. The scanning was realized at a spacial resolution of $120\,\mu$m. Each set of scans was manually reconstructed by using the software XACT and then joined a in 3D image (stack). For each 1D freezing, several stacks were obtained and sorted in ascending order form 0, the first.

The freezing period was identified as the time from the start of freezing and the start of thawing. The beginning of thawing was associated to the moment in which frost front started to go downward. Furthermore, it was noticed such moment corresponds to the relative minimum temperature recorded at the top of the sample (Figures 7.6 and 7.7).

By a first visual observation of the consecutive 3D images, the last stack before the thawing started was identified. Then, for the 1D freezing at $-12\,°C$, a range of about 30 stacks was chosen, placing in the middle the approximated freezing end. Since the other freezing processes were scanned for less time, all the stacks were considered. For each case the 3D images were *concatenated* to create a 4D image. For the stack approximately identified as freezing end, the frost height was detected and identified as the height in which ice lenses are no longer visible.

Once obtained the 4D image, all the horizontal sections was cropped by a square cross section with size 36x36 mm^2. The part of the image, which was outside the square, was removed to avoid boundary noise.

The mean of the grey scale values was calculated as an average among the grey values in the square and then plotted against the time. First, the grey value trend over the time was plotted at the maximum frost front height. Since no much changes in density were visible at that height, the grey values were plotted for the fourth slice below the frost front, *i.e.*, 0.5 mm down.

Following such procedures, the graph in Figure 7.9 were obtained.

As discussed in Chapter 6, the soil is subjected first to suction and then it is crossed by ice lenses. As the thawing starts, the frost front starts dropping and density increases again. For this reason a relative minimum is expected in the graph of grey mean value against time. The relative minimum marks the end of the freezing period. In Figures 7.9, the graphs of change in grey values over the time for -5, -12 and $-22\,°C$ as bottom temperature are shown.

For the freeze-thaw-freeze (T=$-12\,°C$), the followed procedure was that above, but changes were made in the vertical position of the slice considered for measure the grey value. At the end of the second freezing, at the frost front ice lenses were more pronounced along the sample edges. Moving the 36x36 mm^2 square to the ages means incorporating grey values outside the sample, which would invalid the measurement.

The problem was solved by keeping the 36x36 mm^2 square in the center but moving it below. The section in which ice lenses are no longer existent was found and the 36x36 mm^2 square was moved to the fourth slide down, *i.e.*, to 0.5 mm down.

The detection of the thawing end was simpler than of end of freezing. Indeed, once the first freezing was over, the scanning interval was increased from 6 min to 16 min. Then, the last 3D image in which ice was still existent was easy identified. In Figure 7.1 are shown the vertical section observed at the last recorded instat of thawing and the one recorded once the thawing was completely over.

In the case of $-22\,°C$, the scans were interrupted after 6 h and 30 min. As shown in Figure 7.9, no relative minimum was detectable and then the freezing period was not over after that time. Despite this, the identification of the freezing period was possible thanks to the data recorded by thermocouples during the whole process. For each 1D freezing case, 6 thermocouples were placed in different position of the freezing chamber.

For all the freezing processes analysed, but for the $-22\,°C$ case , the comparison among the freezing period and temperatures developments shows that the end of freezing period corresponds to the relative minimum of the temperature recorded at the specimen top. For this reason, it is assumed that the same thing happens for the 1D freezing at lower temperature. This allowed for identification of the time for maximum heigth of the frozen zone.

A spike can be seen in 7.8 for the $-22\,°C$ freezing due to the thermocouples re-positioning.

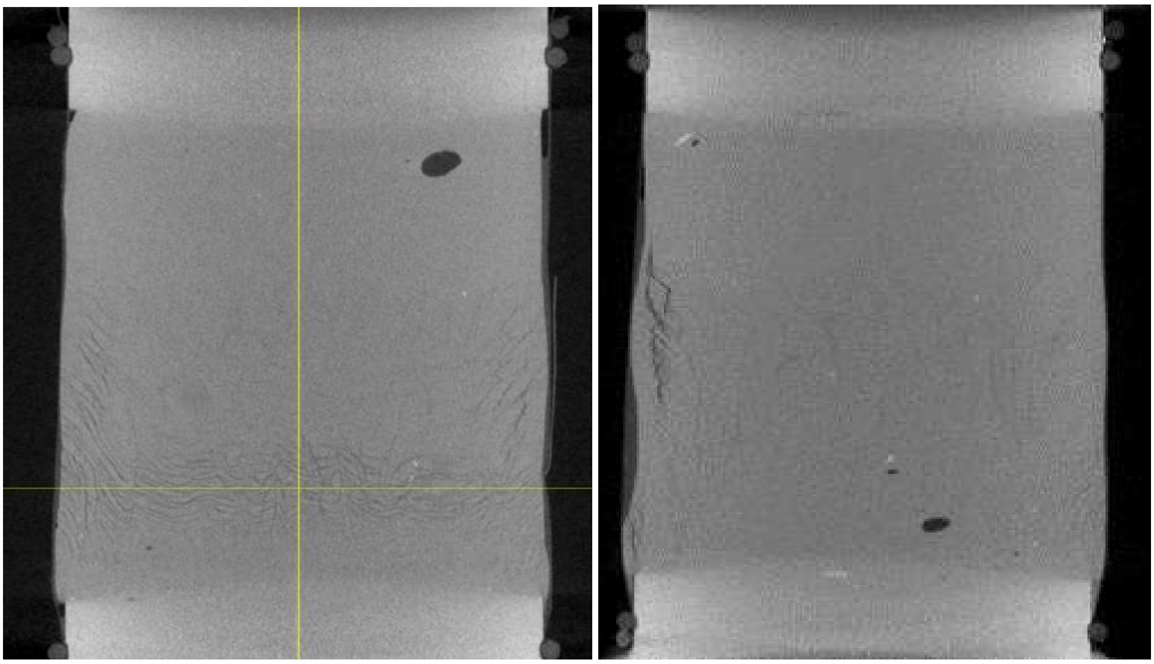

Figure 7.1: Onsoy clay vertical section (left) at the last recorded instat of thawing (right) once the thawing was completely over

In Software ImageJ (Fiji), the height of the frozen zone was identified by the last position of the horizontal section in which ice lenses were visible. Due to presence of aluminum caps and the density contrast between sample and cap, an x-ray reconstruction artefact exists at the interface between soil and caps. The height of the specimen was considered at to the beginning of such metal caps, which was identified as the first (closer to the soil) slice in which grey values of metal caps are homogeneous and it was marked as end of the specimen. Figures from 7.2 to 7.5 show the characteristic sections identified at the end of each freezing process. Final frost heave was calculated as the difference of the height of the specimen before freezing and at the end of the freezing period.

Furthermore, frost heave was computed over the time by extracting the axial elongation from the Φ matrix (see 6.3) calculated between the new image and the reference one during freezing by *Digital Image Correlation* (DIC). It's trend over the time is shown in Figures 7.14 for the different bottom temperatures.

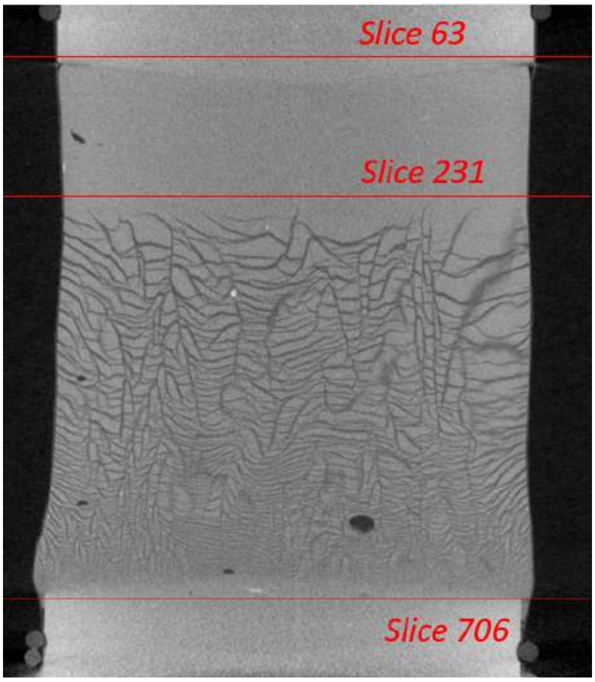

Figure 7.2: Characteristic sections identified at the end of the −12 °C first 1D freezing

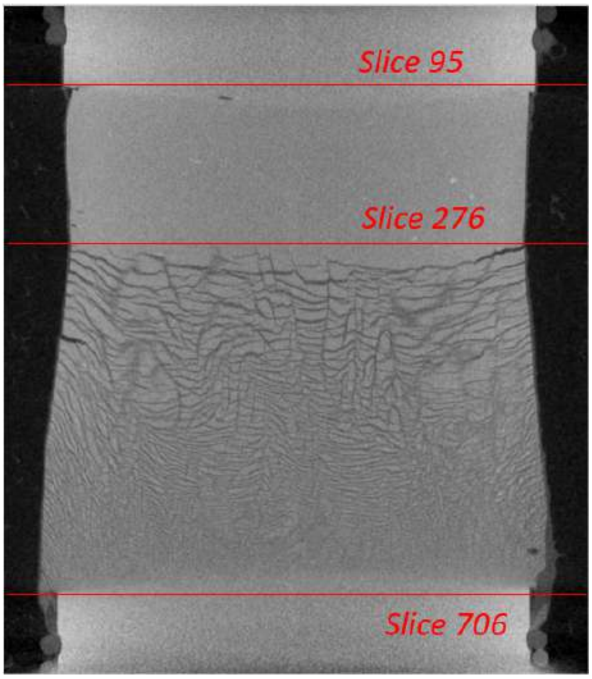

Figure 7.3: Characteristic sections identified at the end of the −12 °C second 1D freezing

7.3 Influence of freezing temperature on clay deformation

As shown in Section 5.5, the freezing temperature, or the thermal gradient, affects the ice lenses size. Contrary to the three-dimensional freezing presented in Chapter 5, the thermal gradient is now nearly uni-directional. This allows to deeper investigate the freezing process and extract further information about frozen soil characteristics. In table 7.2 and in Figure 7.10 are shown the results obtained from the analysis in Section 7.2.

Wang et al. (2017) uni-diretional froze unsaturated clay specimen to -5, -7, -10, −15 °C. They found that for lower bottom temperatures the maximum frozen height gets longer and thermal equilibrium is reached later (Figure 7.12). Furthermore, they observed that as the temperature within the specimen stabilized during the freezing process, the specimen reached a maximum height (frost heave). At thermal equilibrium, the maximum frozen height was assessed based on the temperature distribution and interpolation.

Also for the current case, the maximum frozen height is longer for lower freezing temperature as shown in Figure 7.11. Contrary to the previous case, measurements were done on the basis

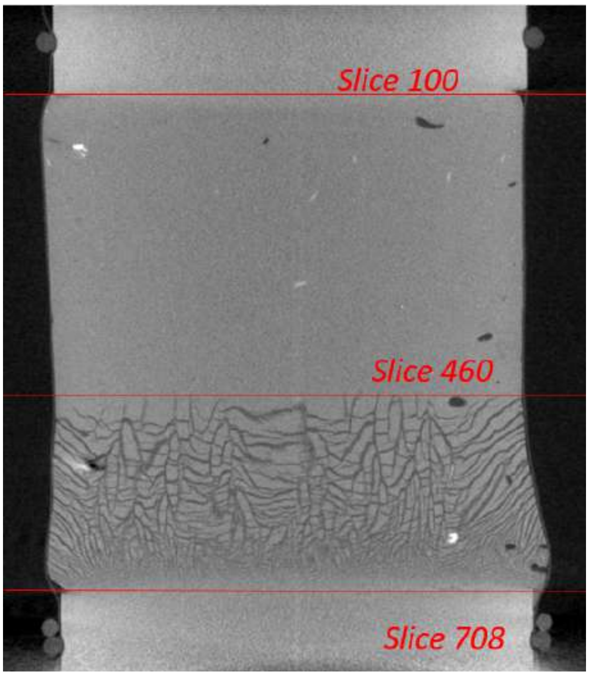

Figure 7.4: Characteristic sections identified at the end of the −5 °C 1D freezing

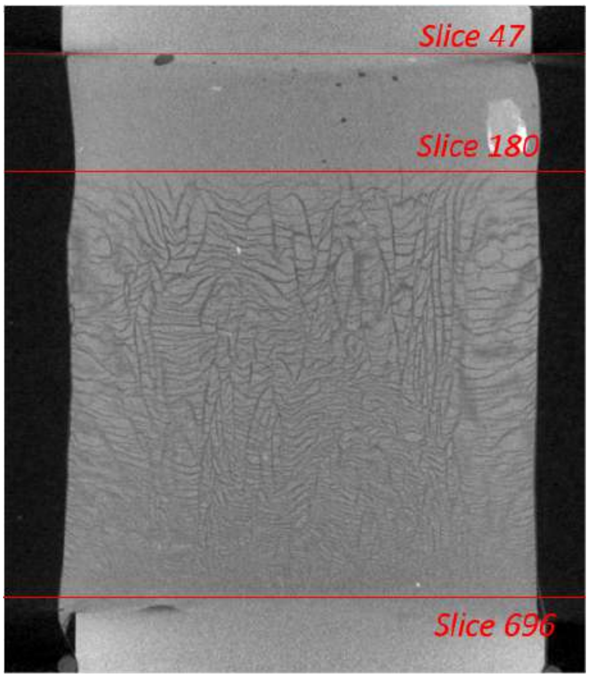

Figure 7.5: Characteristic sections identified at the end of the −22 °C 1D freezing

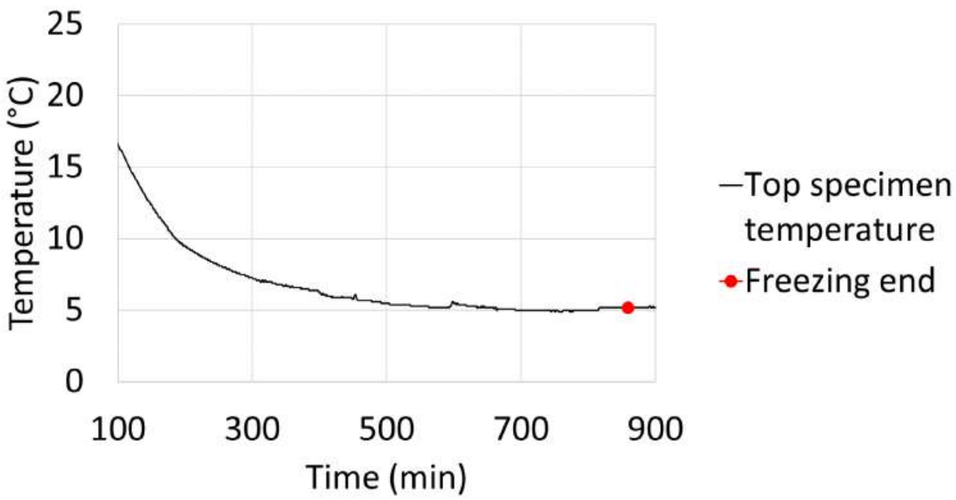

Figure 7.6: Top temperature over the time for −5 °C 1D freezing

of tomography scans processing. Image processing is considered to be an accurate and non destructive way to detect the frost front, since the freezing temperature of water in the soil is not easy to precisely estimate. Indeed, it depends on the salt which is dissolved inside it and on the

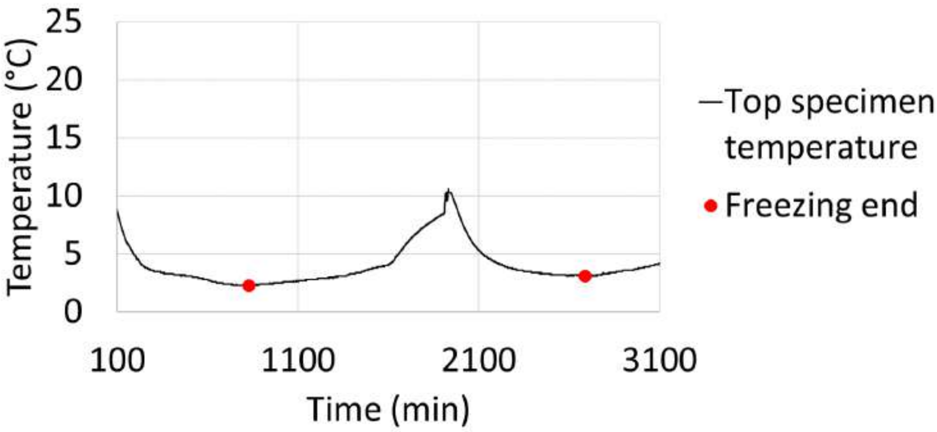

Figure 7.7: Top temperature over the time for −12 °C 1D freezing

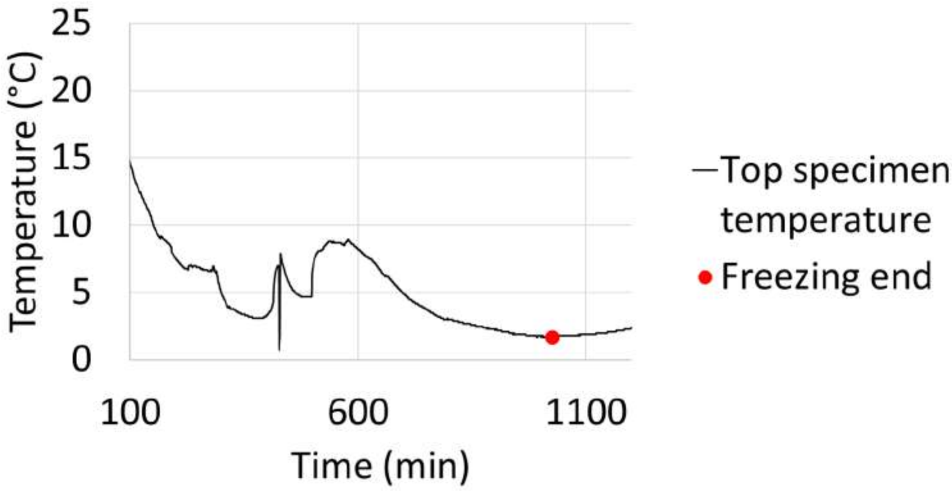

Figure 7.8: Top temperature over the time for −22 °C 1D freezing

interactive forces with granular particles. At the freezing end, frost heave was measured equal to 4.1% for−5 °C after 14 h freezing and 10% for both −12 °C and −22 °C after 13 h and 6 h and 30 min freezing, respectively.

As shown in Figure 7.11, the freezing period (time between the freezing and the thawing beginning) was longer when brine melting temperature was −22 °C (17 h) and almost similar for the −12 °C and −5 °C cases (14 h and 13 h, respectively). Such dissimilarities in freezing period could be due to brine latent heat. Contrary to pure ice water, whose latent heat of melting is almost constant for starting temperature, for a water-NaCl solution, Han et al. (2006) found that

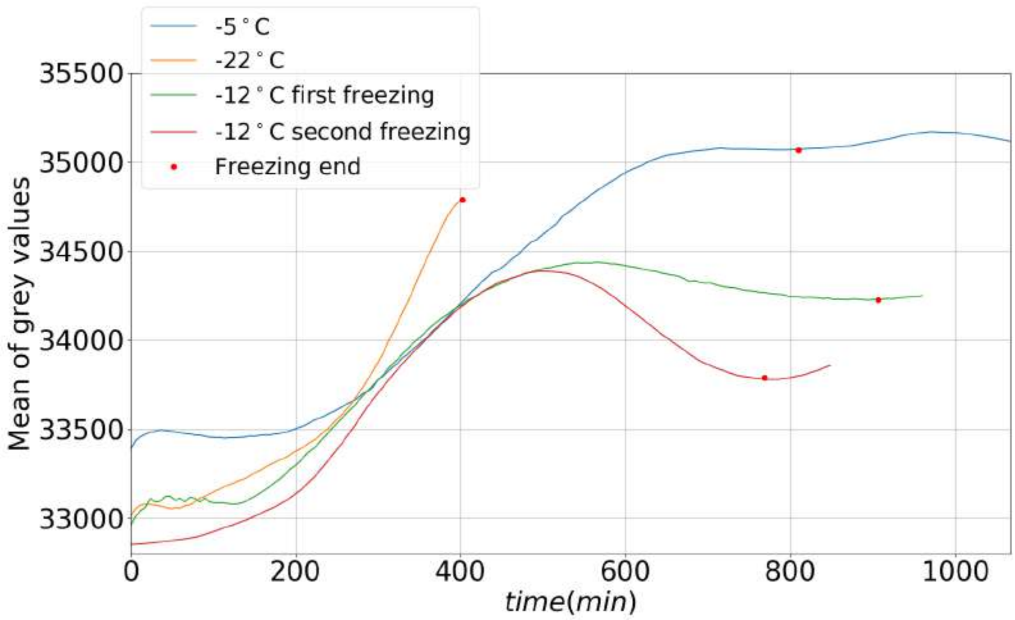

Figure 7.9: Mean of grey values over the time for -5, -12 and −22 °C 1D freezing and for −22 °C second 1D freezing at the maximum frozen height

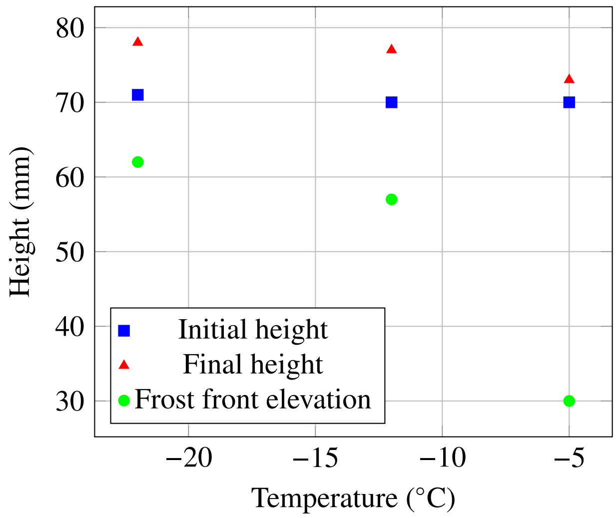

Figure 7.10: Specimen initial and final height and frost front elevation for -5, -12 and −22 °C 1D freezing

it depends on the concentration of salt in water.

As recorded by thermocouples, after a short period in which brine temperature was constant, it started to increase despite of not all the frozen brine got melted. That because a not perfect insulation system was adopted. In particular, in the case of brine melting point of -12 and −22 °C,

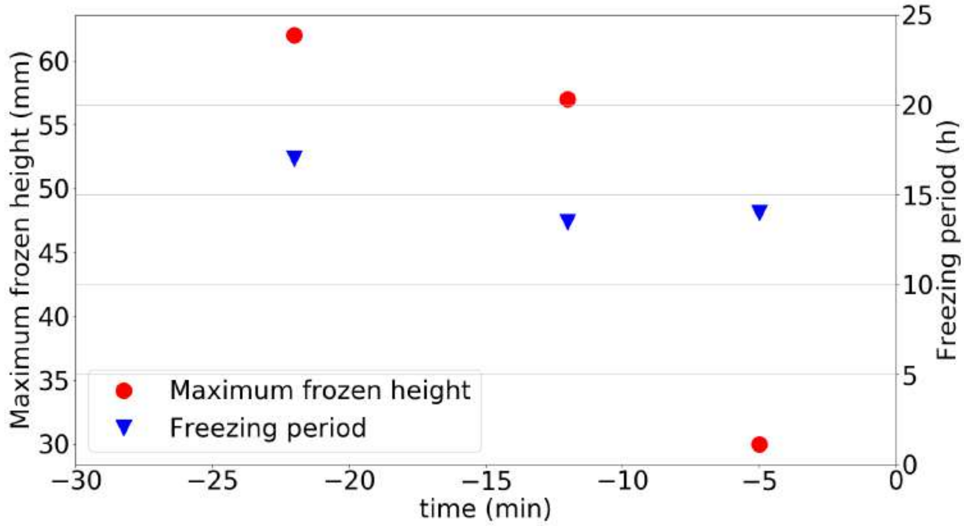

Figure 7.11: Maximum frozen height and freezing period obtained in this work

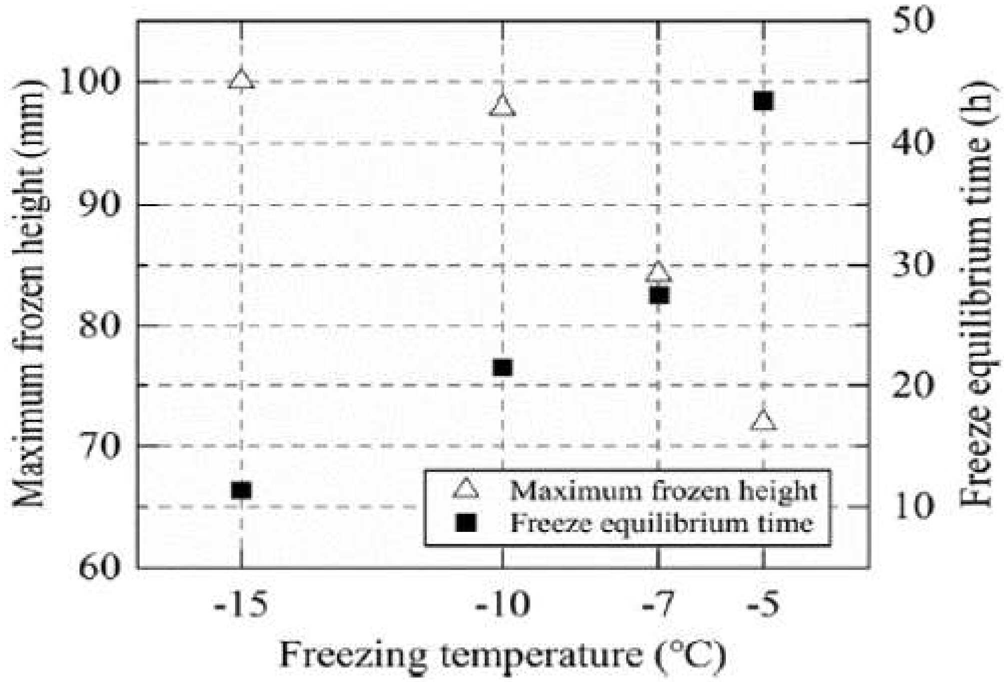

Figure 7.12: Maximum frozen height and freezing period from Wang et al. (2017)

temperature was constant for almost the first 500 min, then it started to increases with a rate of about 0.40 °C/h. While the −5 °C bottom temperature increased from the first instant with about

0.25 °C/h rate. For such reasons, despite of the purpose for such measurements was to detect the freeze equilibrium time, they can give only an idea about how long was the specimen freezing.

Table 7.2: Summary of specimen physical characteristics for -5, -10 and −22 °C 1D freezing

T (°C)	-5	-10	-22
Water content (%)	56	51	55
Freezing period (hours)	13	13.5	17
Initial height H (mm)	70	70	71
Final height H_F (mm)	73	77	78*
Frost heave (mm)	3	7	8*
Frost front elevation h_F (mm)	30	57	62*
Frost heave (%)	4.3	10	9.9*

⋆ measured after 6 h and 30 min from the freezing beginning.

Frost front position over the time was measured in the 3D images every hour from the freezing beginning until its end (start of thawing). It was identified as the last horizontal section, counting from below, in which they ice lenses appeared. The development is shown over the time in Figure 7.13 for -5, -10 and −22 °C 1D freezing. For the first minutes of freezing the slope of all the curves is almost equal. Then, the freezing rate is slowing down for all the cases. For the −5 °C freezing, frost front appears stable after almost 750 min, indicating that a steady state situation was reached. The same thing was not observed for the other 1D freezing, since a plateau is not identified for such cases.

Frost heave over the time was computed over the time as explained in Section 7.2. Figure 7.14 shows the graphs obtained for -5, -10 and −22 °C 1D freezing. By comparing the first 400 minutes for each 1D process, once can say that frost heave occurs faster at lower temperature. For the -12 and −22 °C cases, it follows a curved trend with reduction in inclination, while for the −5 °C case it appears more linear. Then, contrary to the first cases in which frost heave seems be over in the first 500 min, for the −5 °C case it occurs more slowly and with almost the same speed for longer time. For the case of −12 °C, maximum frost heave was measured almost 9% after 550 min by DIC, while at the end of the freezing process it was manually measured almost equal to 10%. Such changes is due to the fact that between about 450 and 750 min, the function did not converged before 100 iterations. For the other cases, the two kind of measurements correspond.

Comparing frost front propagation and frost heave trend over the time for −22 °C case, it is seen that the frost heave shows the tendency to stabilize at 400 min while frost front looks like

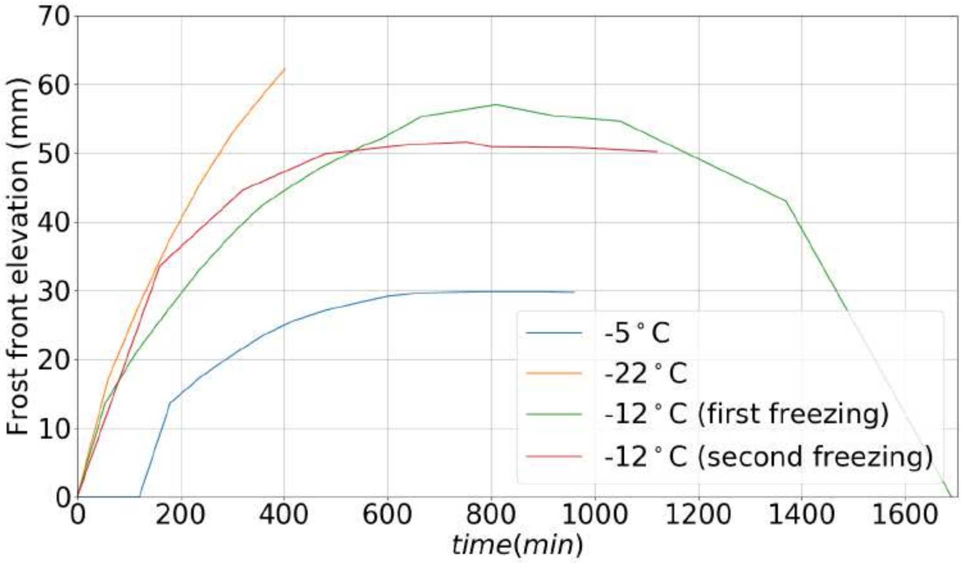

Figure 7.13: Frost front elevation over the time and freezing temperature for -5, -12 and −22 °C and −12 °C second freezing

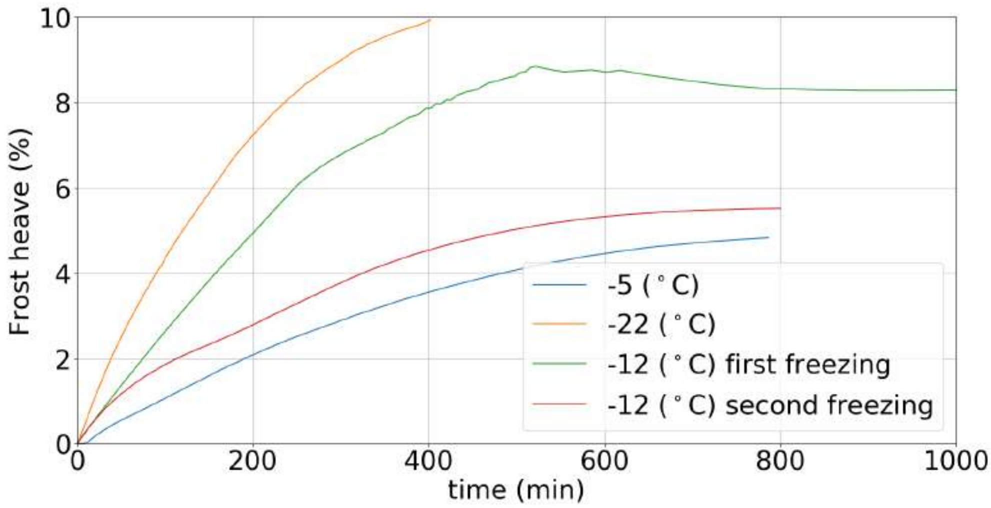

Figure 7.14: Frost heave elevation over the time and freezing temperature for -5, -12 and −22 °C and −12 °C second freezing

propagate with a speed of 10 mm/h. A similar behavior is shown by the −12 °C freezing. Indeed, in this later case at about 500 min, the frost heave slope is starting to decrease, while frost front continues to propagate. Such behavior is not evident −5 °C freezing.

Further comparisons of the different freezing cases can be done in terms of average of ice lenses thickness. Average ice lenses thickness was computed using the technique explained in Section 5.4. Figure 7.15 shows that ice lenses thickness gets thinner with lower bottom temperature. Surely, as seen in Chapter 5, an accurate comparison can be realized taking into account the water content and rate of freezing.

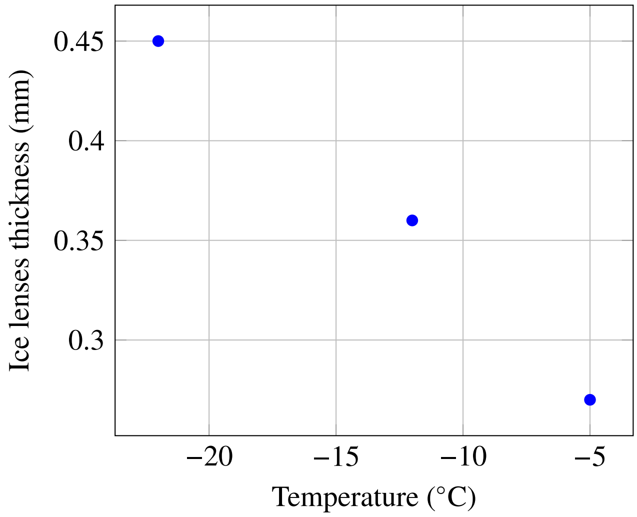

Figure 7.15: Average ice lenses thickness for the three different 1D freezing processes

7.4 Freeze-thaw-freeze cycle

A freeze-thaw-freeze cycle was performed on one clay sample. The first freezing was at −12 °C and the second at −13.5 °C, since the brine mixture used in the second freezing had a slightly lower melting point.

Contrary to what seen in literature (*e.g.*, Wang et al. (2017)), the thawing was slowly, keeping the melting brine below the specimen.

The period of the first freezing was measured 13.5 h. Thawing took 14 h and the second freezing period (12.5 h) was recorded 1 h shorter than the first one.

Figures from 7.16 to 7.19 show the vertical section of the same sample in unfrozen state, after the first and second freezinf and after the thawing. Figure 7.18 shows that the freezing causes damage in the soil's structure, leaving almost vertical cracks after the thawing. These cracks could be the reason for the increase in permeability measured by Chamberlain and Gow (1979) after a freeze-thaw cycle. After the thawing, water appear trapped between the sample and the membrane, showing that water leaks out from the clay during the thawing. As we have seen in Chapter 3, freezing process involves a redistribution of the water throw out the sample. Due to the cryogenic suction, the water goes downwards, causing the densification of the top part while the bottom zone becomes softer. Due to such redistribution, a certain amount of water passes from a bond with particles state to a free state. As Tommik (2017) observed, when clay thaws new bonds between particles are formed. Thawed clay sticks together forming larger particles. Increasing particle size will decrease the specific surface area and therefore the amount of water that can be bound to that area will also decrease. Then, new cracks and more amount of free water, together with a slight decrease in temperature, might lead to a faster freezing.

The frost front was tracked during the first and the second freezing. The sample height was also measured from the 3D images. As shown in Figure 7.13, frost front initially propagates at similar speed. Then, the second freezing frost front keeps an higher speed than the first one, after which it drastically decreases, keeping the frost front an almost stable position for 300 min.

The frost heave was measured for both freezing cases, once the freezing period was over. As shown in Table 7.2 , it is measured equal to 10% for the first freezing and 6% for the second one. Despite of the undrained system, a 4% reduction in frost heave is observed.

As shown in Figure 7.18, water in free state exists between the sample and the membrane after thawing. An hypotesis is that the water particles are less bond to the soil particles, or even they get free. This might lead to think that its freezing temperature is increased. Since the system is undrained, more water in free condition exists for the second freezing. According to this, a larger amount of water will freeze at the same bottom temperature than the previous freezing, recording then an higher frost heave.

Since the above hypothesis were not confirmed, an analysis in terms of diameter was realized in order to see if the real frost heave reduction was hidden behind a change in section.

The diameter of the cross section along the entire sample (70 mm in height) was measured when soil was in unfrozen state, at the end of the first and the second freezing and at the end of thawing (Figure 7.20). The diameter measurement was under the hypothesis of circular cross section along the entire, despite of the deformation process is three-dimensional. The explanation of each curve is in what follows:

1. in *unfrozen condition* the sample has a constant 70 mm diameter, but at the top and bottom, probably due to sample handling during its preparation and x-ray artefact (since the closeness to metal cups);

2. at the *end of the first freezing* we see a global reduction in diameter along the height of the sample, which slightly increases ahead the frost front. At the frost front the minimum diameter is measured, telling that the denser zone develops almost at the same elevation of the frost front;

3. after the *end of the thawing* the diameter becomes less than in the unfrozen state in the upper zone. The difference in size is due to the redistribution of water from the upper zone to the bottom. Since no increase in diameter is observed in the bottom zone, the specimen does not absorb such water but it leaks out and gets trapped between the soil and the membrane.

4. At the *end of the second freezing* a large expansion in section at the bottom is visible, while the diameter at the frost front is smaller than in the first freezing.

As Miller (1972) explained in its ”Secondary frost heave theory”, frost heave does not exist just due to the expansion of water but it is also the result of its slow redistribution though the partially frozen region of the soil due to the existence of a *premelted film* of water at lower temperature than the freezing one. On this basis, one may say reduction in frost heave occurred since redistribution of water was not accentuate as the previous freezing. Indeed, due to the freeze and thaw, a great amount of water is already migrated downwards and a part of it changed its status from bond to free water. Such conditions lead to a water demand by the bottom part to the zone above which is satisfied with a less amount of water than the previous freezing. Cryogenic suction acts also on the free water already existent in the bottom zone, which is suck into the specimen and frozen, involving in an increase in diameter.

Furthermore, the diameters analysis allowed to see that the freeze-thaw process is reversible in the bottom zone, since the cross section diameter takes back its size.

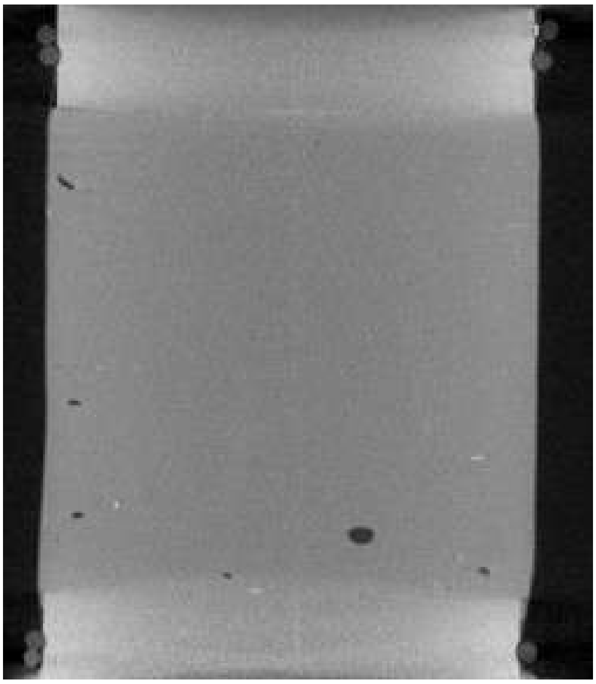

Figure 7.16: Specimen's vertical section in unfrozen state

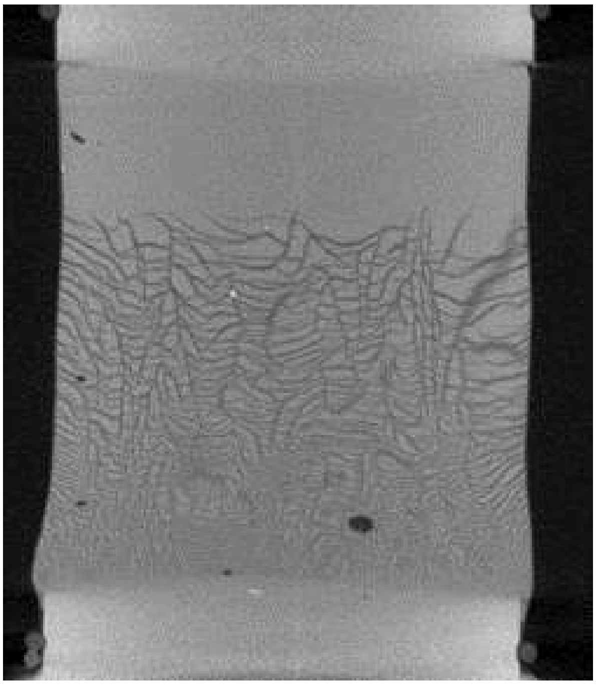

Figure 7.17: Specimen's vertical section at the end of the first freezing

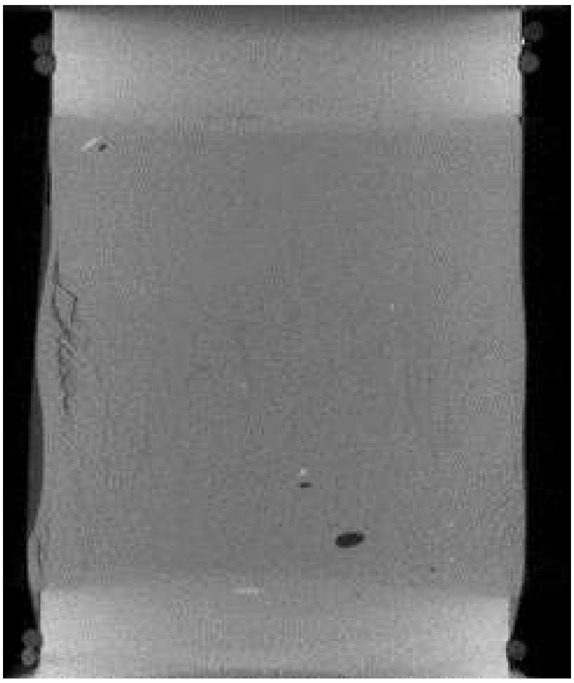

Figure 7.18: Specimen's vertical section at the end of the the thawing

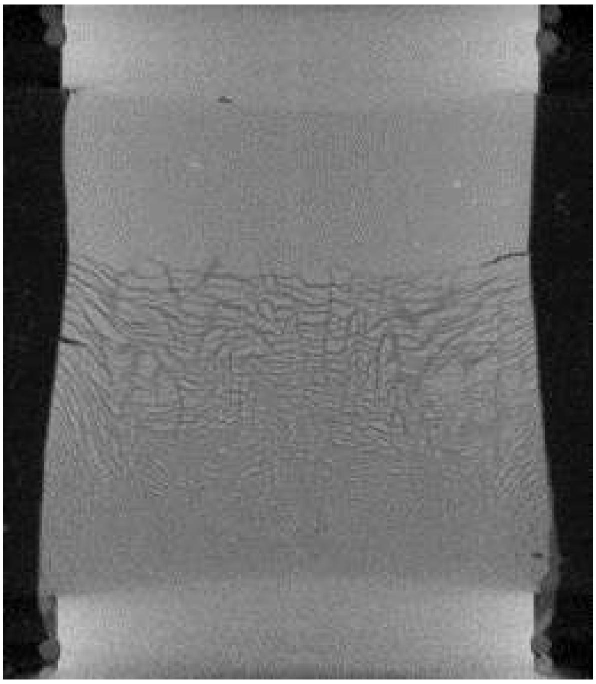

Figure 7.19: Specimen's vertical section at the end of the second freezing

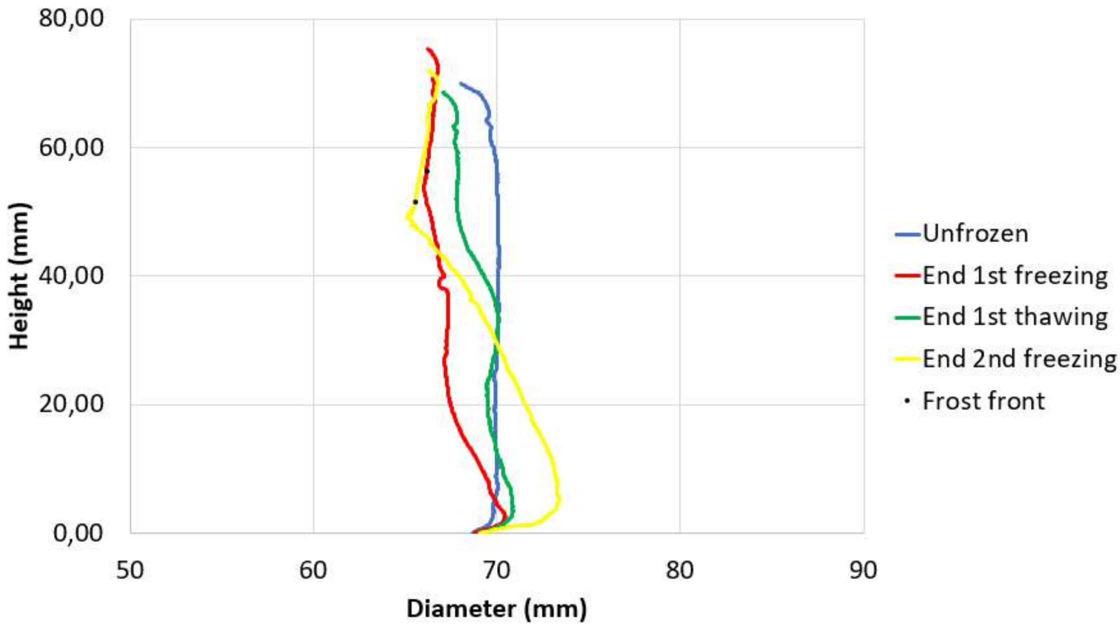

Figure 7.20: Diameter along the height specimen for four different instant

Chapter 8

Frost front penetration prediction

Prediction of frost heave and frost front penetration is critical in cold regions civil engineering. Infrastructures, buildings and foundations are always under damage risks by frost heave and thawing settlements and millions dollars are spent annually on their preservation and restoration. Since 1960s, several sophisticated models are developed in order to predict frost heave and frost front penetration in soils. Groenevelt and Grant (2013) identified two principal ”schools”. The fist is the school of D.M. Anderson of the Cold Regions Research and Engineering Laboratory (CRREL) in Hanover, New Hampshire. The second is the school of Bob (R.D.) Miller, of Cornell University, Ithaca, New York. Over the years, new schools are born and new refined concepts are continually introduced to the ancient theories in order to obtain a better prediction of behavior frozen soil. Such theories have often foundation on equilibrium thermodynamic concepts (*e.g.*, Clapeyron equation) and use hydro-dynamics (*e.g.*, Darcy equation) and mechanics notions.

8.1 Stefan formula and Modified Berggren equation

Despite of the existence of several sophisticated model in literature, frost front prediction is usually realized by manually applying simplified equation for Infrastructure Engineering. One of the first and simplest equation proposed for this scope is the *Stefan Formula*.

On the hypotesis of 1D freezing, Stefan formula assumes that the latent heat of soil moisture is the only heat which is removed when freezing the soil. Thus, the thermal energy which is stored in the form of volumetric heat and released as the soil temperatures drop to and below the freezing point is not considered [Aldrich Jr (1956)]. The assumption of volume heat negligibly involves in the overestimation of the frost front penetration.

The Stefan formula states that the heat conducted to the ground surface through the frozen layer, expressed by the Fourier's equation (left term of Eq.8.1), is equal to the latent heat released by a layer of soil dx thick in time dt, expressed by the conservation of thermal energy, in which the volumetric heat is neglected (right term of Eq.8.1).

$$k_f \frac{dT}{dz} = L\frac{dz}{dt} \tag{8.1}$$

where k_f is the thermal conductivity,vertically measured in the frozen soil from the ground surface and L is the latent heat of water L_w inside the soil, computed taking into account the soil's water content w and its dry density ρ_d (eq. 8.2).

$$L = L_w w \rho_d \tag{8.2}$$

By integrating and solving for z, one obtains:

$$z = \sqrt{\frac{2k_f}{L}\int_0^{t_f}(T_P - T_S)dt} \tag{8.3}$$

in which T_S is the temperature of soil surface at depth $z_S = 0\,\mathrm{m}$ depth. T_P is the temperature at the frost front depth z, unknown of the problem. t_0=0 is the initial time of freezing and t_f is the period of freezing. The term $\int_0^{t_f}(T_P - T_S)dt$ corresponds to the Surface freezing index (SFI), usually expressed in days Fahrenheit or days Kelvin. It is also possible to use the Air freezing index (AFI) by adding a coefficient n, depending on the kind of layer above the soil surface (for instance snow, concrete and bituminous mix). The AFI is expressed as the SFI but it consider the air temperatures over the time.

In this was Eq.8.3 becomes:

$$z = 416\sqrt{\frac{k_f nAFI}{L}} \tag{8.4}$$

Due to the overestimating trend of the Stefan equation, several modifications were proposed for it, over the time. Noways, design of pavement structures in cold regions is realized on the basis of the (UFC), which proposes to use the *Modified Berggren equation* (Eq. 8.5). This last corresponds to the Stefan formula corrected by introducing a corrective parameter λ, obtained on the basis of thermodynamic theories.

$$z = 416\lambda\sqrt{\frac{k_f nAFI}{L}} \tag{8.5}$$

The parameter λ depends on the volumetric heat capacity, computed as the average between that of the unfrozen soil c_u and the frozen soil c_f (Eq.8.6) , on the latent heat of water iside the soil L and on the surface temperature T_S and freezing temperature of water inside the soil T_P by the parameters μ and α, expressed in Eqq.8.7 and 8.8. In Eq. 8.8, T_m is the recorded maximum annual temperature in the zone. Once computed μ and α, λ is calculated from the graph in Figure 8.1.

$$c_{avg} = \rho_d(c + 0.75\frac{w}{100}) \tag{8.6}$$

$$\mu = \frac{c_{avg}}{L}(T_S - T_P) \tag{8.7}$$

$$\alpha = \frac{T_m - T_P}{T_S - T_P} \tag{8.8}$$

8.2 Experimental data and model results comparison

In order to realize a comparison between experimental data and frost penetration model results, the −12 °C 1D freezing case was considered. The Stefan formula expressed as Eq.8.3 was applied over the time, considering the temperatures 0, -3, -4 and −5 °C as frost front temperature. The sample's metal bottom cap temperature recorded by thermocouples was considered as soil surface temperature T_S.

The thermal conductivity k_f, was computed as the average between the one of the frozen soil and that of the unfrozen one. The values were that measured for a clay sample by Kurz et al. (2017) and its properties are in Table 8.1 and they are equal to 1.21 and 0.90 W/mK for the frozen and unfrozen clay, respectively Following such procedure, the graph in Figure 8.2 was obtained. It shows The better interpolation to the experimental curve was obtained for -3 and −4 °C.

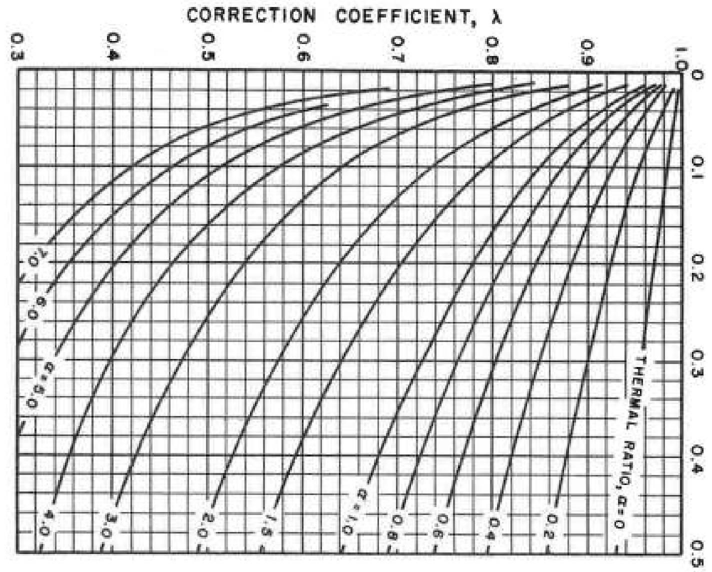

Figure 8.1: Correction coefficient in the modified Berggren formula from Aldrich Jr (1956)

Table 8.1: Plastic index I_p, saturation degree S_r, natural water content w_n and dry densityt γ_d measured for a clay sample by Kurz et al. (2017)

I_p	S_r	w_n (Mg/m3)	γ_d
24.2	85	36	1.3

The Modified Berggren equation was applied just for the last freezing instant (700 min), computing the SFI as the integral of all the temperatures recorded untill that instant and λ for the temperature T_S recorded at 700 min. By using the Modified Berggren equation all the frost front position predicted by the Stefan formula are reduced of few millimeters (Table 8.2).

The carried out analysis allows to say that the usual hypothesis of 0 °C temperature at the frost front involves in an overestimation of frost front penetration. This was already observed in literature for the Stefan formula. For 0 °C case, also the Berggren's λ parameter is not sufficient to match the experimental data. Contrary to the current practices, for the short-term clay freezing better results are obtained by applying the Stefan formula and considering that the freezing temperature, which corresponds to the temperature at the frost front, is actually some degrees below zero.

Table 8.2: Frost front position after 700 min −12 °C freezing by Stefan formula and Modified Berggren equation

T (°C)	0	-3	-4	-5
Frost front (Stefan) (mm)	71	61	57	53
Frost front (ModBerg) (mm)	68	59	56	51

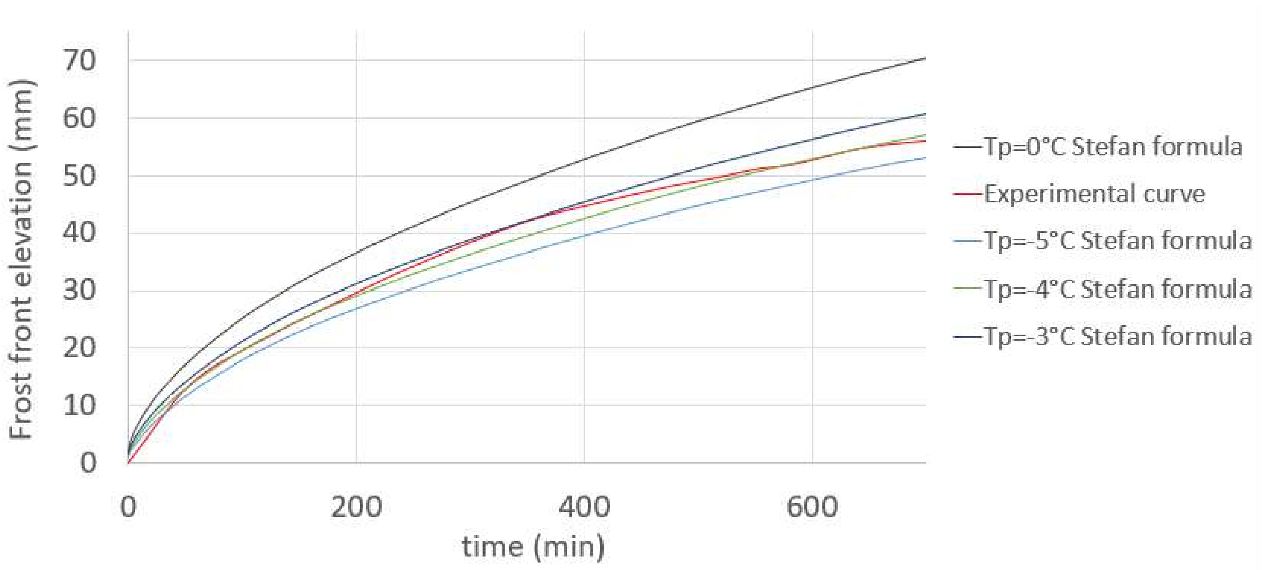

Figure 8.2: Frost front penetration over the time by Stefan equation for 0, -3, -4, −5 °C T_P

Chapter 9

Conclusion

During this master project several freezing procedures were investigated in order to find the one which returns an elementary representative frozen samples, homogeneous and isotropic. The required characteristics were uniformly distributed ice crystals and small in size respect to the soil matrix. In the way they cannot be identify as a separated phases from frozen soil.

First different sampling procedures were tested. Difficulties have been identified at this step, since the returning of air bubbles in the clay sample by using the sampling techniques explained in literature. Air bubbles affects the freezing process since they corresponds a preferential location for the initiation of ice segregation. Furthermore, recent study have revealed that water can infiltrate into deeper soil through preferential pathways where air-filled macropores exist at the time of freezing [Niu and Yang (2006)]. After some trials, the introduction of concrete vibrator in the clay slurry before consolidation was believed a good improvement for the specimen preparation, since it returns less air bubble porosity than the other methods tested (Figure 4.8).

During the three-dimensional freezing campaigns, two kind of soil were tested: Halden silt and Onsoy clay. In the Halden silt ice crystals were not identifiable by a $60\,\mu$m resolution x-ray tomography. Hence, it can be concluded that a reliable mechanical response of an Halden silt frozen specimen could be obtained by almost any freezing procedure.

For the Onsoy clay, ice crystals have been noted when the temperature drops below $-4\,°$C.

Three main factors were observed affecting the average of ice lenses thickness: the freezing temperature, the water content and the rate of freezing. Finally, among the freezing methods tested during this master thesis, the slow freezing to $-5\,°$C was identified as the best procedure to freeze, since it involves in the most homogeneous and isotropic soil material.

Two one-dimensional freezing campaigns were carried out. The cold was imposed at the bottom of the specimen.

During the first campaign, Halden silt and Onsoy clay one-dimensional freezing was compared. For the Halden silt, a net frost front was seen moving upwards without ice lenses development. Ice lenses grown in Onsoy clay and a three-dimensional deformation behaviour was observed despite of the one-dimentional freezing. Further analysis were carried out about the change in density and strains along the height of sample due to the imposed thermal gradient. Four different zones were identified where soil differently behaves.

For the second campaign, three different thermal gradient was imposed to the specimen and a freeze-thaw-freeze cycle was observed. Thermal gradient affected the deformation of the specimen. For this case, the analysis were focused on the quantification of the frost heave and the maximum frozen height. They were measured greater for lower bottom temperature. Frost front elevation increased at similar initial speed for all the cases and then it tends to stabilize (equilibrium-steady state) (Figure 7.13).

After one freeze-thaw cycle water was observed leaking out from the sample. It appears trapped between the membrane and the soil in Figure 7.18. After one freeze-thaw-freeze cycle frost front elevation and frost heave was measured less than after the first freezing. Furthermore, the equilibrium-steady state was reached in shorter time for the second freezing than for the first one. To further investigate this phenomenon, a diameter analysis was carried out. A global reduction in diameter was observed along the height of the specimen after the first freezing. The thawing induced sample's cross section to retake almost the initial diameter in the bottom zone, while in the upper zone the diameter keeps smaller than in the unfrozen state. After the second freezing, diameter increased above the one measured in unfrozen state, while it keeps smaller in the upper zone.

Results obtained during the second one-dimensional freezing campaign were applied on existing method for the prediction of the frost front penetration. Two equations were used: the Stefan formula and the Modified Berggren equation. The experimental results obtained for one case of freezing were well matched by the Stefan formula during the freezing period. In particular, a better interpolation of the experimental data was noted considering -3 or -4 °C as freezing temperature of water inside the soil. The Modified Berggren equation returned an overestimation of the frost front position after 810 min freezing.

X-ray tomography was critical for the understanding of the freezing process and the detection of short-term deformation. The digital image processing has been found an innovative and important instrument in the frozen soil analysis. Indeed, it gives the tools for the quantification of phenomena of which just qualify explanations exist in literature. For this reason, it would be a worthy ally for the improvement of constitutive model already proposed in literature. Furthermore, linked to mechanical test apparatus, it would improve the interpretation of the mechanical response of the frozen soil. Finally, it could fill the gap existent in the current body of knowledge regarding the phenomena involved by the freezing of soil and and the influence of freeze-thaw cycles on the soil physical, mechanical, hydraulic and thermal properties.

Bibliography

(2019). Introduction — spam 0.3.3.1 documentation. (Accessed on 06/14/2019).

Akagawa, S. (1988). Experimental study of frozen fringe characteristics. *Cold Regions Science and Technology*, 15(3):209–223.

Aldrich Jr, H. P. (1956). Frost penetration below highway and airfield pavements. *Highway Research Board Bulletin*, (135).

Andò, E. C. G. (2005/2006). *Experimental investigation of microstructural changes in deforming granular media using x-ray tomography*. Tesi di laurea, Université Grenoble Alpes.

Andersland, O. B. and Ladanyi, B. (2004). *Frozen ground engineering*. John Wiley & Sons.

Atakol, K. (1969). *Frost action phenomena*. Number 11. Pennsylvania Transportation and Traffic Safety Center.

Atkins, P. and De Paula, J. (2009). *Elements of physical chemistry*. Macmillan.

Bates, R. E. and Bilello, M. A. (1966). Defining the cold regions of the northern hemisphere. Technical report, COLD REGIONS RESEARCH AND ENGINEERING LAB HANOVER NH.

Black, P. B. (1995). Applications of the clapeyron equation to water and ice in porous media. Technical report, COLD REGIONS RESEARCH AND ENGINEERING LAB HANOVER NH.

Blaker, Ø., Carroll, R., L'Heureux, J.-S., and Klug, M. (2016). Characterisation of halden silt.

Burland, J. (1990). On the compressibility and shear strength of natural clays. *Géotechnique*, 40(3):329–378.

Chamberlain, E. J. (1981). Frost susceptibility of soil, review of index tests. Technical report, COLD REGIONS RESEARCH AND ENGINEERING LAB HANOVER NH.

Chamberlain, E. J. (1989). Physical changes in clays due to frost action and their effect on engineering structures. *Proceedings on the International Symposium on Frost in geotechnical engineering*, 1:863–893.

Chamberlain, E. J. and Gow, A. J. (1979). Effect of freezing and thawing on the permeability and structure of soils. *Engineering geology*, 13(1-4):73–92.

Chang, D. K. and Lacy, H. S. (2008). Artificial ground freezing in geotechnical engineering.

Cole, D. and Abdullahi, A. (2001). Ice and frozen earth as construction materials.

Commons, W. (2017). File:resolution in direct and indirect x-ray detectors.svg — wikimedia commons, the free media repository. [Online; accessed 13-July-2019].

De Sheeran, D. and Rj, R. K. (1971). Preparation of homogeneous soil samples by slurry consolidation. *J Mater*, 6(2):356–373.

Fofonoff, N. P. and Millard Jr, R. (1983). Algorithms for the computation of fundamental properties of seawater.

Groenevelt, P. H. and Grant, C. D. (2013). Heave and heaving pressure in freezing soils: A unifying theory. *Vadose Zone Journal*, 12(1).

Han, B., Choi, J. H., Dantzig, J. A., and Bischof, J. C. (2006). A quantitative analysis on latent heat of an aqueous binary mixture. *Cryobiology*, 52(1):146–151.

House, R. (1993). *Random House unabridged dictionary*. New York: Author.

Ji-Lin, Q. and Wei, M. (2006). Influence of freezing-thawing on strength of overconsolidated soils. *Chinese Journal of Geotechnical Engineering*, 28(12):2082–2086.

Jia, F. (2018). Literature review on general information of frozen soil and ultrasonic wave measurement of unfrozen water content.

Kanevskiy, M., Shur, Y., Jorgenson, M., Ping, C.-L., Michaelson, G., Fortier, D., Stephani, E., Dillon, M., and Tumskoy, V. (2013). Ground ice in the upper permafrost of the beaufort sea coast of alaska. *Cold Regions Science and Technology*, 85:56–70.

Kenneth, R., Spring, B. O., Flynn, J. C. L., and Michael, W. D. (2019). Spatial resolution in digital imaging — microscopyu. [Online; accessed 13-July-2019].

Kotter, E. and Langer, M. (2002). Digital radiography with large-area flat-panel detectors. *European radiology*, 12(10):2562–2570.

Kump, K., Grantors, P., Pla, F., and Gobert, P. (1998). Digital x-ray detector technology. *RBM-News*, 20(9):221–226.

Kurz, D., Alfaro, M., and Graham, J. (2017). Thermal conductivities of frozen and unfrozen soils at three project sites in northern manitoba. *Cold Regions Science and Technology*, 140:30–38.

Lambe, R. V. W.-T. W. (2006). Meccanica dei terreni, seconda edizione. *Flaccovio Dario*.

Liu, Z., Liu, J., Li, X., and Fang, J. (2019). Experimental study on the volume and strength change of an unsaturated silty clay upon freezing. *Cold Regions Science and Technology*, 157:1–12.

Love, B. (2017). Chapter 5 - property assessments of tissues. In Love, B., editor, *Biomaterials*, pages 97 – 128. Academic Press.

Miller, R. (1972). Freezing and heaving of saturated and unsaturated soils. *Highway Research Record*, 393(1):1–11.

Müthing, N., Barciaga, T., and Schanz, T. (2017). Cyclic response of natural onsøy clay. In *Holistic Simulation of Geotechnical Installation Processes*, pages 257–274. Springer.

Niu, G.-Y. and Yang, Z.-L. (2006). Effects of frozen soil on snowmelt runoff and soil water storage at a continental scale. *Journal of Hydrometeorology*, 7(5):937–952.

Nixon, J. (1991). Discrete ice lens theory for frost heave in soils. *Canadian Geotechnical Journal*, 28(6):843–859.

O'Neill, K. and Miller, R. D. (1985). Exploration of a rigid ice model of frost heave. *Water Resources Research*, 21(3):281–296.

Pasquetto, S. and Patrone, L. (1994). *Chimica fisica*. Masson scuola.

Penumadu, D. and Dean, J. (2000). Compressibility effect in evaluating the pore-size distribution of kaolin clay using mercury intrusion porosimetry. *Canadian Geotechnical Journal*, 37(2):393–405.

Slunga, E. and Saarelainen, S. (2005). Determination of frost-susceptibility of soils.

Stanton, A. (1896). Wilhelm conrad röntgen on a new kind of rays: translation of a paper read before the würzburg physical and medical society, 1895. *Nature*, 53(1369):274–276.

Taber, S. (1929). Frost heaving. *The Journal of Geology*, 37(5):428–461.

Thomas, H. R., Cleall, P. J., Li, Y., Harris, C., and Kern-Luetschg, M. (2009). Modelling of cryogenic processes in permafrost and seasonally frozen soils. *Geotechnique*, 59(3):173–184.

Tommik, K. (2017). Consolidation of soft sediments using artificial ground freezing.

Tsytovich, N. (1960). *Bases and foundations on frozen soil*. National Academy of Sciences, National Research Council.

(UFC), U. F. C. (2004). Calculation methods for determination of depth of freeze and thaw in soil: Arctic and subarctic construction. *Washington, DC: U.S. Army Corps of Engineers*.

Viggiani, G. (2018). Advanced experimental geomechanics course. *Université Grenoble Alpes*.

Viggiani, G., Andò, E., Takano, D., and Santamarina, J. (2014). Laboratory x-ray tomography: a valuable experimental tool for revealing processes in soils. *Geotechnical Testing Journal*, 38(1):61–71.

Wang, J. and Nishimura, S. (2017). Interpretation of mechanical behavior of frozen clay through parallel tests of frozen and unfrozen soils. *Japanese Geotechnical Society Special Publication*, 5:155–160.

Wang, S., Yang, Z. J., and Yang, P. (2017). Structural change and volumetric shrinkage of clay due to freeze-thaw by 3d x-ray computed tomography. *Cold Regions Science and Technology*, 138:108–116.

Wikipedia (2019). Tubo radiogeno — wikipedia, l'enciclopedia libera. [Online; in data 11-luglio-2019].

Xu, X., Lai, Y., Dong, Y., and Qi, J. (2011). Laboratory investigation on strength and deformation characteristics of ice-saturated frozen sandy soil. *Cold Regions Science and Technology*, 69(1):98–104.

Xu, X., Wang, Y., Yin, Z., and Zhang, H. (2017). Effect of temperature and strain rate on mechanical characteristics and constitutive model of frozen helin loess. *Cold Regions Science and Technology*, 136:44–51.

Zumdahl, S. S. and Zumdahl, S. A. (2011). Chemistry: An atoms first approach.